Functionalization of Silica-Coated Iron Oxide Nanoparticles via the Silanol-Alcohol Condensation Reaction

by

Henry J.H. Kang

B.Sc., Simon Fraser University, 2016

Thesis Submitted in Partial Fulfillment of the
Requirements for the Degree of
Master of Science

in the
Department of Chemistry
Faculty of Science

SIMON FRASER UNIVERSITY
Fall 2019

Approval

Name:	**Henry J.H. Kang**
Degree:	**Master of Science (Chemistry)**
Title:	**Functionalization of silica coated iron oxide nanoparticles via the silanol-alcohol condensation reaction**
Examining Committee:	**Chair:** **Jeffrey Warren** Associate Professor
Byron Gates Senior Supervisor Associate Professor	
Daniel Leznoff Supervisor Professor	
Hua-Zhong Yu Supervisor Professor	
Neil Branda Internal Examiner Professor	

Date Defended/Approved: September 10th 2019

Abstract

The surface properties of nanoparticles play an important role in their interactions with their surroundings. Silane reagents have been used for surface modifications to silica shells on iron oxide nanoparticles, but using these reagents presents some challenges. Some of these challenges include the moisture sensitivity of silane reagents and the formation of multilayers. An alternative approach to modifying the surfaces of these silica shells was developed to impart different terminal functional groups, such as a thiol, alcohol, or carboxylic acid, through the use of alcohol-based reagents. This reaction was initiated through convective heating and microwave-assisted heating. This approach to surface functionalization of the core-shell particles was verified through analytical measurements and the attachment of gold nanoparticles. The silanol-alcohol condensation reaction was also extended to the mixed functionalization of the silica-coated iron oxide nanoparticles with both thiol and carboxylic acid functionalized alcohol reagents. The processes and results for the silanol-alcohol condensation reaction were also compared with silanization process. The use of the silanol-alcohol condensation reaction could be extended further to other surface functionalization through the use of additional alcohol-based reagents.

Keywords: Iron oxide nanoparticles; silanol-alcohol condensation; surface modification; core-shell structure; silica coating

To My beloved family and friends

Acknowledgments

I would like to thank my senior supervisor, Professor Byron D. Gates, for giving me the opportunity to work under his guidance. I deeply appreciate all the advice and support from him throughout my research career.

I also thank my committee members – Dr. Daniel Leznoff, and Dr. Hogan Yu – for their valuable advice and encouragement.

I would like to thank the technicians and engineers at 4D LABS, especially Dr. Xin Zhang and Dr. Michael Paul, for their help on training of the tools as well as advice on interpretation of the results.

I would also like to thank my past and current group members for all the enjoyment and humour in the lab. In particular, I want to thank Dr. Irene Andreu Blanco, Rana Faryad Ali, Melissa Radford, Stephanie Sonea, Iris Guo, and Dr. Austin Lee, among many friends and colleagues from the 4D Labs and the Department of Chemistry, for all their encouragement and all the scientific conversations I have had with them during my time at SFU.

Lastly, I want to thank my family for their continued support.

Table of Contents

List of Tables

List of Figures

List of Acronyms

APTES	(3-aminopropyl)triethoxysilane
Au NPs	gold nanoparticles
DI water	deionized water
DTNB	5,5’-dithio-bis-(2-nitrobenzoic acid)
EDC	N-(3-dimethylaminopropyl)-N’-ethylcarbodiimide
EDS	energy dispersive X-ray spectroscopy
ESAR	effective specific absorption rate
Fe_3O_4	magnetite
HDDA	12-hydroxy-1-dodecanoic acid
m_{np}	mass of nanoparticles that are used for hyperthermia
m_s	mass of solution that nanoparticles are dispersed in
MPTMS	(3-mercaptopropyl)trimethyoxysilane
MUD	11-mercapto-undecanol
NHS	N-hydroxysuccinimide
NPs	nanoparticles
PEG	poly(ethylene glycol)
PVP	polyvinylpyrrolidone
SAMs	self-assembled monolayers
SAR	specific absorption rate
SDS	sodium dodecyl sulfate
SEM	scanning electron microscopy
TEM	transmission electron microscopy
TEOS	tetraethyl orthosilicate
TGA	thermogravimetric analysis
TNB	2-nitro-5-thiobenzoic acid
XPS	X-ray photoelectron spectroscopy

Glossary

Antiferromagnetism	Type of magnetism in which the magnetic moments of metal species in a metal or metal oxide lattice point in the opposite direction and have the same magnitudes. Antiferromagnetism is observed in the salts of ions like Mn^{2+}, Fe^{3+}, and Gd^{3+}.
Brownian Relaxation	One of the two magnetic relaxation mechanisms that generate heat from magnetic nanoparticles under an alternating magnetic field. The relaxation of magnetic moments fixed to the nanoparticles.
Co-precipitation Synthesis	One of the processes to produce iron oxide nanoparticles. This process can be used to synthesize spherical nanoparticles with a diameter from 30 to 100 nm. The process is achieved by mixing 1 mole of ferrous salt with 2 moles of ferric salt in a basic aqueous medium at room temperature.
Curie Temperature	Above this temperature, a magnetic material loses its permanent magnetic properties and will have a paramagnetic behavior. This happens as thermal energy exceed the magnetic interactions.
Effective Specific Absorption Rate (ESAR)	The measurement of heat generated by nanoparticles. This measurement shows the amount of heat generated per mass of nanoparticles as a function of field strength.
Ellman's Test	Colorimetric assay for thiol quantification. The Ellman's reagent, 5,5'-dithio-bis-(2-nitrobenzoic acid) (DTNB), reacts with a free sulfhydryl group to yield a free 2-nitro-5-thiobenzoic acid (TNB). This TNB has an absorbance at 412 nm, which can be correlated to the concentration of thiol groups present in the sample.
Energy Dispersive X-ray Spectroscopy (EDS)	An analytical technique used to generate an elemental map of a sample. This technique is often coupled with SEM or TEM technique. The EDS techniques use characteristic X-ray emission from a sample to generate an elemental map. The characteristic X-rays are produced from the interaction between the high energy electron beam and the sample.
Ferrimagnetism	Type of magnetism in which the magnetic moments of metal species in a metal or metal oxide lattice point in the opposite direction, but these magnetic moments have different magnitudes. This results in a spontaneous magnetization.

Ferromagnetism	Type of magnetism in which the magnetic moments of metal species in a metal or metal oxide lattice point in the same direction. Ferromagnetism is observed for some transition metal species. Ferromagnetic materials are attracted to magnets.
Hyperthermia	A form of tumor treatment where heat is used to damage and kill the cancer cells in a biological system with minimal damage to other tissue.
Magnetically Activated Hyperthermia	The heat generated from the magnetic nanoparticles under an alternating magnetic field for use in the management of cancer. There are two different mechanisms of heat generation: (i) Brownian relaxation; and (ii) Neel relaxation.
Microwave	Electromagnetic radiation with frequencies between 300 MHz and 300 GHz.
MRI Contrast Agent	A material used to improve the visibility of structures when analyzed by magnetic resonance imaging (MRI).
Neel Relaxation	One of the two magnetic relaxation mechanisms that generate heat from the magnetic nanoparticles under an alternating magnetic field. The relaxation of magnetic moments within nanoparticles.
Self-Assembled Monolayers (Sams)	Assemblies of compounds that are formed spontaneously on the surfaces of materials and that are self-limiting to a coating thickness equal to the length of a single molecule.
Silanol-Alcohol Condensation Reaction	A chemical reaction between a silanol and an alcohol group to form a silyl bond while producing water as a by-product. This chemistry can be used to attach different alcohol groups onto the surfaces of silica.
Sol-Gel Chemistry	The sol-gel chemistry is a process to produce solid materials from small molecules. This process involves the conversion of monomers into a colloidal solution (sol) that acts as the precursor for a network (gel).
Solvothermal Synthesis	One of the processes to produce iron oxide nanoparticles. This process can be used to produce hydrophilic nanoparticles. This process is performed in a sealed container or in an autoclave with a high temperature in aqueous or non-aqueous solutions under a high vapor pressure.
Specific absorption rate (SAR)	The measurement of heat generated by nanoparticles. This measurement shows the amount of heat generated per mass of nanoparticles.

Thermogravimetric Analysis	An analytical technique where the mass of a sample is measured as a function of temperature and time. The weight changes can provide information about the thermal or oxidative stability, composition, or moisture content of a sample.
Tomographic Transmission Electron Microscopy	Tomographic transmission electron microscopy uses a number of TEM images that are obtained at different angles, which are combined to produce a three-dimensional visualization of a sample.
Transmission Electron Microscopy (TEM)	Transmission electron microscopy (TEM) is a microscopy technique where images are produced through the interactions of high energy, focused electron beam with a thin sample (<100 nm). This technique can provide a magnified view of a sample from 1,000 to 1,000,000 times.
X-Ray Photoelectron Spectroscopy (XPS)	X-ray photoelectron spectroscopy (XPS) is an analytical technique that is frequently used to study the chemical composition of the surfaces of a sample. The XPS technique measures photoelectrons that are ejected from a sample. The surfaces of the sample are irradiated with X-rays. These X-rays interact with the sample and cause photoelectrons to be ejected from the sample, which is detected by the XPS system.

Chapter 1. Introduction

1.1. Introduction to Iron Oxide Nanoparticles

Magnetic nanoparticles have been widely studied and incorporated into a range of different products.[1–5] Magnetic iron oxide nanoparticles, specifically, have been widely studied for use in water purification techniques, MRI contrast agents, bio-separations, and magnetically activated hyperthermia.[6–11] Importantly, these particles can be isolated and/or assembled through the use of applied magnetic fields. The properties of magnetic iron oxide nanoparticles can be altered through surface modifications. The properties of these nanoparticles can be further tuned by altering their size, shape, and composition.[12,13] There are a variety of known iron oxide structures (Table 1.1).[14] Hematite (α -Fe_2O_3), magnetite (Fe_3O_4), and maghemite (γ-Fe_2O_3) are the most commonly pursued structures.[15] These types of iron oxide nanoparticles can be chemically synthesized. Of these structures, magnetite and maghemite structures have ferrimagnetic properties, respectively. Hematite exhibits magnetic antiferromagnetic properties. In this thesis, magnetite nanoparticles are used as a platform for the demonstration herein as this type of iron oxide nanoparticle has a relatively high oxidative stability, and it is accepted to be a nontoxic magnetic material with approval use in for medical applications.[16] These nanoparticles will serve as a platform for coating with silica and functionalizing with a series of alcohol-containing reagents for demonstrating a new approach to tuning the surface chemistry of these materials.

Table 1.1 Name and chemical structure of different iron oxides[15]

iron oxide structure	chemical structure
magnetite	Fe_3O_4
maghemite	γ-Fe_2O_3
hematite	α-Fe_2O_3
feroxyhyte	δ'-FeOOH
goethite	FeO(OH)
akaganeite	$Fe^{3+}O(OH,Cl)$
lepidocrocite	γ-FeO(OH)
wustite	FeO
bernalite	$Fe(OH)_3$

1.1.1. Properties of Magnetite Iron Oxide Nanoparticles

Magnetite differs from most other iron oxides in that it contains iron species that are both divalent (Fe^{2+}, ferrous species) and trivalent (Fe^{3+}, ferric species). Magnetite has a cubic inverse spinel structure that consists of a cubic close-packed array of oxide ions. Figure 1.1 shows a crystal structure of the cubic unit cell of the magnetite structure. The schematic shows that the inverse spinel structure is made of up both octahedral and tetrahedral sites (Figure 1b, and 1c).[15,17] These two types of interstitial sites are the locations of the iron ions within the inverse spinel structure. These tetrahedral sites for iron are located at the center of a tetrahedron of oxygen atoms, and the octahedral sites for iron are located at the center of an octahedron of oxygen atoms. All corners of these tetrahedrons and octahedrons are occupied by oxygen species. In a unit cell of the inverse spinel structure, there are 64 tetrahedral sites and 32 octahedral sites. Only 8 of the tetrahedral sites and 16 of the octahedral sites are, however, occupied by iron cations. Half of these 16 octahedral sites are occupied by the Fe^{2+} and the other half are occupied by the Fe^{3+} species. All of the occupied tetrahedral sites contain Fe^{3+} species.[17] This mixed occupation of Fe^{2+} and Fe^{3+} ions in the octahedral sites enables the magnetite structure to have ferrimagnetic properties. Ferrimagnetic materials have atoms arranged with opposing magnetic moments. These moments are unequal, which results in a spontaneous magnetization. The Curie temperature of magnetite nanoparticles has been observed at 850 K.[18] Above the Curie temperature, these magnetite nanomaterials lose their permanent magnetic properties. Below the Curie temperature, the Fe^{2+} and Fe^{3+} ions in the octahedral sites are aligned opposite to the Fe^{3+} ions in the tetrahedral sites. A similar property has been observed in antiferromagnetic materials, but the magnitude of the anti-parallel spins in the magnetite is not equal and there is a net magnetic moment.[14] The magnetic ordering of magnetite with the structure of inverse-spinel has spin-state of high spin.[19]

The magnetic properties of magnetite nanoparticles also depend upon the size and shape of these materials. For instance, their saturation magnetization changes with the size of the nanoparticles.[20,21] A larger particle size results in a higher saturation magnetization than observed for smaller nanoparticles. This relationship between the magnetization and size of the magnetite particles is due to a decrease in the magnetic disorder at their surfaces, which results from the decrease in their surface-to-volume ratio.[22] Magnetic nanoparticles also have a size-dependent property that has been widely studied. Small magnetite nanoparticles with a diameter around 15 nm have an additional property that can be used for biomedical applications, which is discussed further below.

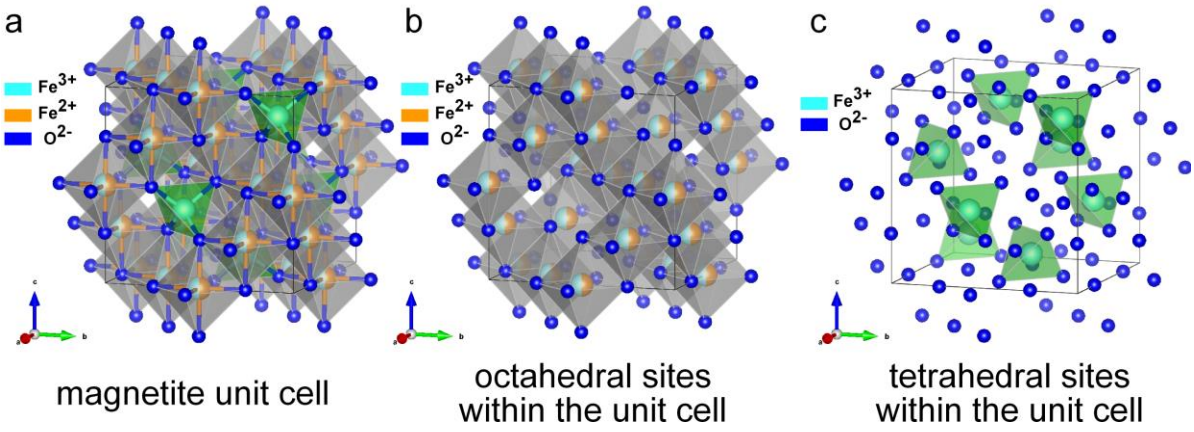

Figure 1.1 **Schematic of the inverse spinel crystal structure of magnetite: (a) polyhedral model of the cubic unit cell of the magnetite structure; (b) a polyhedral model for the occupation of Fe^{2+} and Fe^{3+} ions within the octahedral sites; and (c) polyhedral model for the occupation of Fe^{3+} ions within the tetrahedral sites. Light blue balls are Fe^{3+} ions, orange balls are Fe^{2+} ions, and dark blue balls are O^{2-} ions. Grey octahedrons signify the octahedral sites within the unit cell and the green tetrahedrons signify the tetrahedral sites within the unit cell.**

Magnetite nanoparticles with a diameter around 15 nm can generate heat under an alternating magnetic field.[23,24] These nanoparticles are single crystal nanoparticles. The heat generated can be used for the targeted heating of tumors. This effect is called hyperthermia. The heat released is generated by the superparamagnetic properties of these magnetite nanoparticles. This property of these magnetic nanoparticles allows them to be used as a therapeutic agent for triggering the release of drugs or to restrict tumor growth.[25–27] Superparamagnetism is a special form of magnetism exhibited in

small ferrimagnetic nanoparticles where each individual nanoparticle has its own magnetic domain or magnetic moment.[12] When superparamagnetic nanoparticles are subjected to an external alternating magnetic field, they release heat. This heat is generated through two relaxation processes: (i) Neel relaxation; or (ii) Brownian relaxation. When an alternating magnetic field is applied to the nanoparticles, each magnetic nanoparticle tries to rotate itself to align with the applied field. As the particle rotates, they undergo Brownian relaxation. Heat is generated as the particle undergoes shear stresses with the surrounding fluid.[28] The particles also undergo Neel relaxation where thermal energy is dissipated by the rearrangement of atomic dipole moments within the crystalline lattice.[29] The heat generated can be assessed as a specific absorption rate (SAR), which yields the amount of heat generated per mass of nanoparticles (Equation 1.1).[12,22,30]

$$SAR\left(\frac{W}{g}\right) = \frac{m_s \times c_p}{m_{np}} \times \left(\frac{\Delta T}{\Delta t}\right) \quad (1.1)$$

Equation 1.1 shows the calculation for SAR. Mass of the solution is m_s, m_{np} is the mass of the nanoparticles, c_p is the heat capacity of the solution, and ($\Delta T/\Delta t$) is the slope of the curve for the temperature rise vs. time while the nanoparticles are exposed to an alternating magnetic field. The calculated SAR values are used as a comparison between different nanoparticles.[12,22,30] The amount of heat generated has been shown to be largely dependent on particle size. Previous studies have shown that particles larger or smaller than 15 nm have a decreased efficiency for generating heat (Figure 1.2).[12] The efficiency of heat generation for these magnetic particles decreases as their superparamagnetic properties diminish, such as when the individual particles have multiple-domains rather than a single domain.[20]

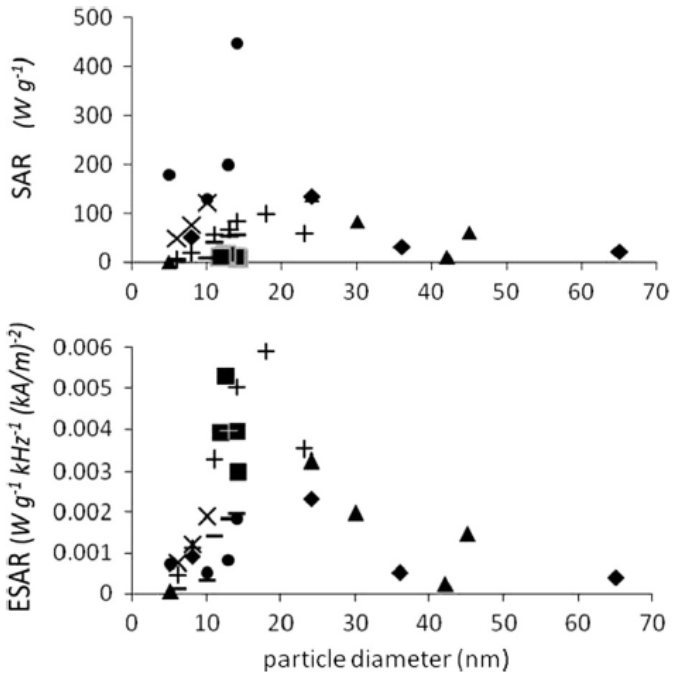

Figure 1.2 **Comparison of experimentally measured values for the specific absorption rate (SAR) as a function of nanoparticle size. When exposed to an alternating magnetic field. The upper plot shows the SAR plotted against the diameter of the magnetic nanoparticles. The lower plot shows these values reported as effective SAR (ESAR) in which SAR is divided by the field strength of the alternating magnetic field. This plot shows the size-dependent heating efficiency for iron oxide nanoparticles. Reprinted with permission from Copyright © 2013 Elsevier B.V. All rights reserved.**[31]

1.1.2. Synthesis of Magnetite Iron Oxide Nanoparticles

There are a variety of processes for synthesizing magnetite nanoparticles. These include co-precipitation[32], thermal decomposition[33], and hydrothermal decomposition methods.[34] The properties of the resulting nanoparticles are dependent on the synthetic route used to prepare these nanoparticles. Different synthetic routes could have a significant influence as a result of their reaction conditions, such as temperature, solvent, or surfactants. These conditions could affect the surface chemistry, shape, size, and water-dispersibility of the resulting nanoparticles.

The co-precipitation method is the simplest and most efficient chemical pathway to obtaining magnetic nanoparticles. This process can be used to synthesize spherical nanoparticles with diameters from 30 to 100 nm.[35] The nanoparticles are prepared from a mole ratio 1:2 of ferrous chloride ($FeCl_2 \cdot 4H_2O$) and ferric chloride ($FeCl_3 \cdot 6H_2O$) salts in a basic aqueous medium held at room temperature. This reaction takes place between pH 8 to 14.[32] The reaction follows the processes outlined in Equation 1.2.[32]

$$Fe^{2+} + 2\ Fe^{3+} + 8\ OH^- \leftrightarrow Fe(OH)_2 + 2\ Fe(OH)_3 \rightarrow Fe_3O_4 + 4\ H_2O \qquad (1.2)$$

In this reaction, the reaction starts with ferrous chloride and ferric chloride instead of iron (II) hydroxide and iron (III) hydroxide because the solubility of these hydroxide based species in aqueous solutions is very low.[36] The size of nanoparticles that are synthesized by the co-precipitation method can be changed by altering the pH. The first controlled preparation of superparamagnetic magnetite nanoparticles was performed by Massart *et al.* using alkaline precipitation of ferrous and ferric salts.[32]

There are two stages that are involved in the synthesis. A short period of nucleation occurs when the concentration of the species reaches a critical supersaturation. This step is followed by the slow growth of the nuclei from the diffusion of solutes to the surfaces of the crystal.[37] The factors on which the phase and size of the nanoparticles depend upon include the concentration of cations, the presence of counter ions, and the pH of the solution.[38,39] The main advantage of the co-precipitation process is that it is cost-effective, and a large number of nanoparticles can be synthesized at once.[40] There are some disadvantages to the co-precipitation process. The synthesized nanoparticles tend to have a high degree of particle agglomeration. The high proportion of agglomeration in the product is due to the large surface area to volume ratio of these

nanoparticles, and their relatively high surface energy. The agglomeration of the nanoparticles results in a decrease in their surface energy. These nanoparticles also interact through the strong magnetic attractions between the particles.[41] The control over particle size distribution in the product is also limited, which results in a polydispersed sample of nanoparticles.[38,42] As the nucleation step is short, there is a relatively short amount of time in which to control the particle size.[43] There are ways to restrict particle agglomeration by stabilizing the particles with surfactants during or after the synthesis. For instance, octanoic acid can be added during the synthesis to decrease the agglomeration of the product.[44] In summary, the co-precipitation syntheses can produce a large amount of iron oxide nanoparticles within a short amount of time, but it is limited in its ability to control the particle size and particle agglomeration.

Nanoparticles with a narrower size distribution can be achieved through thermal decomposition methods.[44–46] In this approach, iron oxide nanoparticles are obtained from a high-temperature (i.e., higher than 200 °C) decomposition of coordinated iron precursors. These precursors include iron acetylacetonate or iron carbonyls dissolved in organic solvents with the addition of stabilizers. Various organic molecules, such as oleic acid, 1-tetradecene, and oleylamine, are added to the reaction as stabilizers.[33] These surfactant molecules form nanodroplets of different sizes. Aqueous iron salt solutions can be encapsulated within these droplets to constrain the processes of nucleation and growth of the nanoparticles.[43] The size of the nanoparticles can be controlled by changing the reaction temperature and other parameters.[44] For instance, an increase in the concentration of ferric ion species promotes the growth of the particles in one direction leading to anisotropic elongation of the structures. The advantages of thermal decomposition method include control over the size and shape of the nanoparticles. Unlike the co-precipitation process, nanoparticles with a narrow size distribution can be synthesized from thermal decomposition.[47] In the thermal decomposition method, iron oxide nanoparticles with different morphologies can also be synthesized by altering the concentrations of the reagents or the reaction times.[48] A limitation of this process is that these particles are usually hydrophobic and can only disperse in nonpolar solvents.[44–46] The residual stabilizer present in the system may restrict the post-synthesis exchange of the surfactants on the surfaces of the as-synthesized nanoparticles.[49] The resulting nanoparticles can be transformed into hydrophilic materials by exchange of the surfactants with molecules containing hydrophilic groups, but these steps could require

sophisticated methods, and multiple steps are often needed to complete this exchange.[50] This could lead to loss of material, or the particles could aggregate during this procedure.

There are other methods to prepare iron oxide nanoparticles of a narrow size distribution that also are hydrophilic.[51–53] The solvothermal process produces monodisperse iron oxide nanoparticles in a sealed container or an autoclave of high reaction temperatures (i.e., above 200 °C) using either aqueous or non-aqueous solutions under high vapor pressures. This process is usually performed in a sealed container. This method is suitable for the growth of high-quality nanoparticles while maintaining good control over their composition. The product can also be hydrophilic. The synthesis of iron oxide nanoparticles by solvothermal techniques happens in two steps: (i) initial formation of small nanocrystals; and (ii) the aggregation into larger nanoparticles. Sodium citrate can bond to the surfaces of the initial nanocrystals, which prevents aggregation with other nanocrystals. The high surface energy of the nanocrystals can causes aggregation of the nanocrystals to reduce the surface energy. Subsequently, the resulting nanoparticles can be polycrystalline. As this aggregation step is rapid, the nanocrystals do not have time to rearrange. The resulting shape of these nanoclusters is spherical. Citrate molecules are still present on the surfaces of the nanoclusters, so the resulting nanoparticles are hydrophilic. The size of these nanoparticles increases with prolonged incubation times.[52]

In this thesis, a solvothermal method was used to synthesize hydrophilic magnetite nanoparticles with an average diameter of 200 nm.[54] The size of the nanoparticles can easily be changed with different synthetic routes. The purpose of the thesis is to demonstrate the chemical functionalization of silica-coated magnetic nanoparticles through the silanol alcohol condensation reaction. As a visualization of the success of this functionalization, 20-nm diameter gold nanoparticles were attached onto silica-coated iron oxide nanoparticles. The surfaces of these particles were prepared to exhibit external thiol functionality. The size of the iron oxide nanoparticles was selected because it would be easy to differentiate the two different types of nanoparticles by size. This size ratio also enables a significant number of gold nanoparticles to attach onto the functionalized magnetic nanoparticles. If the size of the iron oxide nanoparticles was 20 nm, for example, there would be a minimal number of gold nanoparticles that could attach to their surfaces. With an average diameter of 200 nm, a higher relative number

of gold nanoparticles could attach onto the thiol functionalized surfaces of these magnetic particles. The differences in the results between control samples and the thiol functionalized iron oxide nanoparticles could be easily observed as a result of this experimental design. The co-precipitation method could have been used to synthesize the 200-nm diameter iron oxide nanoparticles as well. However, nanoparticles that are synthesized through the co-precipitation method can easily aggregate as observed in our own experiments. The solvothermal synthesized nanoparticles were less likely to aggregate, and this process also produced hydrophilic nanoparticles. These hydrophilic nanoparticles were also desired as they could be directly coated with silica through the Stöber method.

1.1.3. Applications of Iron Oxide Nanoparticles

Iron oxide nanoparticles have been incorporated into many products due to their favourable properties. Magnetic nanoparticles can be easily separated from other species by using external magnets. As mentioned in the above sections, the properties of iron oxide nanoparticles can also be tuned by altering their size, shape, and surface chemistry. There are other advantages to these nanoparticles as well. These nanoparticles are biocompatible and non-toxic. These nanoparticles could be used in a variety of biomedical applications. Some of these biomedical applications include magnetic resonance imaging contrast agents,[55–57] or therapeutic agents.[58,59] These nanoparticles have been utilized for different application in other areas as well. For instance, due to their strong magnetic properties, these nanoparticles can be easily removed from their environment such as for remediation efforts. Iron oxide nanoparticles have been used as a water purifying agent to remove heavy metals or organic molecules from water.[3] Some disadvantages of the iron oxide nanoparticles are discussed in the following sections (i.e., Section 1.2). Some of the applications of iron oxide nanoparticles have been listed below in Table 1.2.

Table 1.2 Applications of iron oxide nanoparticles in different fields

Field	Application
Biomedical	Drug delivery[57,60,61] MRI contrast agent[55–57] Therapeutic agent (i.e., cancer therapy)[58,59]
Agriculture and Food	Fertilizer[2]
Environmental Remediation	Waste water treatment[1] Heavy metal removal from water[3]
Energy	Energy storage[62]
Sensors	Electrochemical sensor[63,64]
Catalysts	Catalyst agent[4,5]

1.2. Introduction to the Surface Modification of Silica-Coated Iron Oxide Nanoparticles

One of the advantages of magnetic iron oxide nanoparticles includes tunable properties through the attachment of different functional groups to the surfaces of these particles. This functionalization enables the iron oxide nanoparticles to be utilized in different applications. For instance, different functionalities such fluorescent tags for tracking purpose could be coupled onto the surface through EDC/NHS coupling with the carboxylic functionalized surface groups.[65] The stabilizing agents such as polyethylene glycol (PEG) could be attached onto the surface to increase colloidal stability of nanoparticles in the biological media (Fig. 1.3).[66] There are also certain limitations to using iron oxide nanoparticles without surfactants or surface coatings. These nanoparticles can easily decompose or aggregate into bigger clusters. Due to their large surface area to volume ratio, the iron oxide nanoparticles tend to form large aggregates that lower their surface energy.[67,68] This aggregation could also lead to changes in their magnetic properties. The other problem of these nanoparticles is that they can be easily oxidized. For instance, magnetite nanoparticles can be oxidized in air and lose their magnetic properties. In biomedical applications, the bare iron oxide nanoparticles can also undergo rapid biodegradation when exposed to biological systems.

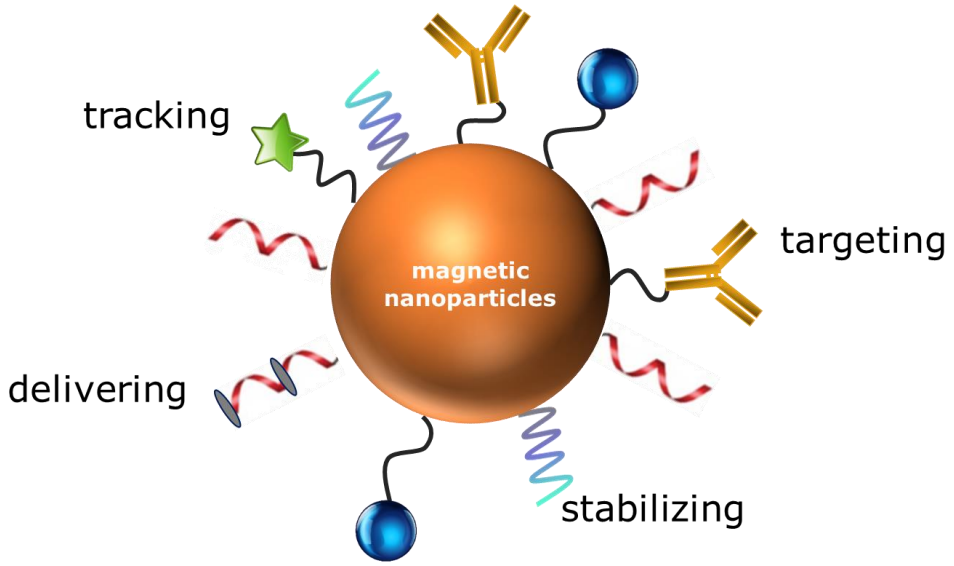

Figure 1.3 **Schematic of different functionalities that could be attached onto the surfaces of iron oxide nanoparticles.**

One of the ways to functionalize the surfaces of iron oxide nanoparticles is through a process of ligand exchange. Ligand exchange is where the ligand of interest is dissolved into a suspension with the nanoparticles. The functional species attached to the surfaces of the nanoparticles are substituted by the ligand of interest, which is maintained in excess in solution. One of the challenges of the ligand exchange process is that the iron within the nanoparticles could be lost during this process. It has been shown previously that iron (III) was may be removed from the surfaces of the nanoparticles by acidic dissolution upon binding 2,6-dihydroxy benzoic acid.[69] Therefore, protective coatings for these nanoparticles are critical for their use in these and other applications. One of the easiest ways to overcome these challenges is through additional surface functionalization. Surface coatings are prepared on iron oxide nanoparticles to give these materials further chemical protection and additional functionality to their surfaces.

There are a number of different methods for surface modifications that can be used to functionalize the surfaces of the iron oxide nanoparticles. For example, polymers can be used to coat the nanoparticles. High molecular weight polymers, such as chitosan[70,71] or dextran,[72,73] tend to have a poor affinity to the surfaces of these nanoparticles, resulting in loss of this coating over time and aggregation of the nanoparticles.[66,74] Silica is another popular class of coating material that is used to functionalize nanoparticles. This type of surface coating can protect the core nanoparticles from degradation and they can also reduce dipole-dipole interactions between iron oxide nanoparticles to reduce particle aggregation.[75] The silica surfaces are terminated by silanol groups, which can react with various coupling agents to covalently attach different molecules to the surfaces of these nanoparticles.

1.2.1. Silica-Coated Iron Oxide Nanoparticles and Their Surface Modification

The silica coating of hydrophilic iron oxide nanoparticles has been commonly achieved using the Stöber method.[76,77] The Stöber method uses tetraethyl orthosilicate (TEOS) to form silica coating on the surfaces of nanoparticles. The formation of silica shells on iron oxide nanoparticles can be broken down into two processes: (i) hydrolysis; and (ii) condensation.[78] The hydrolysis and poly-condensation reaction start at various sites of the TEOS reagents upon reaction with water solution as mixing occurs. These steps can be catalyzed through the addition of a base or an acid. The sol-gel chemistry of silica is otherwise very slow under neutral reaction conditions. In addition to acidic or basic catalysis, there are many other factors that could affect the rates of hydrolysis and condensation, such as the selection of solvents or the presence of chelating agents.[79]

The catalyst can change the resulting structure of the silica gel due to differences in the rate of hydrolysis facilitated by the catalyst. Hydrolysis results in the replacement of an alkoxy group with a hydroxyl through a pentacoordinate transition state in either the acid and base-catalyzed systems. Figures 1.4 and 1.5 show the mechanism of the acid and base-catalyzed reactions, respectively. The rate of each hydrolysis step depends on the stability of the transition state, which depends on the relative electron withdrawing or donating power of the silanol versus the silicon alkoxy groups (i.e., ethoxy). The acidic condition has a relatively slower hydrolysis step when compared to basic conditions. The condensation process is also catalyzed by either an acid or base, and depends on the hydrolysis step. This step results in the formation of siloxane bonds. If hydrolysis is completed, the resulting product is $(OH)_3Si\text{-}O\text{-}Si(OH)_3$, which has 6 sites for subsequent condensation reactions. In basic conditions, the hydrolysis step is quick as there are multiple condensation sites available, so the product leads to highly branched agglomerates. This condensation can result in the formation of a colloidal gel. For acidic conditions, as the hydrolysis step is slower, there are a limited number of condensation sites available. The limited number of reaction sites leads to the formation of chain-like structures in the acid catalyzed reaction.

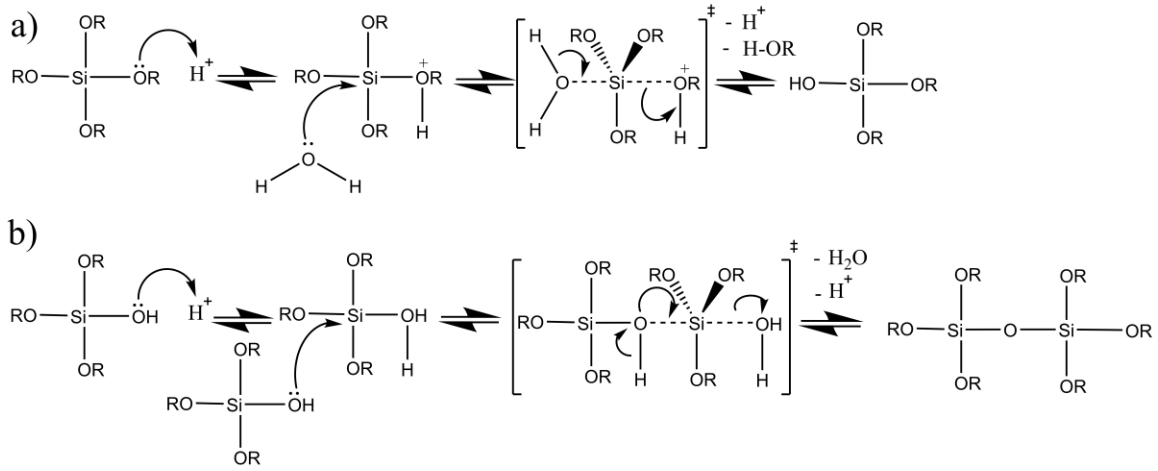

Figure 1.4 **Mechanism of acid catalyzed silane alkoxides: a) hydrolysis; and b) condensation.**

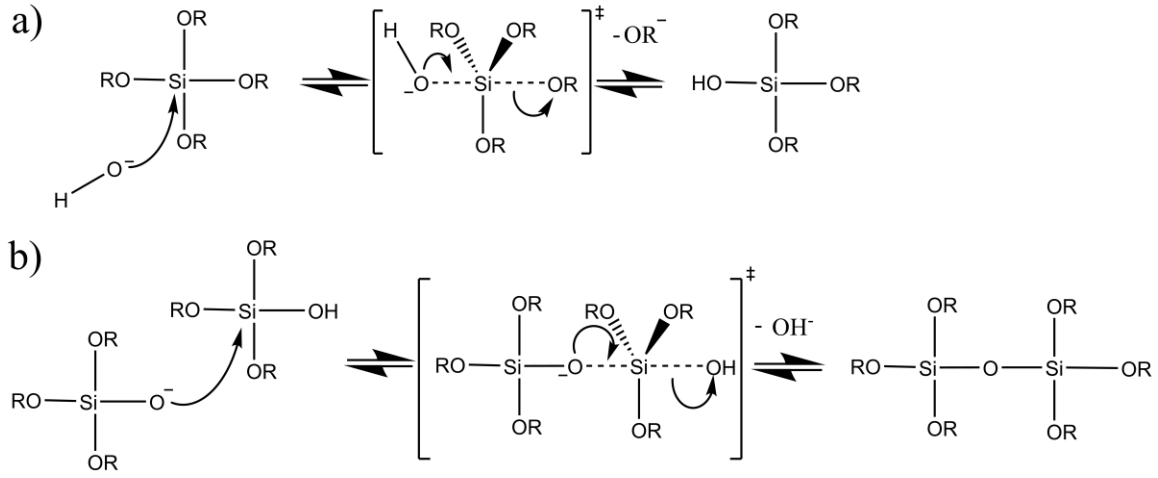

Figure 1.5 **Mechanism of base catalyzed silane alkoxides: a) hydrolysis; and b) condensation.**

Further modifications to the surfaces of the silica shell can be achieved through co-condensation reactions using silane chemistry. Different functional groups can be attached to these surfaces, such as primary or secondary amine groups, as well as thiol groups. These functional groups can be further modified through different coupling agents. These coupling reactions typically require coupling agents to activate the functional groups during the coupling process. For instance, an amine-functionalized silica shell can be prepared using aminated silanes, such as (3-aminopropyl)triethoxysilanes (APTES).[80–83] These silanes provide reactive sites for covalently attaching linkers to biomolecules.[84] These attachments can be achieved using coupling agents such as N-(3-dimethylaminopropyl)-N'-ethylcarbodiimide (EDC), and N-hydroxysuccinimide (NHS) ester. These agents are used to covalently attach amine-the functionalized silica shells to carboxylic groups of another reactant species.[65] Reacting with different functional groups will require different coupling agents. For instance, a thiol -functionalized silica shell can be prepared using a thiolated silane, such as 3-mercaptopropyltriethoxysilane. Maleimide-functionalized reagents can then be attached to the thiol-functionalized silica surfaces via formation of thioether bonds.[85] Coupling agents that are used for aminated silanes would not work for thiol functionalized surfaces. The advantages of using silane-based reagents include their ease of preparing coatings on different surfaces and the lower energy barrier towards condensation to form covalent bonds with these surfaces.[86]

There are some disadvantages to using silane reagents. These reagents are susceptible to competing side reactions,[87] tend to undergo intermolecular polymerization, and can form multilayers.[88] Previous literature depict that alkoxysilane reagents tend to make the "islands" of clustered silane reagents.[89] Figure 1.6 shows a schematic of both a single layer and a multi-layer formation with amine functionalized silane reagents. As depicted in Figure 1.6b, the possible orientation of silanes could be random and can lead to a multi-layer formation.

Another challenge of silane reagents are the quality of surface coating.[90] Previous literature also states that there is a dramatic variation in the surface coverage of the same silane reagents for silica particles obtained from different suppliers.[91] These coatings, for example, can consist of 2% to 300% surface coverage of the silane reagents. It is desirable to have processes for functionalizing silica through processes

that can be carried out more reproducibly, that utilize more widely accessible reagents, and that adds a diverse array of chemical functionality to these surfaces.

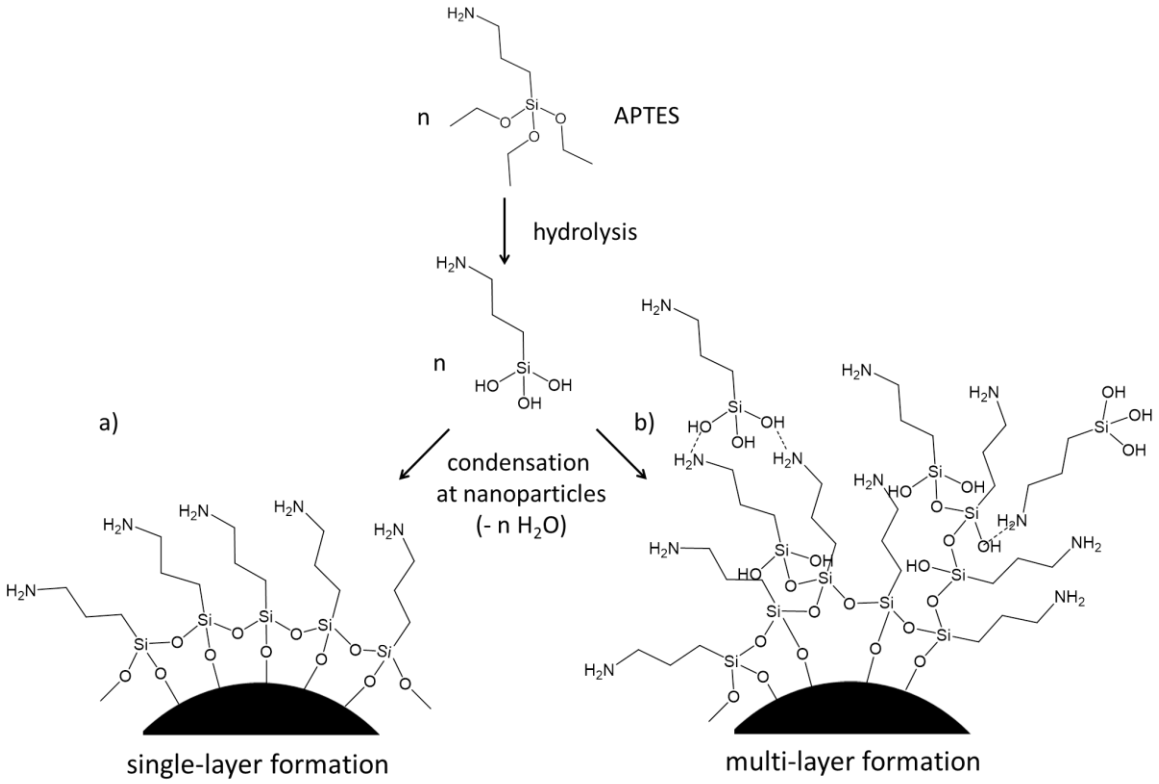

Figure 1.6 Possible reaction routes for the formation of amine functionalized nanoparticles through the use of (3-aminopropyl)triethyoxysilane or APTES. The reaction routes depict (a) a monolayer formation and (b) a multilayer formation at the surfaces of the nanoparticles.

1.2.2. Surface Modification through a Silanol-Alcohol Condensation Reaction

The functionality of silica surfaces can be tuned further through the covalent attachment of alcohol containing molecular reagents. Alcohol-based reagents can be covalently attached to silica surfaces through a condensation reaction to form self-assembled monolayers (SAMs). This reaction route has been previously utilized to tailor the properties of silica-coated wafers, glass slides, or quartz substrates. There are several advantages of the silanol-alcohol condensation reaction over silane-based surface modifications. For example, the reaction by-product is water (Figure 1.7). Other silane reagents can have different by-products. For instance, chlorosilanes produce HCl during the surface modification process. These by-products might also restrict the usage

of the nanoparticles, so the product purification steps become important. Alcohol molecules are also relatively stable in the water while silane reagents tend to react and self-polymerize in the presence of water. In addition, there are many more alcohol reagents readily available for purchase than silane-based reagents. The downside of the functionalization using alcohol-based reagents is their slow reaction kinetics. The silanol-alcohol condensation reaction also requires a substantial amount of energy input into the system.[92,93] Covalently attached monolayers derived from alcohol-based reagents can be achieved using a range of stimuli for driving the condensation reaction. These stimuli include convective heating[92,94], UV-irradiation[95], and microwave assisted heating[96,97]. This approach to the functionalization of silica has not been previously extended to silica-coated iron oxide nanoparticles.

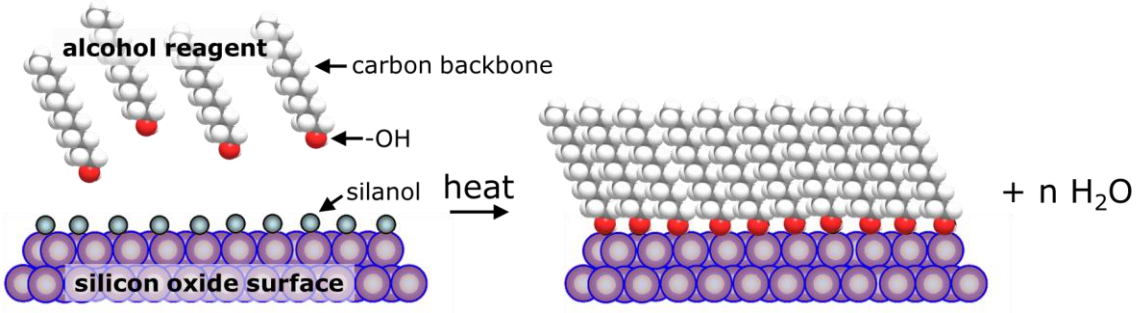

Figure 1.7 Schematic of the silanol-alcohol condensation reaction between an alcohol reagent and a silanol functionalized silicon oxide surface.

Convective heating processes, such as through the use of an oil bath, were previously used to initiate the silanol-alcohol condensation reaction on silicon-based wafers.[94] Optimization of the experimental conditions was achieved based on the results of analyses from different instrumental techniques, such as infrared spectroscopy or X-ray photoelectron spectroscopy. The success of the condensation reaction was first confirmed through infrared spectroscopy. Elevated temperatures approaching 250 ºC were initially required to observe a change to the properties of a silica substrate.[98] Later with the development of other analytical techniques, results from X-ray photoelectron spectroscopy demonstrated that the silanol-alcohol condensation reaction can be achieved at much lower temperatures, such as 120 ºC.[92] Other experimental conditions were also evaluated such as different alcohol reagents or changes in the reaction times. For example, different concentrations of 1-octanol were reacted with the silicon substrate while also adjusting the reaction times. The attachment of 1-octanol to the silicon substrate rendered it hydrophobic, as the attachment of 1-octanol led to an increase in

the water contact angle.[94] Hydrophobic materials are known to have water contact angles higher than 90º. Water contact angle measurements of 100º were achieved when immersing the silica substrate in the alcohol reagents at 120 ºC for over 24 h. When varying the concentration of 1-octanol, a higher water contact angle was achieved with an increase in the concentration of alcohol reagent (Figure 1.8). This previous study also demonstrated that polar aprotic solvents can be used to facilitate the formation of alcohol-based monolayers. Previous studies also demonstrated the importance of minimizing water content in the reaction. A higher water content in the reaction leads to a lower water contact angle after the reaction with the 1-octanol. This could correspond to the presence of fewer alcohol reagents attached to the silica surfaces.[94]

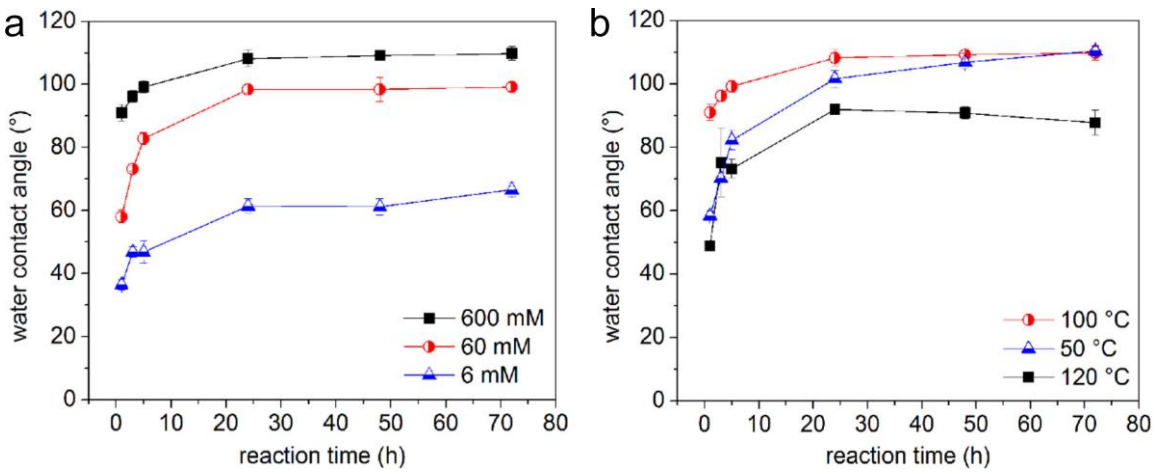

Figure 1.8 Water contact angle measurement for silicon substrates after reacting with 1-octanol dissolved in propylene carbonate while varying: a) concentration of 1-octanol; and b) temperature of the reaction. Reprinted with permission from © Copyright 2015 American Chemical Society.[94]

Microwave-assisted heating has a higher efficiency of heating than convective heating processes. Microwave heating induces more homogenous heating throughout the solution. Convective heating is not homogenous. The heating by convective processes is achieved through “wall heating” where the wall of the container is heated, and the heat is transmitted to the solution within (Figure 1.9). This heating method has been widely used to initiate reactions in material science and other types of syntheses. Microwave-assisted heating has been applied to the silanol-alcohol condensation reaction as well. As a comparison to the conventional heating process, 1-octanol was

also attached to the surfaces of a silica substrate using microwave assisted heating.[96] Water contact measurements and X-ray photoelectron spectroscopy were performed on the product to compare the results from microwave assisted heating with those from convective assisted heating. The rate of the reaction by microwave assisted heating was significantly faster than the convective heating method as observed from trends in water contact angle measurements. It was shown that the water contact angle was able to reach its maximum value over 100º within 30 min for the microwave assisted heating (Figure 1.10). The weakly bound octanol was removed through the Soxhlet extraction. Conventional heating (by oil bath) took around 24 h to reach a similar water contact angle value. These results show that microwave heating is more efficient when compared to convective heating.[96]

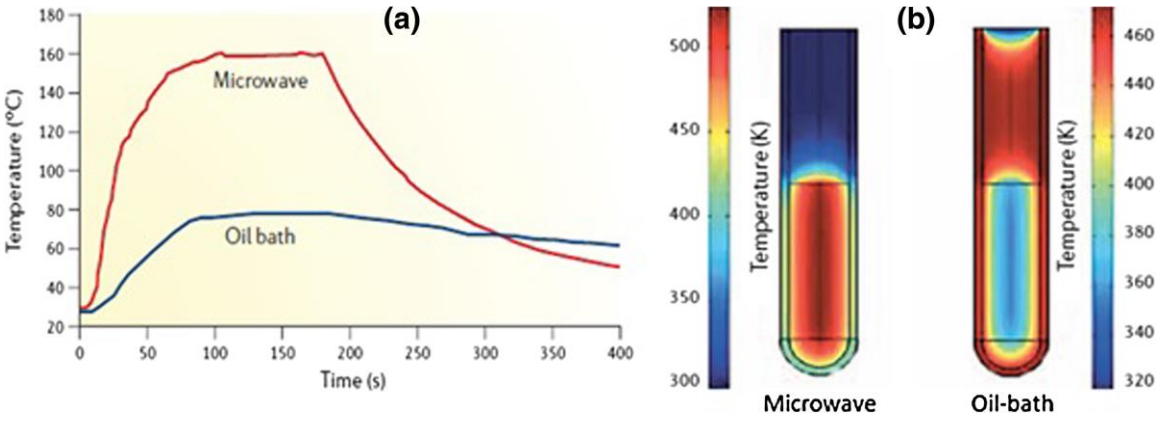

Figure 1.9 **Comparison between conventional heating versus microwave heating methods: a) comparison of temperature profiles achieved by each method; and b) distribution of thermal gradients within vials, under microwave and oil-bath conditions. Reprinted with permission from © Gude et al.; license Chemistry Central Ltd. 2013.**[99]

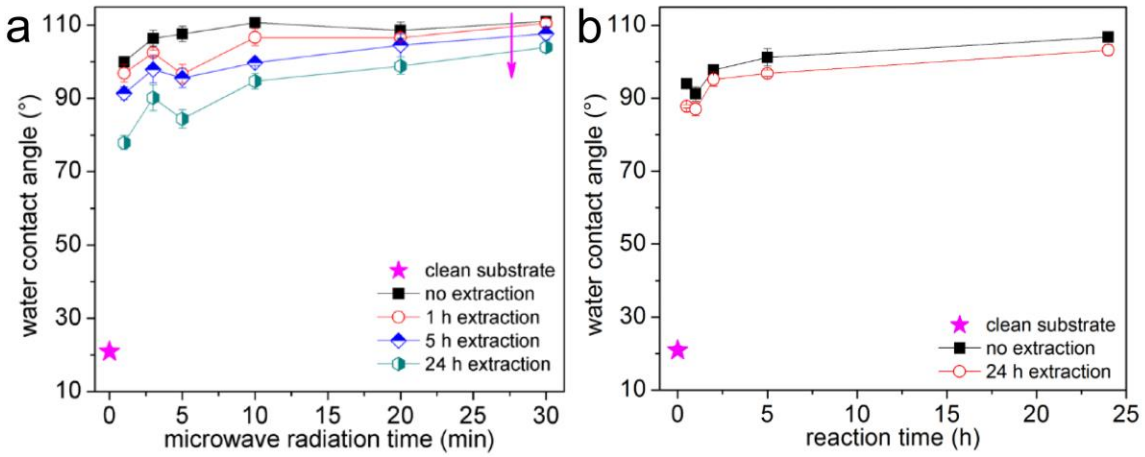

Figure 1.10 **Water contact angle measurement for silicon substrates after reacting with 1-octanol dissolved in propylene carbonate using different heating sources: a) a microwave reactor; and b) an oil bath. Reprinted with permission from © Copyright 2016 American Chemical Society.**[96]

1.3. Objectives of the Thesis

This thesis describes to demonstrate an alternative method to functionalize the surfaces of silica-coated iron oxide nanoparticles through a silanol-alcohol condensation reaction. The syntheses of the sought-after nanoparticles, and characterization of their surface modifications are the focus of the thesis. The aim of these studies is to build a foundation for silanol-alcohol condensation reactions using alcohol-containing reagents to modify the surfaces of silica-coated nanoparticles. This surface modification method has previously been applied to functionalize the surfaces of planar silica-coated silicon substrates. Previous literature demonstrated that this process can be used to change the properties of the planar silica surfaces with alcohol-based reagents. In this thesis, the silanol-alcohol condensation method was applied to functionalize the surfaces of silica-coated iron oxide nanoparticles.

The work in Chapter 3 demonstrates that the silanol-alcohol condensation reaction can be used to modify the surfaces of nanoparticles. In Chapter 3, a thiol-functionalized alcohol containing reagent, 11-mercapto-undecanol, was attached to the surfaces of silica nanoparticles. Gold nanoparticles were attached to these thiol coated nanoparticles to assist in verifying the surface modifications. Attachment of a large number of gold nanoparticles demonstrated that the thiol functionalization was successful. To further verify the modified surface chemistry, a thiol quantification assay via an Ellman's test was performed on the nanoparticles. The assay verified the presence of thiols on the surfaces of the purified nanoparticles. The work discussed in Chapter 4 seeks an optimization of the silanol-alcohol condensation reaction using a microwave-assisted process for surface modification, and the formation of monolayers prepared from a mixture of reagents on the surfaces of nanoparticles. Overall, the purpose of this thesis is to demonstrate surface modifications to silica-coated iron oxide nanoparticles. The silanol-alcohol condensation reaction could be achieved either using the microwave assisted heating or convective heating using an oil bath. The condensation reaction can be used to attach multiple types of alcohol-based reagents onto the surfaces of silica-based nanoparticles or silica coatings on nanoparticles. This approach to functionalizing nanoparticles could be extended into other types of functional alcohol reagents that can be utilized for different applications.

Chapter 2. Characterization of Functionalized Silica-Coated Iron Oxide Nanoparticles

In this thesis, the as-synthesized and functionalized nanoparticles were analyzed through the use of a number of different instruments. The size, shape, surface chemistry, and elemental compositions of functionalized nanoparticles were analyzed. In this chapter, these details of these instruments and their use are discussed.

2.1. Transmission Electron Microscopy (TEM)

Transmission electron microscopy (TEM) is a technique where images are produced through the interactions of a high energy focused electron beam with a thin sample. This technique can provide a magnified view of a sample from 1,000 to 1,000,000 times. It is frequently used to study the morphology, composition, and crystal structure of a sample. In this thesis, TEM was used to verify the size and shape of nanoparticles and to verify the presence of a silica coating on the iron oxide nanoparticles. This technique was first demonstrated by Max Knoll and Ernst Ruska in 1931. Ruska was awarded the Nobel Prize in physics for the development of electron optics and design of the transmission electron microscope.[100–102]

Electrons possess a wave-like characteristic that can be explained through the Louis de Broglie equation:

$$\lambda = \frac{h}{p} = \frac{h}{mv} \tag{2.1}$$

Here, λ is the wavelength of electrons in nm, h is Planck's constant (6.626×10^{-34}), and p, m, and v are the momentum, mass, and the velocity of the electron. When the accelerating voltage of the filament for a TEM is above 50 kV, electrons can be extracted from a filament or another electron source into the vacuum of the TEM system. If the accelerating potential is increased above 50 kV, this decreases the wavelength of the electron, which enables the electrons to penetrate through several microns of a solid sample. If this solid sample is crystalline, the incident electrons can be diffracted by crystal planes within the sample. This could be used for incident electron diffraction analyses of the solid sample. [100–102]

A sample needs to be first loaded onto a metal mesh for TEM analysis. This mesh is typically made of copper, nickel, or gold with support films of Formvar (polymers made up of polyvinyl alcohol and formaldehyde as copolymers with polyvinyl acetate) that is coated with a thin film of carbon (e.g., < 10-nm thick). Any solution left on the mesh is evaporated prior to insertion into the TEM. The metal mesh is then loaded onto a specimen holder and this holder inserted into the vacuum of the TEM system. The TEM that was used for the research in this thesis has a side-entry stage where the sample holder is loaded horizontally through an airlock. After sample insertion, the TEM column is put under high vacuum ($<10^{-6}$ Pa). Air is removed from the TEM column to minimize the scattering of the incident electrons by gas molecules.

The mechanics of a TEM system are briefly explained through the electron beam passage. High-energy electrons are first generated from the electron gun. For the TEM system that was used in this thesis, a Schottky source was used for generating the electron beam. This source consisted of a V-shaped tungsten filament with the tip coated with zirconium oxide. The emitted electrons are accelerated towards the anode, a round metal plate that has a central hole. This acceleration forms a high energy electron beam. Only 1% of the electrons produced pass through the central hole. Therefore, the beam current of the TEM system is only 1% of the emission current from the electron source. The electron beam that passes through the hole in the metal plate is subsequently focused and condensed onto the sample using a series of electromagnetic lenses. The electron beam that goes through the sample holder is focused onto the detector using condenser and objective lenses that are located under the sample holder. The focused electron beam hits the electron detector, which converts the projected electron image into a visible form (e.g., negative, or a digital display). [100–102]

There are certain downsides of TEM analyses that can restrict the usage of TEM techniques for studying the morphology of samples. These potential challenges include sample damage by the incident electron beam, interpretation of the transmitted images, and sample requirements that include restrictions on their thickness. Different solutions have been found to overcome some of these challenges. When the high energy electron beam is projected onto the sample, it can cause radiation damage to the sample. The damage tends to increase with higher accelerating voltages. Certain techniques such as specimen cooling or sensitive charge-coupled devices coupled with the TEM can decrease the electron dose required to create images of the samples. The decreased

electron dose minimizes damage to the samples. Another challenge is that TEM only presents a projected 2D view of the samples. A single TEM image cannot provide information regarding the depth and 3D morphology of the sample. Electron tomographic techniques are often used to overcome this problem. The tomographic techniques use a series of TEM images, obtained at different angles and combined together to produce a 3D view of the sample. In this thesis, a tomographic TEM technique was used to produce a 3D view of the sample to show the true sample morphology. The major challenge with TEM analyses is that the samples need to thin enough to allow the electrons to pass through the sample. For high-resolution TEM, a sample thickness on the order of 100 nm is usually suggested.[89] This restriction of the sample thickness can limit the type of samples that can be analyzed by TEM. Extra sample preparation steps can be taken to prepare samples. This preparation includes the focused ion beam (FIB) techniques. Unfortunately, this technique can be quite expensive so, therefore, accessibility to these instruments can be restricted.[100–102]

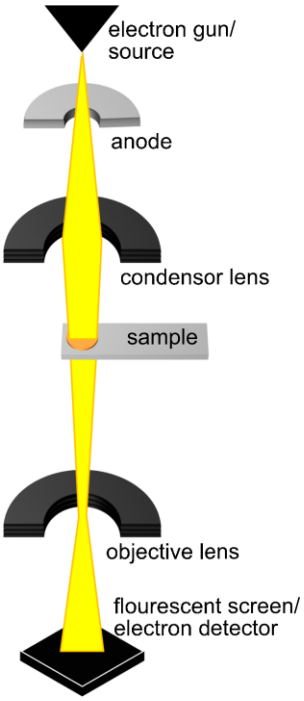

Figure 2.1 **A schematic diagram of a simplified view of the components of a transmission electron microscope (TEM). This schematic diagram is not drawn to scale.**

An electron microscope is a powerful tool that can be used to analyze small quantities of samples and relatively small samples that cannot be analyzed through typical optical microscopy techniques. The electron beam interactions with the sample provide information about its crystal structure and also produces a wide range of secondary signals from the sample (Figure 2.2). These signals can be used to study other properties that cannot be analyzed through brightfield (BF) TEM analyses. For instance, energy dispersive X-ray spectroscopy, as explained in the next section, can be used to map the elemental composition of the samples.[100–102]

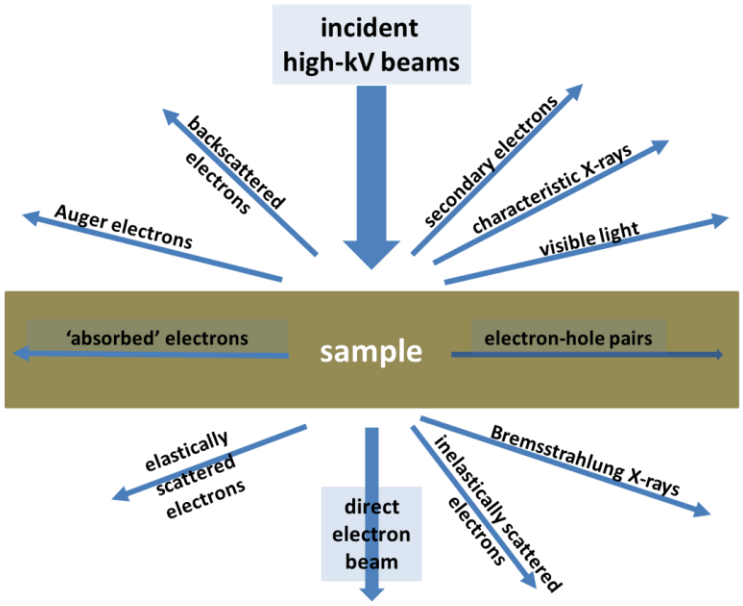

Figure 2.2 **A diagram that shows the possible signals that can be generated from the interaction between a high-energy electron beam and a sample. This diagram is not drawn to scale. The directions of the signals are to show the general direction where the signals could be detected.**

2.2. Energy Dispersive X-Ray Spectroscopy (EDS)

Energy dispersive X-ray spectroscopy (EDS) is used to generate an elemental map of the sample. This technique is often coupled with SEM or TEM techniques. Electron microscopy alone can provide magnified images of a sample, but this imaging alone cannot be used to distinguish different types of elements within the samples. The use of EDS can give information related to the composition of the elements within a sample. As these techniques can be coupled, the images of the sample can be paired with elemental mapping. In this thesis, EDS techniques were used to obtain an elemental map of the gold-iron-silica core-shell structure to differentiate the layers and components of these complex structures.[100,101]

The EDS techniques utilize the characteristic X-ray emission that comes from the sample to generate the elemental maps. The characteristic X-rays are produced from the interaction between the high energy electron beam and the atoms in a sample. The high energy electrons penetrate through the outer valence bands and interact with the inner-shell electrons. If the critical ionization energy is met, electrons can be knocked out of inner shells electron. The critical ionization energy is the amount of energy required for the inner-shell electrons to be ionized. The ejection of an inner shell electron forms a hole in the inner shell and the atom is ionized for a few seconds. An outer shell electron releases energy to fill the inner shell hole. This transition corresponds with the emission of a characteristic X-ray. The energy of this characteristic X-ray emission is the energy difference between the outer shell electron and the inner shell hole. This energy transition is specific to each element.[99] The energies of the X-rays produced increase as the electrons are more tightly bound to the nucleus, so an atom with a higher Z number (atomic number) would require a higher critical ionization energy. Each element typically has at least one characteristic peak in the EDS spectrum and the elements can be distinguished by the specific photon energy associated with the observed peaks, which correspond to the energy of the emitted X-rays. High Z number elements can have several peaks, which can overlap with the peaks from other elements in the sample. The peaks, however, form a fingerprint in terms of peak position and relative peak intensity that can be used to distinguish different elements. When an EDS measurement is coupled with an analytical electron microscope, elemental maps can be overlaid with the electron microscopy images.[100,101]

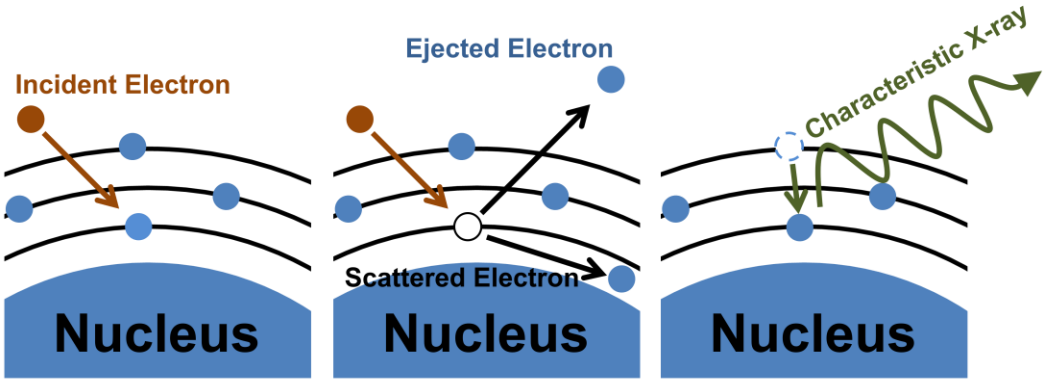

Figure 2.3 **Schematic depiction of the mechanism of energy dispersive X-ray spectroscopy: a) an incident electron beam penetrates through the electron shell; b) the incident electron beam ejects an inner shell electron; and c) the resulting hole in the inner shell is filled by one of the outer shell electrons, which results in the emission of a characteristic X-ray. This schematic is not drawn to scale.**

There are some disadvantages to EDS techniques. As mentioned above, high Z number elements have several peaks and these peaks can overlap with the peaks of other elements. Therefore, a single peak could contain overlapping signals from different elements. For instance, titanium and oxygen are not easy to distinguish from one another in their EDS spectra.[102] If the user has an idea of what kind of elements are present in the sample, peak fitting (e.g., accounting for peak positions and their relative intensities) can be used to differentiate these peaks. The other challenges of EDS techniques are the detection of relatively light elements, such as lithium or boron. Other techniques such as electron energy loss spectroscopy (EELS) are known to have a lower detection limit for lighter elements.[101] The relative high background signal in EDS analyses at low photon energies can also be a challenge. This background is associated with the incident electron beam. When the incident electrons pass close to an atomic nucleus, much of this primary electron beam is scattered within the sample. This process leads to the Bremsstrahlung emission of electrons. The characteristic X-ray emission lines are, therefore, superimposed onto this Bremsstrahlung background. This background spans from low to high energies as a broad continuous peak.[100,101]

Energy dispersive X-ray spectroscopy is a powerful technique that can generate elemental maps to differentiate the distribution of elements within a sample. For this thesis, EDS and elemental mapping were utilized to differentiate the layers of the core-shell structures. Unfortunately, EDS could not provide information on the molecular

coating itself. Other techniques such as X-ray photoelectron spectroscopy and a colorimetric assay (i.e., Ellman's Test) were, therefore, used to analyze the molecular coatings on the nanoparticles.

2.3. X-ray Photoelectron Spectroscopy (XPS)

X-ray photoelectron spectroscopy (XPS) is an analytical technique that is frequently used to study the chemical composition of the surfaces of a sample. The XPS can also determine the chemical bonding states of the elements in the sample. In this thesis, XPS was utilized to verify the chemical composition of customized surface coatings on the silica-coated iron oxide nanoparticles. This technique verified the successful surface modification of the nanoparticles. High-resolution XPS was developed in the 1950's under the leadership of Kai Siegbahn.[103] The first commercial XPS was developed at the end of the 1960's.[104] This technique is similar to EDS in terms of its use of the secondary signal coming from the interactions between from an incident energy source and the atoms of a sample. There are specific differences between these two techniques. High energy electrons are used to induce the emission of characteristic X-rays in EDS analyses, but a monochromatic X-ray source is often used to excite the inner shell electrons in XPS analyses. Characteristic X-rays ejected from the sample are used to determine the elemental composition in EDS, but the kinetic energy of the ejected inner shell electrons (i.e., photoelectrons) provide chemical information of the sample in XPS.[104]

The XPS system measures the energy of the photoelectrons that are ejected from the sample. The surfaces of the sample are irradiated with incident X-rays. A common X-ray source is an aluminum or magnesium operating at power from 500 to 1000 W.[104] In this thesis, an aluminum source (1487 eV) was used to generate the incident X-ray beam. These X-rays interact with the inner shell electrons of the atoms in the samples. Similar to how an inner shell electron is ejected by a high energy electron beam in EDS, the X-ray causes a photoelectron to be ejected from the inner shell.[104] The placement of the sample under vacuum is also required to avoid scattering or absorption of the photoelectrons by gas molecules, and to restrict contamination of the surfaces from adsorbed volatile species. The emission of photoelectrons is limited to a depth of approximately 10 nm, as they are otherwise absorbed or heavily scattered by the sample.[105] The kinetic energy of the photoelectrons is analyzed by an electron energy

analyzer. The measured energy is approximately the difference between the binding energy of the electron and the incident photon energy. The electron binding energy is specific to each element and the orbital from which the photoelectron was ejected. A survey scan is used to assess the elements in a sample over a wide range of energy levels. Higher resolution scans measure a narrower range of energies of a particular photoelectron emitted from the orbital of a single element. A high-resolution scan is used to determine the chemical states of the elements within a sample.[104]

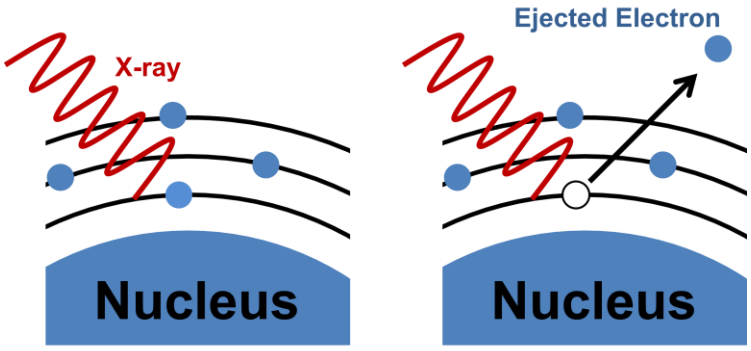

Figure 2.4 Schematic depiction of the mechanism associated with X-ray photoelectron spectroscopy: a) an incident X-ray penetrates through the outer shell electrons; and b) the incident X-ray causes an inner electron (or photoelectron) to be ejected from the shell.

One advantage of XPS is that it has a relatively low background signal. The XPS also induces relatively less sample damage than many other analytical techniques. Another advantage is the relatively high sensitivity of XPS for surface chemistry analyses. There are also some disadvantages to XPS as well. For example, the penetration depth of the photoelectrons is only about 10 nm. Therefore, it has a limited depth of analysis. Other techniques, such as EDS coupled with STEM, can be used to analyze sample compositions a greater depth. Some of EDS techniques can analyze the composition of a sample with a thickness of up to 100 nm.[104]

2.4. Ellman's Test, Thiol Quantification Assay

In 1959, the Ellman's Test was introduced as a versatile water-soluble technique to quantify the free sulfhydryl groups (-SH) present in an aqueous solution.[106] This test is now frequently used to quantify the thiol content in biochemical species, such as in proteins or low-molecular-mass thiols such as glutathione. Other methods that can be used to quantify the presence of thiol include inductively coupled plasma mass spectrometry (ICP-MS),[107] thermogravimetric analysis (TGA),[108] and liquid chromatography in tandem with mass spectrometry (LC-MS).[109] These techniques tend to require larger amounts of sample, can be relatively expensive, and can be time-consuming. The Ellman's Test is relatively simple, inexpensive, and fast. There are limitations to the Ellman's Test. It can be susceptible to matrix effects from certain buffers. The Ellman's reagent also has a low stability under acidic conditions, and can have pH dependent absorbance. Between pH of 7.3 to 10, the Ellman's reagent do not have independent absorbance.[110]

The concentration of thiol molecules is measured by the Ellman's Test through the reaction of the Ellman's reagent and the thiol containing the sample. The Ellman's reagent, 5,5'-dithiobis-(2-nitrobenzoic acid) (DTNB), and the sample are mixed in a phosphate buffer at a pH of 8. The DTNB has highly oxidizing disulfide bond (pKa 4.5). This disulfide bond is reduced by the free aliphatic thiol groups in an exchange reaction, and forms a mixed disulfide bond along with the yellow colored 2-nitro-5-nitrobenzoic acid (TNB^{2-}) species (Figure 2.5). The amount of TNB^{2-} is quantitatively related to the amount of thiol in the sample (1 TNB^{2-}:1 thiol), which can be quantified through the UV-Vis absorbance of TNB^{2-} at 412 nm. As the amount of thiol content in sample increases, the absorbance at 412 nm increases as well.[111] Previous literature has demonstrated that the disulfide exchange reaction between sulfur groups that are attached to the aromatic groups and the alkyl thiol groups should reach completion.[112]

It has been previously demonstrated that the Ellman's Test can be used to analyze the thiol content on the surfaces of thiol-functionalized silica nanoparticles. This method was compared to results of electrospray ionization time of flight mass spectroscopy (TOF-MS) to validate that this test as a reliable means to quantify the thiol content of the surfaces of nanoparticles. It was demonstrated that thiol quantification for freely accessible (thiols pointing outwards, opposite to the nanoparticle core) can be

achieved using the Ellman's Test. To analyze the thiols bound to the surfaces of nanoparticles, the nanoparticles need to be dispersed in the solution containing the Ellman's reagent.[113] In this thesis, the Ellman's Test was used to quantify the amount of freely available thiol on the surfaces of the functionalized nanoparticles. Figure 2.6 shows the schematic of the reaction between the thiol functionalized silica-coated iron oxide nanoparticles and the Ellman's reagent. As the Ellman's reagent reacts with a thiolate anion, to quantify the presence of these species, the orientation of thiol functionalization can also be verified. If the orientation of thiol groups were towards the core of the nanoparticles (e.g., resulting from binding or adsorption to the silica), there would not be a colorimetric response from the Ellman's reagent.

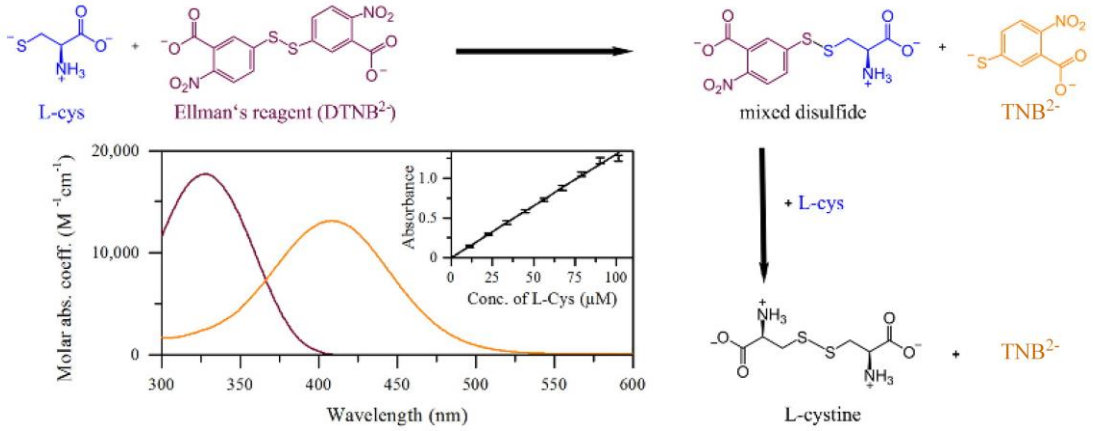

Figure 2.5 **A possible reaction between L-Cys (blue) and the Ellman's reagent ($DTNB^{2-}$, dark purple) is shown. The concentration of L-cys is related to the formation of TNB^{2-} (orange). The spectrum shows the molar absorption of both the Ellman's reagent (dark purple) and the TNB^{2-} (orange). Insert within the spectrum shows the relationship between the concentration of L-Cys and the Ellman's reagent. Reprinted with permission from © Copyright 2015 American Chemical Society.**[111]

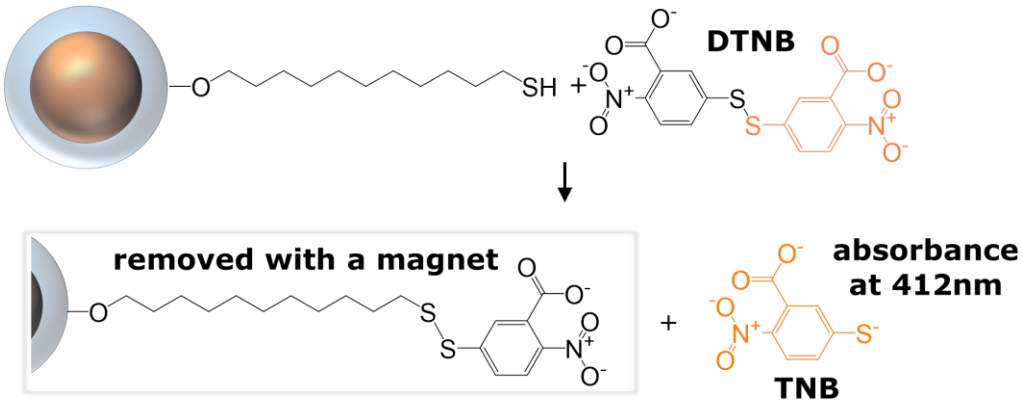

Figure 2.6 **Schematic of the reaction between thiol functionalized silica-coated iron oxide NPs and the Ellman's reagent.**

Chapter 3. Assembly of Gold Nanoparticles onto Silica-Coated Iron Oxide Nanoparticles Assisted by a Silanol-Alcohol Condensation Reaction

3.1. Notice of Permission

The following chapter is adapted with permission from copyright © The Royal Society of Chemistry 2019: Kang, H., et al., "Tunable functionalization of silica-coated iron oxide nanoparticle via silanol-alcohol condensation reaction:, Chemical Communications, 2019, 55, 10452-10455.[114] The majority of the work presented in this chapter has been performed by myself, including experiments, data acquisition and writing, under the supervision of Dr. Byron Gates. Dr. Michael T. Y. Paul performed the TEM tomography analysis. Mr. Faryad Rana Ali performed the XRF analyses of iron oxide nanoparticles and provided advice on the synthesis and silica coating of iron oxide nanoparticles. Dr. Austin Lee provided advice on the silanol-alcohol condensation reaction and Dr. Irene Andreu provided advice on the formation of the core-shell structures. Ms. Melissa J. Radford provided an assistance in the procedures to quantify the thiol surface coverage of the functionalized silica-coated iron oxide nanoparticles.

3.2. Introduction

Among magnetic nanoparticles, the magnetite phase of iron oxide (Fe_3O_4), specifically, have been widely studied for use in water purification, as well as for use in therapeutic purposes and as MRI contrast agents.[6,8–11,115] Surface modifications to these NPs are important for improving their colloidal stability and their utility in a range of applications. A challenge with handling many Fe_3O_4 NPs is that they can easily aggregate or decompose.[67,68] Stabilization of Fe_3O_4 NPs is often sought through modifications to their surface chemistry. The surfaces of Fe_3O_4 NPs can be modified through the attachment of polymer coatings[70–72,116] or silane reagents.[9,80–82] Polymer coatings have several limitations that include a significant increase in the hydrodynamic size of the NPs, which can affect their *in vivo* circulation time and cellular uptake.[74,117] Alternatively, silica coatings have been widely utilized to create core-shell NPs. Advantages of a silica coating include its hydrophilicity[76] and the ability to minimize

unwanted magnetic interactions between individual NPs such as induced particle agglomeration.

The functionalization of silica can be achieved through the covalent attachment of silane reagents, such as 3-mercaptopropyltrimethoxysilane (3-MPTMS) or (3-aminopropyl)triethoxysilane (APTES).[80–82] Other functionalities are also available, such as fluorinated, nitrile or methyl terminated reagents. There are, however, a number of challenges of using silane-based reagents. For example, these reagents are susceptible to competing side reactions,[87] sensitive to moisture, tend to undergo intermolecular polymerization, and can form multilayers.[88] It is desirable to tune the surface chemistry of the silica coatings through processes that can overcome these challenges.

Silica surfaces can also be tuned through the covalent attachment of alcohol containing molecular reagents. Alcohol-based reagents can be covalently attached to silica through a condensation reaction. This approach has been previously utilized to form self-assembled monolayers (SAMs) on planar silica.[94,96] There are several advantages of utilizing the condensation reaction between silanols and alcohols. The reaction by-product is water, whereas for chlorosilanes reacting with silanols the by-product is hydrogen chloride.[118,119] Alcohol-based reagents are often stable in the presence of water, whereas silane-based reagents will undergo hydrolysis and polymerization. This process of functionalizing silica surfaces by a silanol-alcohol condensation reaction has not previously been extended to silica-coated NPs.

In this study, we utilized oil bath assisted heating to functionalize silica-coated Fe_3O_4 NPs through a silanol-alcohol condensation reaction. As a demonstration of this reaction pathway, a thiol functionalized alcohol reagent—11-mercapto-1-undecanol—was covalently attached to the surfaces of silica. After purification of the product, gold (Au) NPs were assembled onto the silica coatings as a potential utilization of the thiol surface functionalization. The reactivity of thiols with Au surfaces is well-known.[120,121] The thiols served as an anchor for attaching Au NPs onto the magnetic NPs. The formation of these assemblies assisted in verifying the successful covalent attachment of the thiolated reagents to the silica through a silanol-alcohol condensation reaction. A diol and a carboxylic acid terminated linear alcohol were also attached to the silica-coated Fe_3O_4 NPs to demonstrate the wider utility of this reaction pathway. For these reactions, propylene carbonate was selected as a polar aprotic solvent because it is considered to

be a green solvent,[122] and it has been demonstrated to be stable under similar reaction conditions.[94] The reactions were maintained at 80 °C assisted by oil bath heating to demonstrate a relatively low temperature process that would be applicable for a range of reagents.

3.3. Experimental

All of the chemicals were of analytical grade and were used as received without further purification. Iron (III) chloride hexahydrate (97%), gold (III) chloride trihydrate (≥99.9%), sodium citrate tribasic dihydrate (ACS reagent, ≥99.0%), sodium dodecyl sulfate (≥98.5%), propylene carbonate (99%), polyethylene glycol 5,000 monomethyl ether (PEG; 5,000 MW), and tetraethyl orthosilicate or TEOS (98%) were all obtained from Sigma-Aldrich (USA). Chemicals such as 11-mercapto-1-undecanol (97%), 11-undecanoic acid (96%), 1,10-decandiol (98%), and polyvinylpyrrolidone (≤100%, 10,000 MW) were all obtained from Aldrich. An aqueous solution of ammonium hydroxide (28% to 30%) was obtained from BDH (USA). Ellman's reagent (95 to 100%, lot # TC262582) was obtained from Thermo Scientific (USA). Urea (99%) and hydrogen peroxide (a 30% aqueous solution) were obtained from Fisher Scientific (USA). Polyethylene glycol (PEG, 100%, 200 MW) was obtained from Alfa Aesar (Belgium). Methoxy terminated PEG-thiol ($mPEG_{5000}$-SH, 5,000 MW) was obtained from NanoCS (USA). Hydrochloric acid (36 to 38.5%, v/v, in water) was obtained from VWR (USA). Nitric acid (68 to 70%, v/v, in water) was obtained from ACP (USA). Sulfuric acid (95 to 98%, v/v, in water) was obtained from Caledon (USA). Ultrapure, deionized (DI) water (18.2 MΩ·cm) was obtained using a NANOpure DIamond™ system from Barnstead (USA).

3.3.1. Synthesis of Iron Oxide Nanoparticles (Fe_3O_4 NPs)

These nanoparticles (NPs) were synthesized via a modified solvothermal method.[54] Iron (III) chloride hexahydrate (0.12 M), sodium citrate tribasic dihydrate (0.06 M), and urea (1.0 M) were dissolved in ethylene glycol (10 mL) with the aid of vigorous mechanical stirring for 60 min. This mixture was transferred to a Teflon lined stainless-steel autoclave (Model No. 4749, Parr Instruments Co., Moline, IL, USA), sealed, and heated at 200 °C for 8 h. After cooling the solution to room temperature, black particles were isolated from the solution using an external magnet (Fig. 3.1). The supernatant was

decanted and the isolated particles were suspended in 20 mL of ethanol. These steps for washing and isolation of the magnetic NPs were repeated a total of three times. After this process of washing the NPs, the isolated solids were dried in an oven at 70 °C for 2 h.

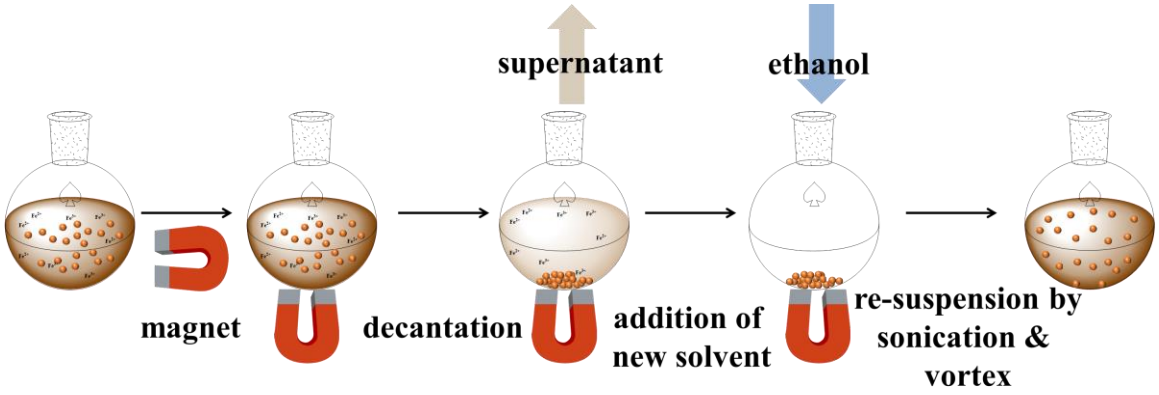

Figure 3.1 Schematic of purification of nanoparticles using the external magnet.

3.3.2. Silica Coating of the Fe_3O_4 NPs

The magnetic NPs were coated with a layer of silica using a Stöber sol-gel process.[77] A portion of the dried iron oxide NPs (10 mg) were re-suspended in a mixture of 16 mL DI water and 64 mL ethanol with the aid of sonication (Bransonic, Ultrasonic cleaner, 50 to 60 Hz) for 1 h. This solution of NPs was stirred using an overhead mechanical stirrer (Fisher Scientific, Compact Overhead Stirrer, 50 W output) rotating at 500 rpm during the addition of ammonium hydroxide and tetraethyl orthosilicate (TEOS). The ammonium hydroxide (1 mL) was added all at once, and subsequently, the TEOS (1 mL) was added dropwise over a period of 5 min. This mixture was stirred continuously for 6 h. After this process, the particles were magnetically isolated from the solution, and the particles were washed by suspending these solids in 20 mL of ethanol with the agitation of the solution for 3 min. This purification process was repeated at least two more times.

3.3.3. Functionalization of the Silica-Coated Fe_3O_4 NPs

Functionalization of the silica-coated iron oxide NPs was achieved using a modified silanol-alcohol condensation reaction.[94] The silica-coated iron oxide NPs were washed again, but propylene carbonate was used in place of ethanol. The supernatant was removed after isolating the NPs from the solution, and these pelleted solids were suspended into a fresh solution of propylene carbonate. This purification process was repeated one more time to remove traces of ethanol from the solution. The desired alcohol reagent, such as 11-mercapto-1-undecanol, was prepared as a 500 mM solution in 2 mL of propylene carbonate. This solution of alcohol reagent was mixed with the pelleted NPs. The vial containing this solution was sealed with a plastic cap and wrapped in parafilm. A suspension of these NPs was obtained by vortexing the solution for 5 min and sonicating for another 5 min. The sealed container was subsequently heated at 80 °C over 24 h by immersion in an oil bath under magnetic stirring. This temperature can also be easily achieved using oil, water, or sand bath assisted heating. The set-up was covered with aluminum foil to reduce exposure to ambient light. After 24 h, the NPs were isolated by use of an external magnet from the excess, unreacted reagents. The isolated NPs were magnetically washed three times with isopropanol as the rinse solution. Following each step of this procedure, the washed NPs were suspended in 10 mL of isopropanol by agitation using a vortexer for 3 min followed by sonication for another 3 min. Isopropanol was chosen as the wash solvent as it effectively removed excess 11-mercapto-1-undecanol from the functionalized silica-coated iron oxide nanoparticles. Different wash conditions to remove excess 11-mercapto-1-undecanol were tested (Appendix A). Supernatants from different wash conditions were collected and added to the gold nanoparticle solution. When 11-mercapto-1-undecanol is coated onto the gold nanoparticles, these nanoparticles become hydrophobic and agglomerate when dispersed in water. This leads to a change in the color of the NP suspension to a dark purple color from an initially bright red solution. If there is 11-mercapto-1-undecanol left in the supernatant of the wash solution, the color of the gold nanoparticle solution will turn to a darker shade of purple. If there is no 11-mercapto-1-undecanol left in the supernatant of the wash solution, the color of the gold nanoparticle solution will remain a bright red color. For isopropanol, the gold nanoparticle solution remained bright red solution after the third wash cycle (e.g., see

data in Table A2 in Appendix A). Washing with isopropanol three times was effective at removing the excess 11-mercapto-1-undecanol.

3.3.4. Synthesis of the Gold Nanoparticles (Au NPs)

The gold NPs (Au NPs) were prepared via a modified citrate reduction method.[123] A 250 mL glass round bottom flask and a stir bar (Fisherbrand stir bar, 7 mm x 2.5 mm) were cleaned by immersion in aqua regia (3:1, v/v, $HCl:HNO_3$) for 15 min. These acid cleaned supplies were rinsed several times with DI water. This cleaning process was repeated using a piranha solution (7:2, v/v, H_2SO_4:H_2O_2). These supplies were further rinsed with DI water. *CAUTION: Aqua regia and piranha solutions are extremely corrosive. These solutions should be handled with extreme care.* A solution of gold salt (5.11 mM $HAuCl_4$) was prepared in DI water one day prior to the synthesis of the Au NPs to maximize the dissolution of the gold salt. A portion of this solution was diluted from 1.45 mL to 50 mL using DI water and transferred to the precleaned 250 mL round bottom flask. A water-cooled condenser was attached to this flask prior to heating the solution. The solution was subsequently stirred with a magnetic stir bar while heating to 100 °C using a heating mantle connected to a variable current controller (GC-15005-01, Chemglass, USA). While heating the gold salt solution, 5 mL of a 4.46 mM solution of sodium citrate tribasic dihydrate was separately prepared and heated for 10 min at 60 °C using a water bath. Upon boiling the solution of gold, the hot solution of sodium citrate tribasic dihydrate was added all at once to the stirred solution in the round bottom flask. The mixture was heated for an additional 10 min before removing the heat and allowing the stirred flask to cool to room temperature. The as-synthesized Au NPs were isolated from the unreacted excess gold salts through centrifugation (Thermo Electron Corporation, IEC microlite microcentrifuge) at 9,500 rpm (8,400 *g*) for 15 min, decanting of the supernatants and re-dispersion of the isolated solids in DI water with the assistance of a vortexer for 3 min.

3.3.5. Assembly of Au NPs onto the Silica-Coated Fe_3O_4 NPs

A solution of Au NPs (10 nM in 0.1 mL water), a solution of silica-coated iron oxide NPs (1 mg in 0.1 mL isopropanol) and a solution of $mPEG_{5000}$-SH (10 µL, 3% w/v in water) were mixed in a 1.5 mL Eppendorf tube (VWR, 89000-028). This mixture was agitated on an orbital shaker at 250 rpm (VWR orbital shaker, VWR 57018-754) for 1 h

at room temperature while covered with aluminum foil to prevent exposure to ambient light. After this process, the magnetic NPs were isolated from the excess reagents, including freely suspended Au NPs, through the use of external magnets. The isolated solids were washed three times with isopropanol. During this process, the magnetic particles were suspended in 1 mL of isopropanol with the assistance of vortexing for 3 min followed by sonicating for another 3 min. This procedure for assembling the Au NPs onto the magnetic core-shell particles was used, as outlined above, regardless of the surface chemistry on the silica-coated iron oxide NPs. When evaluating the influences on the self-assembly process of adding non-covalently interacting surfactants with the particles, the amount of each surfactant added to the suspension was maintained in place of the $mPEG_{5000}$-SH.

3.3.6. Characterization of the NPs and Their Assemblies

The concentration of Au NPs in solution was estimated using extinction spectroscopy.[124] The extinction spectra of the suspensions of Au NPs were obtained using an 8453 UV-Vis spectrometer from Agilent (USA). Cuvettes used for these measurements were Fisherbrand™ disposable cuvettes (Fisher, Catalog #14-955-127) with a fixed path length of 1 cm. The peak maxima at 521 nm associated with the plasmon resonance of the Au NPs were used when determining the particle concentration. The extinction coefficient for these particles (8.78×10^8 $M^{-1}cm^{-1}$) was obtained from prior art.[124]

Analyses of the particles by transmission electron microscopy (TEM) and energy dispersive X-ray spectroscopy (EDS) were obtained using an FEI Tecnai Osiris operating at 200 kV (Thermo Fisher, USA). Dimensions of the NPs were estimated through TEM analyses by measuring between 20 and 50 particles per sample set. Tomographic analyses by TEM were obtained by tilting the sample from +60° to −60° using a Fischione advanced TEM tomography holder (Model 2020, USA). The TEM images used for the tomography reconstruction were obtained at a tilt of every 2°. The reconstruction was performed by Inspect 3D (Thermo Fisher, USA), and the data visualized by Amira 6.5 (Thermo Fisher, USA).

The number of Au NPs attached to the surfaces of the silica-coated Fe_3O_4 NPs were calculated through TEM analyses. For these measurements, the average number

of Au NPs was determined by assessing at least 5 randomly chosen different core-shell particles observed in the TEM samples. As the projected bright field TEM images only clearly depict the NPs on one side of the assemblies, it was assumed that the number of Au NPs would be equal on the bottom of the Fe_3O_4 NPs. The number of Au NPs coated on the core-shell particles in the projected images was, therefore, doubled for the reported values. The TEM tomographic analyses indicated that this was a valid assumption given the uniformity of the coatings observed for the thiol-functionalized magnetic NPs.

The Ellman's Test was used to quantify the amount of thiol functional groups present on the surfaces of the core-shell particles after reacting with 11-mercapto-1-undecanol. The purified particles were suspended in isopropanol. A calibration curve for the Ellman's Test was established using a series of standards containing 11-mercapto-1-undecanol (i.e., 0 mM, 0.08 mM, 0.17 mM, 0.25 mM, 0.33 mM, 0.41 mM, and 0.50 mM 11-mercapto-1-undecanol) each prepared by dissolving 11-mercapto-1-undecanol in isopropanol. A portion of each sample (250 µL of the particles in isopropanol) or the standard solutions of 11-mercapto-1-undecanol (250 µL, prepared in isopropanol) were each separately mixed with 2.5 mL aliquots of 0.1 M sodium phosphate buffer and 50 µL of the Ellman's reagent (4 mg/mL, suspended in 0.1 M sodium phosphate buffer). These solutions were agitated with the assistance of a vortexer (Vortex-Genie 2, Scientific Industries, USA) for 15 min before obtaining an absorbance spectrum for each mixture with an Agilent 8453 UV-Vis spectrometer. These assessments were performed at room temperature. The concentration of thiol functional groups present on the surfaces of the NPs was estimated from the standard curve.

The density of thiols on the surfaces of the magnetic particles was estimated using the quantitative results from the Ellman's Test and the total surface area estimated for the silica-coated Fe_3O_4 NPs. The number of thiol groups in a sample was determined using the standardized results from the Ellman's Test. The total available surface area on each core-shell nanoparticle was calculated using the following steps: (i) the total number of NPs in a sample was calculated using the mass of silica-coated Fe_3O_4 NPs used for the Ellman's Test in combination with the density of these materials and the average volume per NP; (ii) the density of the Fe_3O_4 NPs was estimated to be 5.19 g/cm^3, and the density of the silica shell was estimated to be 1.90 g/cm^3;[78] (iii) the average volume of the silica shell and the Fe_3O_4 core were each determined from TEM

based measurements; and (iv) the total collective surface area of particles in the sample was calculated by multiplying the estimated total number of NPs by the nominal surface area per nanoparticle, which was also estimated using particle diameters obtained from the TEM measurements and assuming each particle had a spherical shape.

3.4. Results and Discussion

Formation of Au NP assemblies on the core-shell structure visually illustrated the grafting of thiolated reagents onto the silica-coated Fe_3O_4 NPs (Fig. 3.2). A methoxy-terminated poly(ethylene glycol) thiol ($mPEG_{5000}$-SH) was added to the suspension to reduce aggregation of the NPs during the assembly process. These conditions were optimized through a series of experiments, including a number of control studies, as outlined in further detail below. The average diameter of the Fe_3O_4 NPs was approximately 250 nm and the silica coatings had an average thickness of 70 nm (Fig.3.3, and Fig. B1 in Appendix B). There are two distinctive layers to the silica-coated and functionalized NPs. These layers are further differentiated through the TEM tomography data and the EDS analyses (e.g., Fig. 3.6, and Fig. 3.7). The Fe_3O_4 core is much darker and dense layer than the silica coating. The less dense and grey layer is the silica coating. The X-ray diffraction analysis of these NPs confirms that the phase of the Fe_3O_4 is magnetite (Fe_3O_4) (Fig. 3.4). The average diameter of the Au NPs was 20 nm (Fig. 3.5). These particles can be easily distinguished from each other by the difference in their size. The purified assemblies were assessed by transmission electron microscopy (TEM) and energy dispersive X-ray spectroscopy (EDS) based analyses to confirm the composition of the resulting assemblies (Fig. 3.6 and 3.7). A high number of Au NPs were assembled onto the silica-coated Fe_3O_4 NPs, suggesting a successful attachment of thiol functionalization. Elemental mapping by EDS further confirmed the composition of each component in these assemblies (Fig. 3.6d and 3.7). Tomographic analyses by TEM were performed to verify the surface coverage of the Au NPs. A uniform distribution of Au NPs was observed over all surfaces of the magnetic NPs (Fig. 3.8). The average number of Au NPs per assembly was determined by assessing the TEM data from 5 different core-shell particles. These assemblies contained approximately 320 ± 90 Au NPs per Fe_3O_4 core.

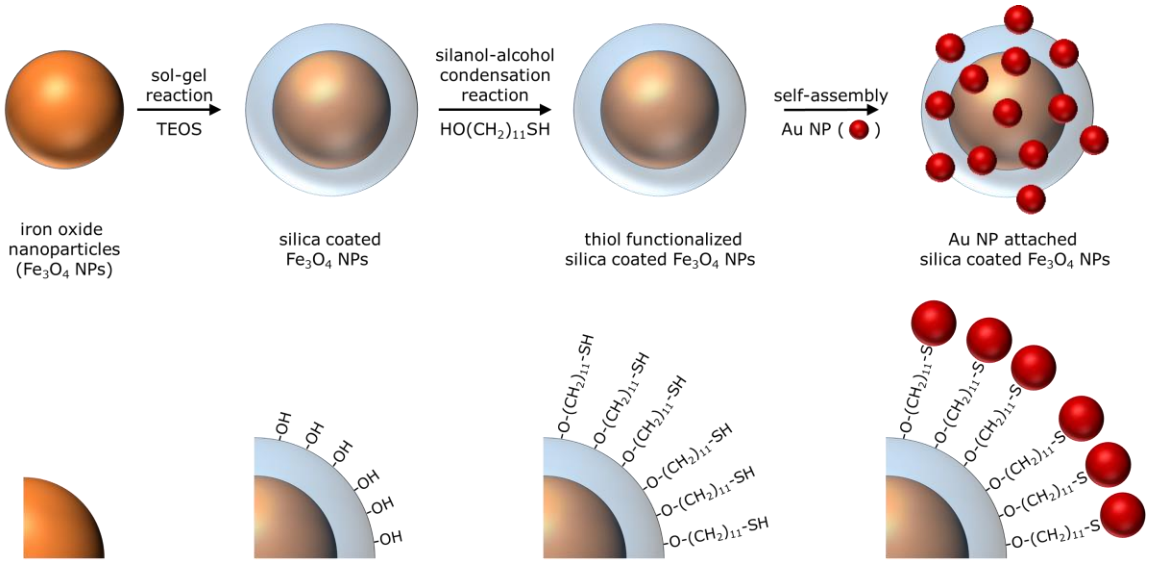

Figure 3.2 **Representative schematic diagram of thiol functionalization of silica-coated iron oxide nanoparticles (Fe_3O_4 NPs) achieved using the silanol-alcohol condensation reaction. This diagram is not drawn to scale.**

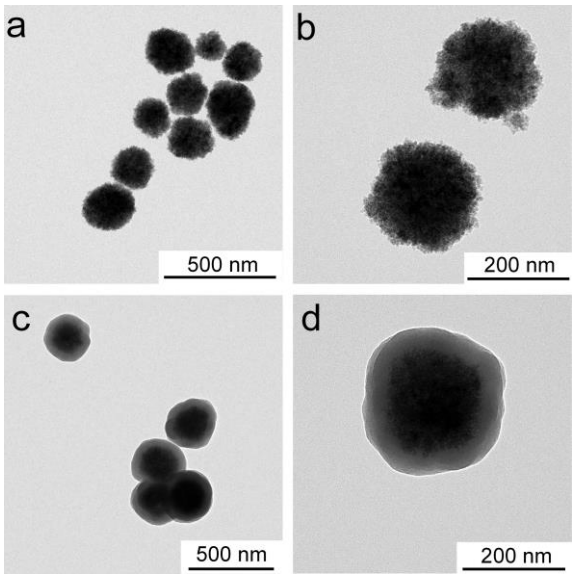

Figure 3.3 **Transmission electron microscopy (TEM) analyses of (a,b) the Fe_3O_4 NPs, and (c,d) the silica-coated Fe_3O_4 NPs.**

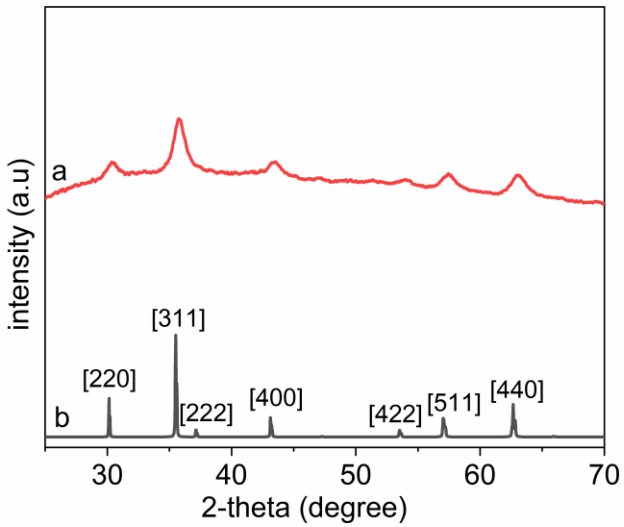

Figure 3.4 **Powder X-ray diffraction patterns for: (a) Fe_3O_4 nanoparticles prepared by the described solvothermal synthesis; and (b) a reported Fe3O4 reference (ICSD no. 35000).**

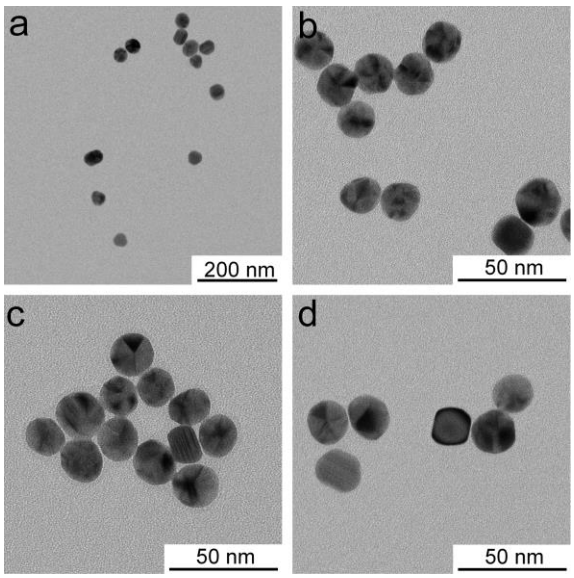

Figure 3.5 **Representative TEM analyses of the gold nanoparticles (Au NPs).**

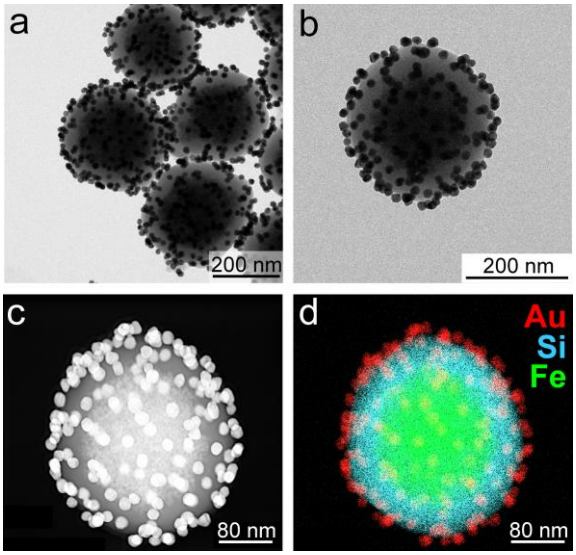

Figure 3.6 **Assemblies of gold nanoparticles (Au NPs) attached to thiol functionalized core-shell NPs of silica-coated Fe_3O_4 as characterized by (a,b) transmission electron microscopy (TEM); (c) high-angle annular dark-field (HAADF) imaging as performed by scanning TEM; and (d) energy dispersive X-ray spectroscopy (EDS). The thiol-functionalized silica surfaces were prepared by a silanol-alcohol condensation reaction.**

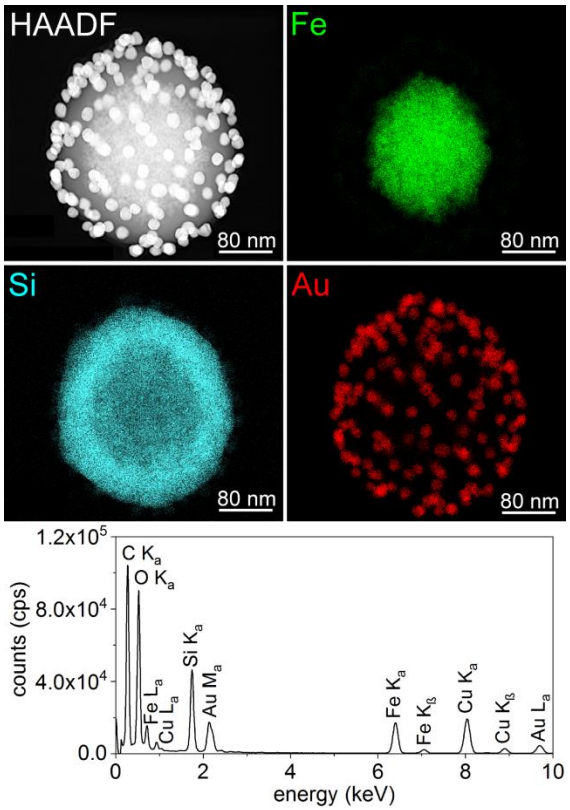

Figure 3.7 **Energy dispersive X-ray spectroscopy (EDS) analysis of the Au NPs assembled onto the surfaces of a thiol functionalized, silica-coated Fe_3O_4 NPs. These images show the high-angle annular dark field (HAADF) image obtained by scanning TEM techniques, and EDS maps of Fe, Si, and Au within these assemblies. A representative EDS spectrum is also included, depicting the composition of the assembly along with contributions from the copper TEM grid.**

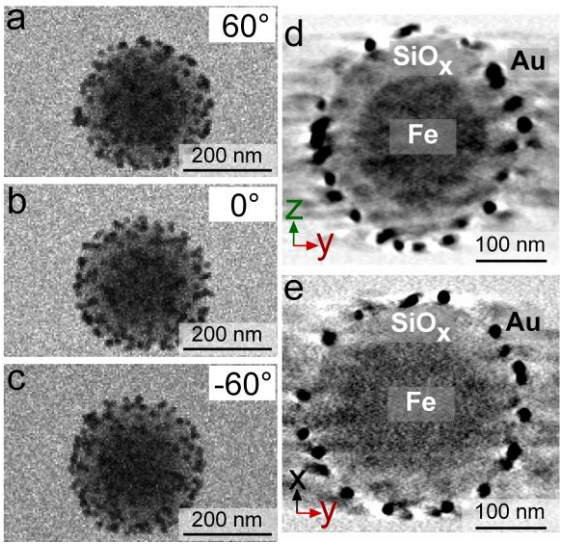

Figure 3.8 **Tomographic analyses performed by TEM techniques of Au NPs assembled onto the surfaces of the magnetic core-shell nanoparticles, which had been functionalized with 11-mercapto-undecanol. A series of TEM images were acquired, including at tilts of (a) +60°, (b) 0° and (c) -60°. Representative orthoslices of (d) the yz-plane and (e) the xy-plane show the distinct layers of these assemblies.**

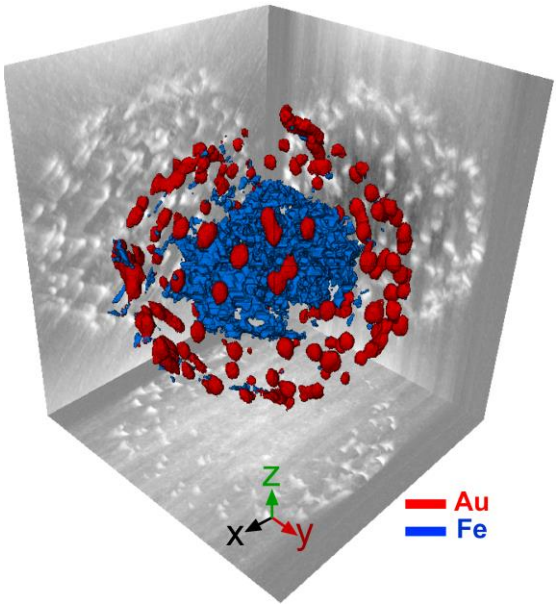

Figure 3.9 **A representative three-dimensional rendering produced from the tomographic data associated with the assemblies displayed in Fig. 3.7. This rendering was prepared from the reconstruction of a series of aligned images obtained at every 2° between +60° and -60°.**

The thiols covalently attached to the surfaces of the particles were quantified through the Ellman's Test, an assay. The Ellman's Test has been widely used as a colorimetric assay for quantifying thiols in a range of samples.[106,125] These uses include quantifying the amount of thiol functional groups available on the surfaces of NPs.[113] A calibration curve was prepared from standard solutions containing 11-mercapto-1-undecanol at concentrations ranging from 0 to 0.50 mM (Fig. 3.10). The thiolated reagents did not readily dissolve in the phosphate buffer. Isopropanol was used instead for the dissolution of this thiol species. The samples containing thiol-functionalized NPs were also dispersed in the same amount of isopropanol prior to mixing with the phosphate buffer used in the Ellman's Test. From these analyses, it was estimated that each thiol group occupies a surface area of approximately 1.9 ± 0.1 nm^2, or 0.53 thiols nm^{-2} on the magnetic NP. A previous study suggested an average surface coverage of 4.6 silanols nm^{-2} depending on the method used to prepare the silica.[126] This prior study also suggested that the accessibility of the silanol groups for further reactivity depends on the degree of surface hydration. These results suggest that many of the silanol groups were reacted with the thiolated reagents, but that likely the process could be optimized further in the future. In the absence of heating the solution during the functionalization step (i.e., without inducing the silanol-alcohol condensation reaction), the surface coverage of thiol groups decreased to one group per approximately 7.3 ± 1.2 nm^2 or 0.14 thiols nm^{-2}. This lower surface coverage was attributed to non-specific adsorption of 11-mercapto-1-undecanol onto the silica. An elevated reaction temperature was required to functionalize the surfaces through the condensation reaction. The formation of disulfide bonds between the surface thiol functional groups would not likely happen. Previous literature shows that the disulfide bond formation between two different 12-mercapto-1-dodecanol molecules can be achieved when the reaction was performed under reflux in presence of an acid.[127] Other literature achieved the formation of a disulfide bond with the presence of an oxidizing agent, such as sodium iodide.[128] For this study, the 11-mercapto-1-undecanol was incubated with silica-coated Fe_3O_4 NPs under heat without presence of acid or oxidizing agent. The disulfide bond between 11-mercapto-1-undecanol species would, therefore, not be very likely happen under the conditions pursued herein.

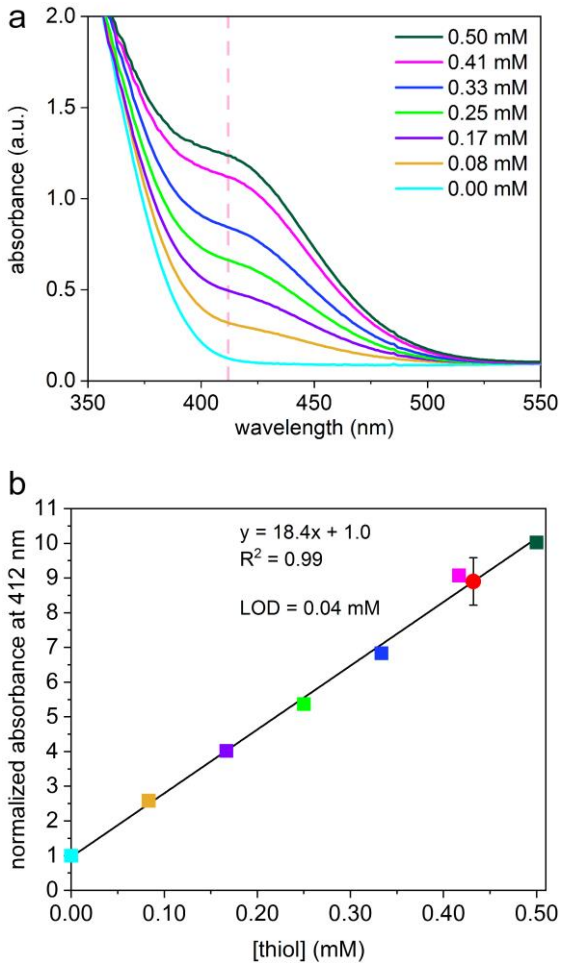

Figure 3.10 **(a) Absorbance spectra from the Ellman's Test for a series of standards prepared from 11-mercapto-1-undecanol at the concentrations noted in the legend. The response of each standard to the Ellman's Test was recorded as a function of its absorbance at 412 nm, as indicated by the dashed vertical pink line. (b) A calibration curve was prepared from these standard solutions containing increasing concentrations of 11-mercapto-1-undecanol. The red circle on this plot indicates the concentration of thiols associated with the core-shell particles functionalized with 11-mercapto-1-undecanol via a silanol-alcohol condensation reaction.**

Formation of the assemblies with bare, silica-coated Fe_3O_4 NPs verified whether covalent attachment of a thiol functionalized surface coating was required for the formation of the Au assemblies. These assemblies had a significantly lower number of Au NPs associated with the magnetic particles with an average of only 6 ± 3 Au NPs per Fe_3O_4 core (Fig. 3.11a and b). All parameters for the assembly process were held constant. These results indicated that neither the addition of $mPEG_{5000}$-SH to the suspension or potential electrostatic interactions between the particles drive the assembly processes. The formation of assemblies was also evaluated using Fe_3O_4 NPs that were only incubated with the thiol functionalized alcohol reagent at room temperature (i.e., not at elevated temperatures). The resulting assemblies had approximately 16 ± 16 Au NPs per magnetic particle. The relatively large standard deviation in these results was due to the high disparity in the number of attached Au NPs (Fig. 3.12). These results suggest that the alcohol reagent can interact in a non-uniform manner through non-specific binding with the silica surfaces, but that elevated temperatures were required to achieve a more uniform and dense surface coverage of the alcohol reagent. The successful, uniform assembly of Au NPs onto the silica required the covalent attachment of the thiol functionality to the surfaces of the magnetic NPs. These results provided an indirect method of verifying the thiol functionalization of the silica.

The conditions for preparing the assemblies were also optimized by tuning a series of variables. Different reagents were used to assess their impact on the stability of the Au NPs during the assembly process. These surfactants were mixed with the Au and the silica-coated Fe_3O_4 NPs, replacing the thiolated $mPEG_{5000}$. These surfactants included polyvinylpyrrolidone (PVP, MW: 10,000), sodium dodecyl sulfate (SDS), and two different poly(ethylene glycols) (PEGs): PEG_{200} (MW: 200) and PEG_{5000} (MW: 5,000). Each of these reagents was evaluated for their ability to assist in the formation of the desired assemblies. All other conditions were held constant during the processes for purification and assembly with the thiol coated magnetic NPs. The isolated products were assessed by TEM (Fig. 3.11). The inclusion of these reagents tended to increase the number of Au NPs attached to the silica in comparison to samples prepared in the absence of additional surfactants. Relatively few Au NPs were, however, attached to the magnetic cores following the assembly process when using non-covalently interacting surfactants, in contrast to assemblies prepared in the presence of $mPEG_{5000}$-SH. In all

cases, except for the addition of $mPEG_{5000}$-SH, the Au NPs did not form uniform assemblies over the silica surfaces. The $mPEG_{5000}$-SH likely minimized aggregation of the NPs during attachment of the Au to the thiol functionalized silica surfaces. The $mPEG_{5000}$-SH was necessary to achieve a relatively high loading and an even coverage of Au NPs on the magnetic particles. The addition of $mPEG_{5000}$ did not have comparable result to the addition of $mPEG_{5000}$-SH, as $mPEG_{5000}$ did not readily dissolve in the isopropanol.

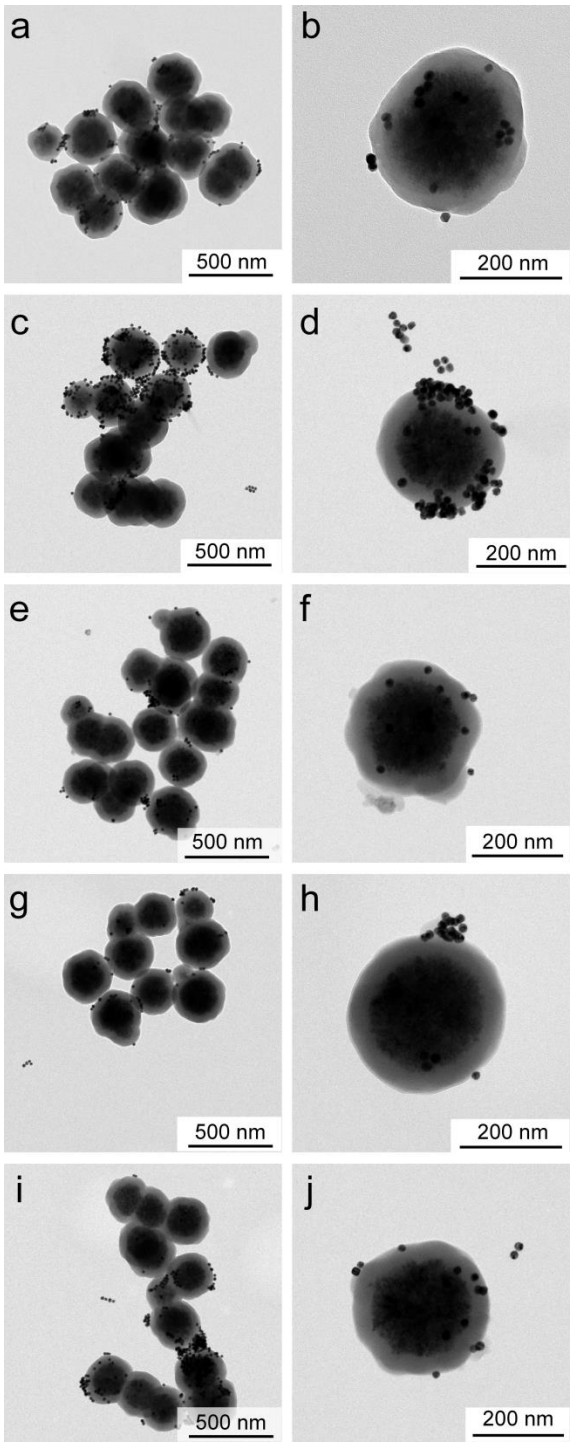

Figure 3.11 **The TEM analyses of samples prepared by mixing with Au NPs thiol functionalized core-shell nanoparticles with the addition of (a,b) no additives, (c,d) sodium dodecyl sulfate (SDS), (e,f) polyethylene glycol (PEG) (MW 5,000), (g,h) polyvinylpyrrolidone (PVP), and (i,j) PEG (MW 200).**

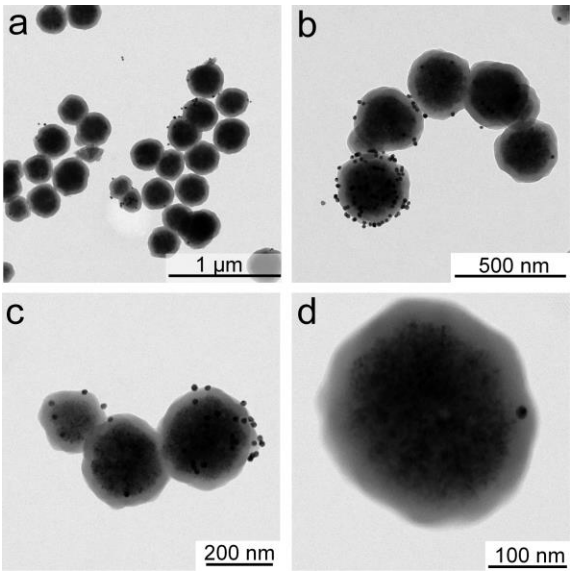

Figure 3.12 Representative images from the TEM analyses of samples prepared by mixing Au NPs with the Fe_3O_4 NPs that were incubated with thiol alcohol reagent at room temperature (i.e., without using elevated heating to trigger the silanol-alcohol condensation reaction).

The assembly process was further tuned by adjusting the concentration of both the Au NPs and the thiol functionalized Fe_3O_4 NPs. These adjustments were correlated to changes in the loading of Au NPs on the magnetic cores. The concentration of the Au NPs was reduced from 10 nM to 1 nM, and Fe_3O_4 NPs concentrations were reduced from 4.7 to 0.94 nM. The formation of the sought after assemblies are governed by the solvent properties and the inclusion of specific surfactants.[129,130] In our system, thiol functionalized Fe_3O_4 NPs were not stable in water, but relatively stable in isopropanol. The addition of PEG-SH were stabilized both types of NPs in the isopropanol and water mixture. At the lower concentrations, not surprisingly, the assemblies contained fewer Au NPs. These assemblies contained an average of 12 ± 3 Au NPs per Fe_3O_4 particle (Fig. 3.12a). When the concentrations of both types of NPs were increased, the average loading of Au NPs increased to 320 ± 90 Au NPs per Fe_3O_4 NPs (Fig. 3.13). The PEG-SH stabilized the Fe_3O_4 NPs through non-covalent surface interaction.

The solvent plays a critical role in the formation of the assemblies. Tuning the nanoparticle assemblies can be performed through changes to a miscible solvent mixture or the ionic strength of the solution.[129,130] In this thesis, the thiol functionalized silica-coated Fe_3O_4 NPs are stable in isopropanol, but they are not colloidal in water. The Au NPs are, in contrast, stable in water and in the mixture of isopropanol and water. The thiol functionalized NPs will precipitate out of solution over time if they are not

otherwise stabilized upon mixing the Fe_3O_4 NPs in isopropanol with the aqueous dispersion of Au NPs. The thermodynamically stable configuration is the formation of Au NPs assembled onto the surfaces of the thiol functionalized magnetic NPs.

In this study, the $mPEG_{5000}$-SH was added a couple of minutes after mixing the solution of thiol functionalized silica-coated Fe_3O_4 NPs and Au NPs. The PEG-SH has a favourable interaction with the surfaces of the thiol functionalized silica-coated Fe_3O_4 NPs. The PEG-SH interacts with the coatings prepared by the silanol-alcohol condensation reaction, stabilizing these hydrophobic residues against aggregation within the aqueous solution. Once the PEG-SH reagents interact with the surfaces of the magnetic NPs it will, however, be difficult for Au NPs to access the remaining thiols groups on the surfaces of the magnetic NPs. The PEG-SH reversibly interact with the surfaces of the thiol capped Fe_3O_4 NPs. These interactions will, however, make it difficult for Au NPs to access the thiols on the surfaces of the Fe_3O_4 NPs. Holding all other conditions equal, a decrease in the concentration of Fe_3O_4 NPs led to a lower surface coverage of Au NPs (Fig. 3.13a and 3.13c). If the amount of PEG-SH was also decreased to maintain a constant ratio of PEG-SH to Fe_3O_4 NPs, the number of Au NPs in the assemblies also increased (Fig. 3.14). Hence, the PEG-SH is added after allowing the particles to interact for an initial period of time to initiate formation of the clusters before passivating the surfaces of thiol functionalized Fe_3O_4 NPs.

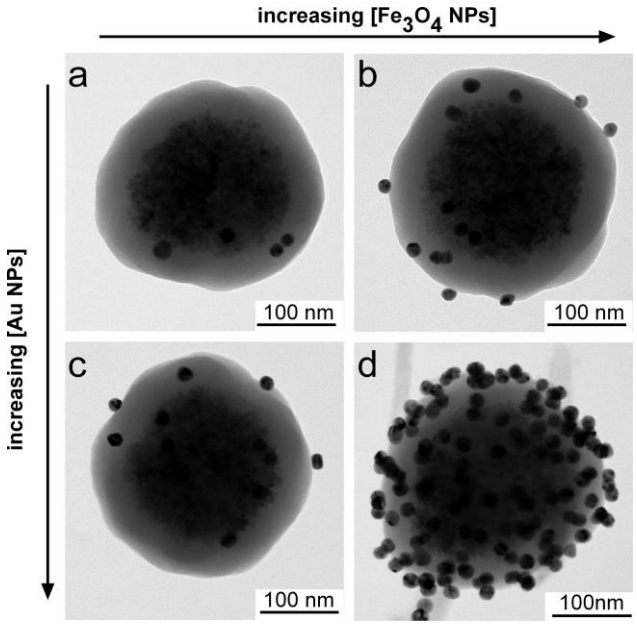

Figure 3.13 **Representative TEM images of Au NPs assembled onto the thiol-functionalized core-shell particles as prepared by varying the concentration of both the Au NPs and the magnetic nanoparticles. The direction of increasing concentration of each type of particles is indicated by the arrows adjacent to the images.**

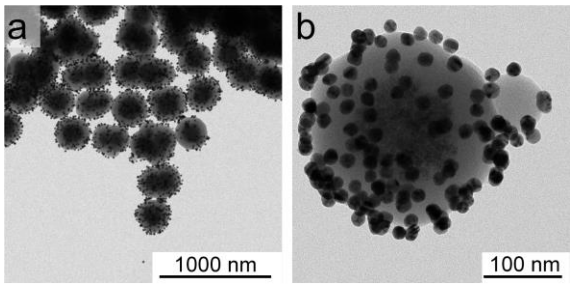

Figure 3.14 **The representative TEM analyses of the sample prepared by mixing 10 nM of Au NPs with 0.94 nM of the thiol functionalized core-shell magnetic NPs with addition of 0.06% (w/v) $mPEG_{5000}$-SH. The amount of $mPEG_{5000}$-SH in this sample was adjusted to maintain the same ratio of Fe_3O_4 NPs to PEG-SH that was used to prepared the majority of the assemblies.**

Table 3.1 Quantification of the number of Au NPs per thiol functionalized core-shell nanoparticle as a function of varying the concentration of both the magnetic NPs and the Au NPs.

[Fe_3O_4 NPs]	[Au NPs]	[PEG-SH]	# of Au NPs per magnetic particle [a]
0.94 nM	1.0 nM	0.3 % (w/v)	12 ± 3
4.7 nM	1.0 nM	0.3 % (w/v)	43 ± 12
0.94 nM	10 nM	0.3 % (w/v)	18 ± 6
4.7 nM	10 nM	0.3 % (w/v)	320 ± 90
0.94 nM	10 nM	0.06% (w/v)	190 ± 40

[a] Mean values calculated for each sample along with the distribution from these means reported as one times the standard deviation. These values were each calculated from a sample of at least 5 separate core-shell particles.

The silanol-alcohol condensation reaction could be utilized to expand the surface chemistry of silica-coated NPs. These additional functional groups also served as further controls to assess the specificity of self-assembling Au NPs onto silica-coated magnetic cores. Additional reagents included molecules with a linear hydrocarbon backbone and either a terminal carboxylic acid or alcohol (i.e., a diol). For example, 11-hydroxyundecanoic acid or 1,10-decanediol were grafted onto the silica surfaces using the same procedures developed for covalently attaching the thiolated reagents. All other conditions were held constant during these processes, including the steps of assembly and sample purification. The carboxylic acid functionalized magnetic NPs displayed a mildly favourable interaction with the Au NPs (38 ± 7 Au NPs per core particle). The diol functionalized magnetic NPs had fewer Au NPs attached to their surfaces with 21 ± 9 Au NPs per core particle (Fig. 3.15 and Fig. 3.16). The incorporation of a thiol functionalization was a key factor for the successful formation of the desired assemblies. The additional surface functionalities demonstrated herein could, however, be used in the future to attach other species or functional moieties onto these cores.

Table 3.2 Quantification of the number of Au NPs on the surfaces of the magnetic particles with different functionalities[+]

type of functionalization	# of Au NPs per magnetic particle[a]
native silica surfaces	6 ± 3
room temperature incubation with 11-mercapto-1-undecanol	16 ± 16
carboxylic acid functionalization (11-hydroxyundecanoic acid)	38 ± 7
alcohol functionalization (1,10-decandiol)	21 ± 9
thiol functionalization (11-mercapto-1-undecanol)	320 ± 90

[+] All particles were prepared from a shell of silica on an iron oxide core.

[a] Mean values calculated for each sample along with the sample variance reported as one time the standard deviation from the mean. These values were each calculated from a sample of at least 5 separate core-shell particles.

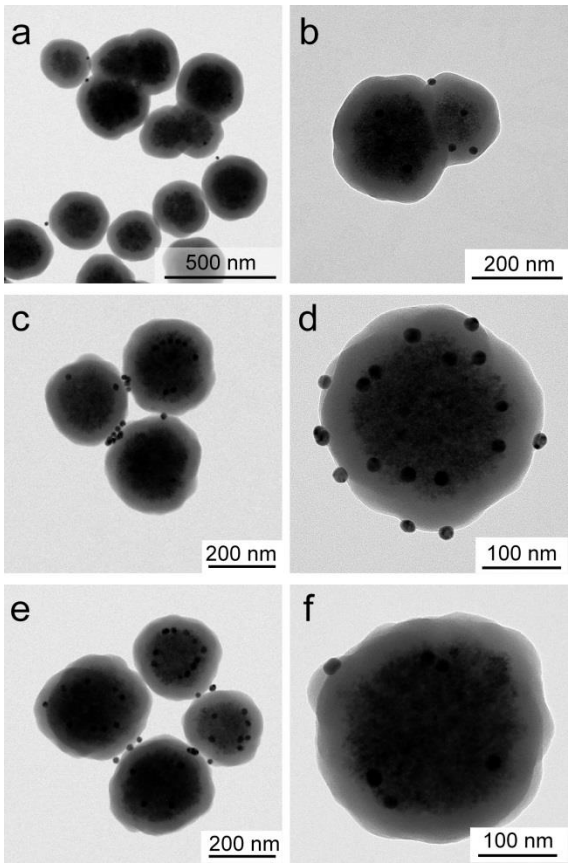

Figure 3.15 **The TEM analyses of particles prepared from mixing Au NPs with (a,b) silica-coated Fe_3O_4 NPs, (c,d) carboxylic acid (11-hydroxyundecanoic acid or HDA) functionalized core-shell nanoparticles, and (e,f) alcohol (1,10-decandiol) functionalized core-shell nanoparticles.**

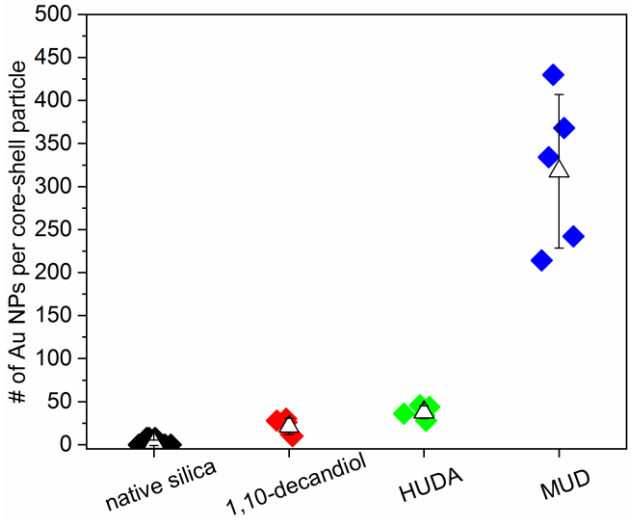

Figure 3.16 **Scatter plot of a number of Au NPs on the surfaces of the functionalized silica-coated Fe_3O_4 NPs. The white triangles represent the calculated mean values and the error bars represent one standard deviation from these means.**

3.5. Conclusions

We demonstrated the functionalization of silica-coated Fe_3O_4 NPs with a thiol terminated linear alcohol reagent through the silanol-alcohol condensation reaction. The Ellman's Test was used to quantify the surface thiol content. It was calculated that these surfaces were covered with 0.53 thiols per nm^2. As a demonstration of a successful surface functionalization, we formed assemblies of Au NPs on the silica-coated Fe_3O_4 NPs. The covalent attachment of alcohol reagents was extended to a carboxylic acid species and a diol. Through covalently linking other alcohol species to the silica through the silanol-alcohol condensation reaction, this process could be utilized for a range of applications in future studies. In addition to driving the assembly of Au NPs onto thiol functionalized magnetic particles, the covalent attachment of alcohols onto the surfaces of silica particles enables further tuning of their surface chemistry through use of widely available and relatively stable reagents.

Chapter 4. One-pot Preparation of Multi-functional Silica-Coated Iron Oxide Nanoparticles Using the Microwave-Assisted Silanol-Alcohol Condensation Reaction

4.1. Notice of Permission

A manuscript based on the work described in this chapter is currently being prepared for a publication. The majority of the work presented in this chapter has been performed by myself, including experiments, data acquisition and writing, under the supervision of Dr. Byron Gates. Ms. Audrey Taylor performed the XPS analyses and Mr. Faryad Rana Ali provided advice on the synthesis and characterization of iron oxide nanoparticles. Ms. Melissa J. Radford and Ms. Stephanie Sonea provided assistance in quantifying the thiol surface coverage on the functionalized silica-coated iron oxide nanoparticles.

4.2. Introduction

The surface modification of nanoparticles is important as this chemistry is closely related to the properties of the nanoparticles. Often the surface chemistry used during the synthesis of a nanoparticle is not the same as the desired, final form of the surface chemistry. One of the ways for tuning their surface functionalization is through a ligand exchange at the surfaces of nanoparticles. A previous study has, however, demonstrated that the ligand exchange of catechol on the surfaces of iron oxide nanoparticles could etch iron out of magnetite nanoparticles.[69] Other methods for the surface functionalization of these Fe_3O_4 nanoparticles include silica coating. A silica coating can minimize the magnetic interactions between nanoparticles and, thus, reduce particle agglomeration.[75] As the silica coating acts as a protective layer, it could minimize the etching of iron from the nanoparticles. Different functionalities, such as linkers to a biomolecule, can be prepared by covalently modifying the surfaces of silica-coated iron oxide nanoparticles.[131–134] A common approach to tuning the chemistry of silica capped nanoparticles is the use of silane reagents, such as 3-mercaptopropyltrimethoxysilane (3-MPTMS), or (3-aminopropyl)triethoxysilane (APTES).[80–82] These silane reagents are

susceptible to side reactions and tend to form multilayers on the surfaces of nanoparticles.[88] The co-deposition of two different silane reagents onto the silica surfaces can be a challenge for controlling the ratio of the two reagents in a one-pot process.[135–137] Although this approach to modify the surfaces of silica has been widely adopted, it can be challenging to reproduce. Alternative methods with more control over the reaction kinetics are desirable.[91]

Silica surfaces can also be functionalized through the silanol-alcohol condensation reaction.[71,73,75] This condensation reaction modifies silica surfaces by covalently attaching alcohol reagents to the silica. Unlike silane-based reagents, alcohol-based reagents are relatively stable in the presence of water. Previously, the silanol-alcohol condensation reaction was utilized to covalently attach linear alcohol reagents onto the surfaces of silica-coated iron oxide nanoparticles (Chapter 3). This reaction is relatively slow in comparison to the reaction of silica with reactive silane-based reagents. As a result, this reaction requires longer reaction times and elevated reaction temperatures.[92,94,96] To attach alcohol reagents onto silica surfaces more effectively and efficiently, different strategies have been previously pursued. One of these alternative methods is the use of microwave radiation to initiate the reaction. Microwave radiation has been shown to heat reactions more effectively than convective heating, such as through the use of an oil bath.[96] Microwave radiation has been widely used to initiate reactions in organic synthesis,[138,139] and material science.[53,140,141] It has also been used to initiate the silanol-alcohol condensation reaction on planar, silica-coated substrates.[96] The silanol-alcohol condensation reaction assisted by microwave radiation was shown to be more efficient than the condensation reaction achieved through convective heating with an oil-bath.

In this study, the silanol-alcohol condensation reaction was tuned by simultaneously functionalizing silica-coated NPs with two different alcohol reagents. This one-pot approach is desirable to avoid a multi-step surface functionalization. We have previously achieved a well-tuned surface coating through the silanol-alcohol condensation reaction.[94,96,97] This process can be used to tune the hydrophobic and oleophobic properties of a planar silica-coated substrate through preparing a mixed monolayer of a hydrocarbon and a perfluorocarbon species. In the case of the NPs, we adjusted the ratio of 11-mercapto-1-undecanol (a thiol containing alcohol reagent) and 12-hydroxy-1-dodecanoic acid (a carboxylic acid containing alcohol reagent) in the

reaction mixture as a demonstration of preparing monolayers of a mixed functionality. This silanol-alcohol condensation reaction was performed using microwave-assisted heating. The functionalization of the NPs following this reaction was assessed through the use of the Ellman's Test, a colorimetric assay. An increasing concentration of 11-mercapto-1-undecanol in the reaction mixture should be correlated with an increase in the thiol content of the surfaces of the functionalized NPs. The surface functionalities formed simultaneously via the silanol-alcohol condensation reaction were further verified through X-ray photoelectron spectroscopy (XPS) analyses. The XPS analyses were used to assess the composition of these surface coatings. Higher resolution XPS analyses of the carbon species identified the presence of thiol and carboxylic acid functionalization on the surfaces of the NPs. We also compared the results of initiating the silanol-alcohol condensation reaction with microwave radiation to the prior work in Chapter 3 using convective heating methods.

4.3. Experimental

All of the chemicals were of analytical grade and were used as received without further purification. Iron (III) chloride hexahydrate (97%), gold (III) chloride trihydrate (≥99.9%), sodium citrate tribasic dihydrate (ACS reagent, ≥99.0%), sodium dodecyl sulfate (≥98.5%), propylene carbonate (99%), polyethylene glycol monomethyl ether (PEG, 100%, 5,000 MW), (3-mercaptoproyl)-trimethoxysilane (95%), and tetraethyl orthosilicate (98%) were all obtained from Sigma-Aldrich (USA). Chemicals such as 11-mercapto-1-undecanol (97%), 12-dodecanoic acid (96%), and polyvinylpyrrolidone (≤100%, 10,000 MW) were all obtained from Aldrich. An aqueous solution of ammonium hydroxide (28% to 30% v/v in water) was obtained from BDH (USA). Ellman's reagent (95 to 100%, lot # TC262582) was obtained from Thermo Scientific (USA). Urea (99%) and hydrogen peroxide (a 30% v/v aqueous solution) were obtained from Fisher Scientific (USA). Polyethylene glycol (PEG, 100%, 200 MW) was obtained from Alfa Aesar (Belgium). Methoxy terminated PEG-thiol ($mPEG_{5000}$-SH, 5,000 MW) was obtained from NanoCS (USA). Hydrochloric acid (36 to 38.5% v/v in water) was obtained from VWR (USA). Nitric acid (68 to 70% v/v in water) was obtained from ACP (USA). Sulfuric acid (95 to 98% v/v in water) was obtained from Caledon (USA). Ultrapure, deionized (DI) water (18.2 MΩ·cm) was obtained using a NANOpure DIamond™ system from Barnstead (USA).

4.3.1. Synthesis of Iron Oxide Nanoparticles (Fe_3O_4 NPs)

Iron oxide nanoparticles (NPs) were synthesized via a modified solvothermal method.[54] Iron (III) chloride hexahydrate (0.12 M), urea (1.0 M), and sodium citrate tribasic dihydrate (0.06 M) were mechanically stirred in ethylene glycol (10 mL) for 60 min. This solution was then transferred to a Teflon lined stainless-steel autoclave (Model No. 4749, Parr Instruments Co., Moline, IL, USA). This autoclave was sealed and heated at 200 °C for 8 h. After 8 h, this solution was cooled to room temperature. The isolated black particles were washed three times with 20 mL of ethanol. The isolation of the magnetic NPs during the washing steps was performed using an external magnet. After the third wash, the NPs were dried in an oven at 70 °C for 2 h.

4.3.2. Silica Coating of the Fe_3O_4 NPs

The magnetic NPs were coated with a layer of silica using a Stöber sol-gel process.[77] Dried magnetic NPs (10 mg) were suspended in a mixture of 64 mL ethanol and 16 mL DI water. This solution was stirred with an overhead mechanical stirrer (Fisher Scientific, Compact Overhead Stirrer, 50 W output) at a speed of 500 rpm. The ammonium hydroxide (1 mL) was added all at once. Tetraethyl orthosilicate (TEOS, 1 mL) was subsequently added after this step, but in a dropwise manner. The resulting mixture was stirred for 6 h at room temperature. After this process, the particles were washed three times with 20 mL of ethanol. Similar to the purification of the iron oxide NPs, the isolation of the silica-coated NPs were performed using an external magnet.

4.3.3. Functionalization of Silica-Coated Fe_3O_4 NPs Using Oil Bath Assisted Heating

Functionalization of the silica-coated iron oxide NPs was achieved using a modified silanol-alcohol condensation reaction.[94] The silica-coated iron oxide NPs were washed again, but propylene carbonate was used in place of ethanol. The supernatant was removed after isolating the NPs from the solution, and these pelleted solids were suspended into a fresh solution of propylene carbonate. This purification process was repeated one more time to remove traces of ethanol from the solution. The desired alcohol reagent, such as 11-mercapto-1-undecanol, was prepared as a 500 mM solution in 2 mL of propylene carbonate. This solution of alcohol reagent was mixed with the pelleted NPs. The vial containing this solution was sealed with a plastic cap and wrapped in parafilm. A suspension of these NPs was obtained by vortexing the solution for 5 min (Scientific Industries Vortex-Genie 2 Mixer, USA) and sonicating for another 5 min (Bransonic, Ultrasonic cleaner, 50-60 Hz). The sealed container was subsequently heated at 80 °C over 24 h by immersion in an oil bath under magnetic stirring. This temperature can also be easily achieved using water or sand bath assisted heating. The set-up was covered with aluminum foil to reduce exposure to ambient light. After 24 h, the NPs were isolated from the unreacted, excess reagent by use of an external magnet. The isolated NPs were magnetically washed three times with isopropanol as the rinse solution. Following each step of this procedure, the washed NPs were suspended in 10 mL of isopropanol by agitation using a vortexer for 3 min followed by sonication for another 3 min.

4.3.4. Functionalization of Silica-Coated Fe_3O_4 NPs Using a Microwave Reactor

The silica-coated iron oxide NPs were transferred to a glass microwave reaction vessel and washed again with propylene carbonate as the rinse solvent. The supernatant was removed after isolating the NPs from the solution, and these pelleted solids were suspended into a fresh solution of propylene carbonate. This purification process was repeated one more time to remove traces of ethanol from the solution. The desired alcohol reagent, such as 11-mercapto-1-undecanol, was prepared as a 500 mM solution in 6 mL of propylene carbonate. This solution of alcohol reagent was added to a glass microwave reaction vessel containing the pelleted NPs. The mixture was briefly agitated for 3 min using a vortexer. The mixture was inserted into the microwave reactor, an Ethos Plus Microwave Labstation (model ATC-FO 300, Milestone Microwave Laboratory System, USA). The ramp time was set to 3 min with the target temperature of 80 °C. The temperature was held constant for 2 h. The maximum energy output of the microwave reactor was also set to 500 W. After 2 h, the NPs were isolated from the unreacted, excess reagent by use of an external magnet. The isolated NPs were washed three times with isopropanol as the rinse solution. Following each step of this procedure, the rinsed NPs were suspended in 20 mL of isopropanol by agitation using a vortexer for 3 min followed by sonication for another 3 min.

4.3.5. Functionalization of Silica-Coated Fe_3O_4 NPs using Silane Reagents

Previous reports have used toluene as a solvent for reacting thiol functionalized silane reagents with silica-coated iron oxide nanoparticles.[80,142,143] Silica-coated iron oxide NPs were isolated from solution using the external magnet, and these pelleted solids were re-suspended into 15 mL of toluene. The (3-mercaptopropyl)-trimethoxysilane (3-MPTMS) reagent (500 µL in total) was added dropwise to the suspension of particles. The solution was stirred continuously with a magnetic stir bar, and was held at 70 °C (using an oil bath) for 2 h under an atmosphere of nitrogen. After 2 h, the solution was removed from the heat and left to stir overnight at room temperature. After 24 h, the NPs were isolated from the unreacted, excess reagent by use of an external magnet. The isolated NPs were washed two times with ethanol as the rinse solution. Following this purification process, the rinsed NPs were suspended in 20

mL of isopropanol by agitation using a vortexer for 3 min followed by sonication for another 3 min.

4.3.6. Synthesis of the Gold Nanoparticles (Au NPs)

Gold NPs (Au NPs) were prepared via a modified citrate reduction method.[123] All the glassware used for this synthesis was cleaned by immersion in aqua regia (3:1, v/v, $HCl:HNO_3$) for 15 min. These acid cleaned supplies were rinsed several times with DI water. This cleaning process was repeated using a piranha solution (7:2, v/v, $H_2SO_4:H_2O_2$). These supplies were further rinsed with DI water. *CAUTION: Aqua regia and piranha solutions are extremely corrosive. These solutions should be handled with extreme care.* A solution of gold (5.11 mM $HAuCl_4$) was prepared in DI water and stirred for 24 h. This solution was further diluted to 50 mL (0.148 mM $HAuCl_4$) with DI water. This diluted solution was stirred with a magnetic stir bar in a 250 mL round bottom flask while heating to 100 °C using a heating mantle connected to a variable current controller (GC-15005-01, Chemglass, USA). A water-cooled condenser was attached to this flask while heating. Separately, a 5 mL solution of a 4.46 mM sodium citrate tribasic dihydrate was prepared and heated for 10 min at 60 °C using a water bath without stirring the solution. When the solution of gold reaches boiling point, the solution of sodium citrate tribasic dihydrate was added to the stirred gold solution. The resulting mixture was heated for an additional 10 min before cooling the solution to room temperature. The suspended Au NPs were isolated from the excess reagents through centrifugation at 9,500 rpm for 15 min. The supernatants were decanted and the Au NPs were re-dispersed in DI water with the assistance of a vortexer for 3 min.

4.3.7. Assembly of Au NPs onto the Silica Fe_3O_4 NPs

A solution of silica-coated iron oxide NPs (1 mg in 0.1 mL isopropanol), a solution of Au NPs (10 nM in 0.1 mL water), and a solution of $mPEG_{5000}$-SH (10 µL, 3% w/v in water) were combined in a 1.5 mL Eppendorf tube (VWR, 89000-028). This mixture was covered with aluminum foil and agitated on an orbital shaker at 250 rpm (VWR orbital shaker, VWR 57018-754) for 1 h at room temperature. After 1 h, the magnetic NPs were isolated from the excess reagents such as freely suspended Au NPs, through the use of external magnets. The isolated NPs were washed three times with isopropanol. During this purification process, the isolated NPs were suspended in 1 mL of isopropanol using

a vortexer (3 min) and a sonicator (3 min), and isolated from solution again using external magnets.

4.3.8. Characterization of the NPs

The Ellman's Test was used to quantify the surface coverage of thiol functional groups on silica-coated Fe_3O_4 NPs. A calibration curve was created using a series of standard solution containing 11-mercapto-1-undecanol (i.e., 0 mM to 0.50 mM 11-mercapto-1-undecanol) in isopropanol. The Ellman's reagent (50 µL, 4 mg/mL, suspended in 0.1 M sodium phosphate buffer), sodium phosphate buffer (2.5 mL, 0.1 M) and either the sample of interest or a standard solution of 11-mercapto-1-undecanol (250 µL, prepared in isopropanol) were mixed together. These solutions were mixed with the assistance of a vortexer for 15 min before obtaining an absorbance spectrum for each of the mixtures with an Agilent 8453 UV-Vis spectrometer. These assessments were performed at room temperature. The concentration of thiol groups present on the surfaces of the functionalized NPs were calculated from the calibration curve prepared from the series of standard solutions.

The calculated concentration of thiol groups determined from the Ellman's Test was used to estimate the coverage of thiols on the surfaces of the magnetic NPs. The total surface area of the silica-coated Fe_3O_4 NPs were estimated using the following steps: (i) the total number of NPs in a sample used for the Ellman's Test was calculated using the mass of the silica-coated Fe_3O_4 NPs, the density of these materials, and the average volume per NP; ; (ii) the density of the silica shell was estimated to be 1.90 g/cm^3; and the density of the Fe_3O_4 NPs was estimated to be 5.19 g/cm^3; [78] (iii) the average volume of the silica shell and the Fe_3O_4 core were calculated from TEM measurements; and (iv) assuming each particle was spherical, the total collective surface area of the silica-coated Fe_3O_4 NPs was estimated by multiplying the nominal surface area per NP (calculated using the diameter of NPs observed in TEM analyses) by the estimated total number of NPs in a sample.

X-ray photoelectron spectroscopy (XPS) measurements were conducted to verify the surface functionalization of the silica-coated Fe_3O_4 NPs. These measurements were acquired using a Kratos Analytical Axis ULTRA DLD system (Kratos Analytical, United Kingdom) with a monochromatic aluminum source (Al Kα at

1486.7 eV) operating at 150 W with a 90° takeoff angle. Survey spectra (0 to 1200 eV) were acquired using a pass energy of 160 eV, a dwell time of 100 ms, and 1 sweep. High-resolution spectra were obtained using a pass energy of 20 eV, a dwell time of 500 ms, and averaging the integrated signal from 10 sweeps.

Transmission electron microscopy (TEM) and energy dispersive X-ray spectroscopy (EDS) analyses were obtained using an FEI Tecnai Osiris operating at 200 kV (Thermo Fisher, USA). The number of Au NPs attached on the core-shell structure of the silica-coated Fe_3O_4 NPs was estimated from TEM analyses. For this estimation, the average of number of Au NPs was determined by counting the Au NPs in at least 5 different assemblies within each TEM sample. As the bright field TEM images provide the information from only one side of these assemblies, the number of Au NPS on the opposite side was estimated to be equivalent. The number of Au NPs in the projected images was doubled to achieve the reported value. Previous analyses have demonstrated this approach to be valid.

4.4. Results and Discussion

The Fe_3O_4 NPs used in these studies were similar to those used in Chapter 3. The average diameter of the Fe_3O_4 NPs was 250 nm and the silica coatings had an average thickness of 70 nm. Multi-functionalization of silica-coated Fe_3O_4 NPs were performed with different ratios of 11-mercapto-1-undecanol (thiol functionalized alcohol reagent) and 12-hydroxy-1-dodecanoic acid (carboxylic acid functionalized alcohol reagent).The silanol-alcohol condensation reaction was initiated with microwave radiation.

The Ellman's test was used to quantify the surface coverage of thiol groups on the surfaces of the functionalized NPs. Four different ratios of 11-mercapto-1-undecanol and 12-hydroxy-1-dodecanoic acid were tested in these studies. All of these conditions were analyzed in triplicate. As expected, the observed trend between the relative amounts of each reagent of thiol used during the silanol-alcohol condensation reaction and the surface coverage of thiol reagents was nearly linear (Fig. 4.1). The silica-coated Fe_3O_4 NPs that were functionalized with only 12-hydroxy-1-dodecanoic acid gave no response to the Ellman's reagent. When the silica-coated Fe_3O_4 NPs were functionalized with only the 11-mercapto-1-undecanol, the surface coverage was 2.4 ± 0.1 nm^2 per thiol or 0.42 thiols nm^{-2} on the surfaces of the magnetic NPs. When the carboxylic acid and thiol containing alcohol reagents were mixed equally, the thiol content on the surfaces of the NPs was 5.2 ± 0.9 nm^2 per thiol or 0.19 thiols nm^{-2}. This thiol surface coverage was approximately half of thiol surface coverage when only reacting with 11-merapto-1-undecanol. These values fit the expected trend for a well-mixed system with an equivalent number of each reagent attached to the surfaces of the NPs after the silanol-alcohol condensation reaction. As expected, an even higher ratio of 11-mercapto-1-undecanol to the 12-hydroxy-1-dodecanoic acid in the reaction mixture increased the number of thiols on the surfaces of the NPs (Fig. 4.1). The results from the use of a mixture of alcohol reagents and the trends therein suggest that these reagents equivalently react with the silanol groups on the silica. Adjusting the thiol content in the mixture of reagents correlates to the thiol content of the surfaces of the modified NPs. These results indicate that a one-pot approach to tuning the surface chemistry of the silica particles can be achieved through the silanol-alcohol condensation reaction. The Ellman's Test verified the presence and the amount of thiol groups on the surfaces, but

this technique could not provide information regarding the carboxylic acid groups on the surfaces of the NPs.

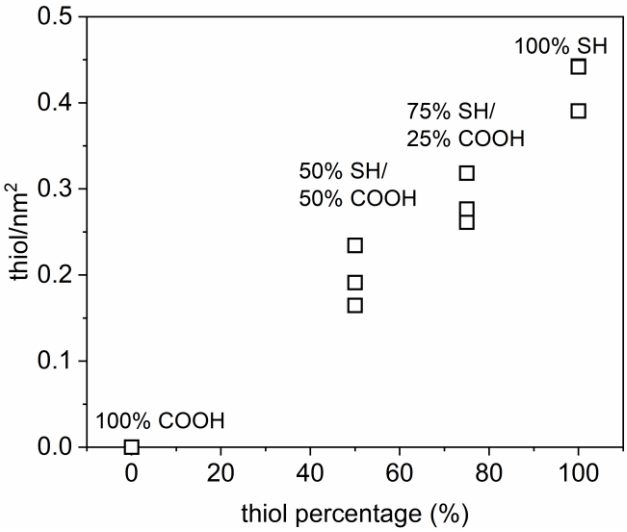

Figure 4.1 Comparison of the thiol content of the functionalized silica-coated Fe_3O_4 NPs prepared using the silanol-alcohol condensation reaction. These custom coatings were prepared by varying the ratio of 11-mercapto-1-undecanol (SH) and 12-hydroxy-1-dodecanoic acid (COOH) within the reaction mixture as indicated on the axes.

In Chapter 3, the silica-coated Fe_3O_4 NPs were also coated with carboxylic acid and diol containing alcohol reagents. These two different types of alcohol functionalization were verified in Chapter 3 with the formation of Au NP assemblies, but these were not confirmed therein using another analytical method. In this chapter, the carboxylic acid functionalization was further verified through X-ray photoelectron spectroscopy (XPS). An XPS survey scan indicated the composition of the surfaces of the silica-coated Fe_3O_4 NPs (Fig. 4.2). As the Fe_3O_4 NPs is covered by a 70-nm thick silica coating, the iron peaks were not present in this spectrum. This was due to the penetration depth of photoelectrons being 10 nm. This XPS spectrum indicates the presence of C, O, Si and possibly S species on the surfaces of the silica-coated Fe_3O_4 NPs. The Si_{2S} species overlaps with the S_{2p} species, which presents a challenge to quantitatively assess the presence of RSH species on these particles.[144] Higher resolution XPS analyses were, therefore, used to differentiate the carbon species bound to the surface of the NPs. The HR-XPS C_{1s} spectra contained distinctive peaks for both the carboxylic acid and thiol functional groups (Fig. 4.3 and 4.4). For the thiol-functionalized NPs, the C_{1s} peak at 286.2 eV signified the presence of a C-S bond associated with the thiol functional group and a peak at 284.8 eV confirmed the

presence of C-C bonds associated with the carbon backbone of the thiol species (Fig. 4.3). The prior art has reported the C_{1s} peak for the C-S bond to be located at 286 eV.[145–148] The C_{1s} peak position of C-C species is well understood to be located at 284 eV.[145–149] This result confirms that thiol groups were present on the surfaces of the NPs. For the carboxylic acid functionalized NPs, there was no distinct C-S peak present in the HR-XPS C_{1s} spectrum (Fig. 4.4).[94] Features associated with the carboxylic acid were, however, present in this HR-XPS spectrum. The broad shoulder at 286 eV signifies a bond between carbon and oxygen and the peak centred at 290.2 eV was associated with the C=O species.[94] The previous literature has indicated that the C-O bonds are located at 286 eV,[150] but that this peak is much broader than the C-S species. The corresponding carbon species for the carboxylic acid is the C=O bond at 289 eV.[94,96] These XPS analyses further confirmed the presence of the carboxylic acid groups on the surfaces of the NPs.

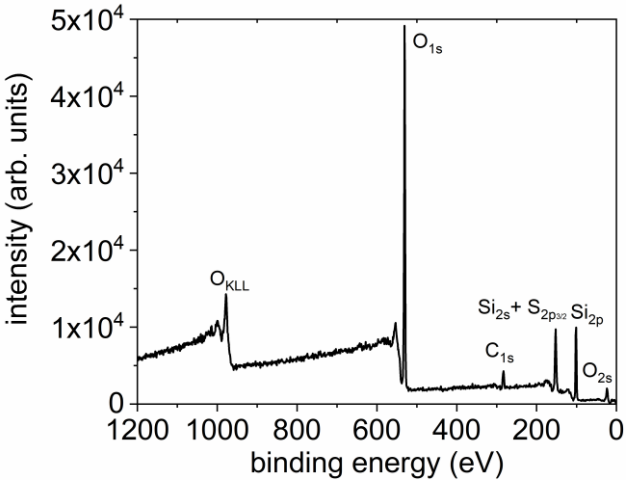

Figure 4.2 **Representative X-ray photoelectron spectroscopy survey scan of thiol funictonalized silica-coated Fe_3O_4 NPs. This functionalization was prepared by the microwave-assisted silanol-alcohol condensation reaction.**

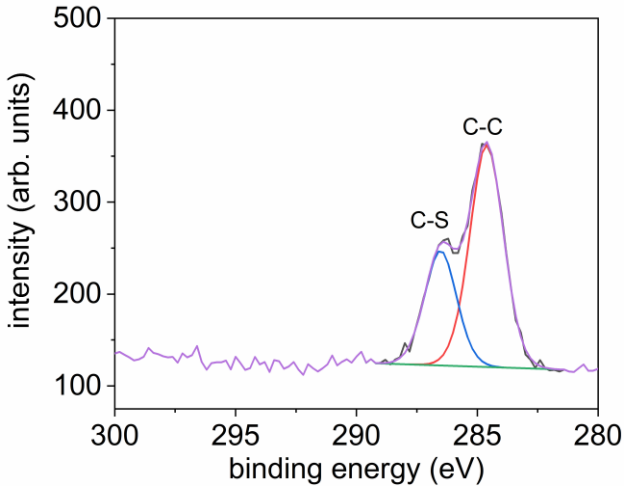

Figure 4.3 **Representative high resolution X-ray photoelectron spectroscopy (HR-XPS) analysis of thiol functionalized silica-coated Fe_3O_4 NPs. This functionalization was prepared by the microwave-assisted silanol-alcohol condensation reaction.**

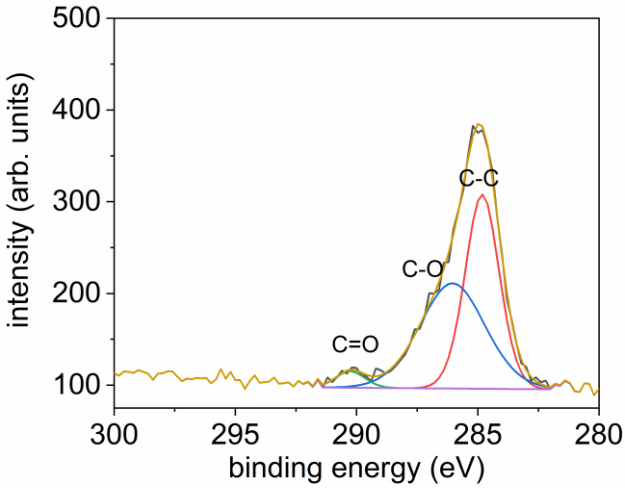

Figure 4.4 **Representative HR-XPS analysis of carboxylic acid functionalized silica-coated Fe_3O_4 NPs. This functionalization was prepared by the microwave-assisted silanol-alcohol condensation reaction.**

The surface chemistry of the functionalized NPs prepared from a 50/50 (mole ratio) mixture of 11-mercapto-1-undecanol and 12-hydroxy-1-dodecanoic acid were also analyzed by HR-XPS. This analysis sought to verify the presence of both the SH and COOH functional groups on the exterior surfaces of the NPs. The HR-XPS results for the C_{1s} species suggest that both the thiol and carboxylic acid groups were present on the NP's surfaces (Fig. 4.5). The peak at 286.2 eV indicates the presence of the C-S bond on the surfaces, which signifies the thiol groups were present on these surfaces. This position of the C-S bond was identical to that for the thiol only functionalized NPs, but the intensity of the peak was lower that of the thiol functionalized NPs relative to the C-C species (Fig. 4.3 and 4.5). The peak at 290.2 eV and a broad peak at 286 eV confirms the presence of the C=O and C-O bonds from the carboxylic acid groups, respectively. The positions of the peaks for these C=O and C-O species matched the peaks from the carboxylic acid functionalized NPs, but the intensity of these peaks also decreased relative to the C-C species in contrast to the coatings prepared from solely 12-hydroxy-1-dodecanoic acid (Fig. 4.4 and 4.5). If the ratio of these distinct peaks are compared relative to the C-C species, the mixed functionality on these NPs contained 45% of the C-S content relative to the thiol functionalized NPs, 43% of the C=O, and 45% of the C-O content compared to the carboxylic acid functionalized NPs. The C-S and C-O peak ratio might not be accurate as these two peaks have a significant overlap in the HR-XPS spectrum, but indicates the magnitude of the relative changes in this sample relative to the monofunctionalized NPs (Fig. 4.5). This decrease in relative peak intensity for either species could signify that there were less thiol and carboxylic groups present on the surfaces of multi-functionalized NPs. A similar result was also demonstrated in the Ellman's Test. As the thiol concentration in the reaction mixture decreased, the amount of thiol groups present on the surfaces of the NPs also decreased. The combination of results from the Ellman's Test and the XPS analyses confirmed that two different alcohol reagents can be simultaneously grafted onto the surfaces of the silica-coated Fe_3O_4 NPs. Previous literature has demonstrated thioesterification reactions, the reaction between a carboxylic acid group and a thiol group to form a thioester bond, which can be achieved under refluxing conditions in the presence of 4,4'-azopyridine as catalyst.[151] This reaction may happen under our reaction conditions even without the presence of this specific catalyst. The XPS analyses, however, could not provide information regarding whether this side reaction between 12-hydroxy-1-dodecanoic and 11-mercapto-1-undecanol took place. Further work is warranted here in the future.

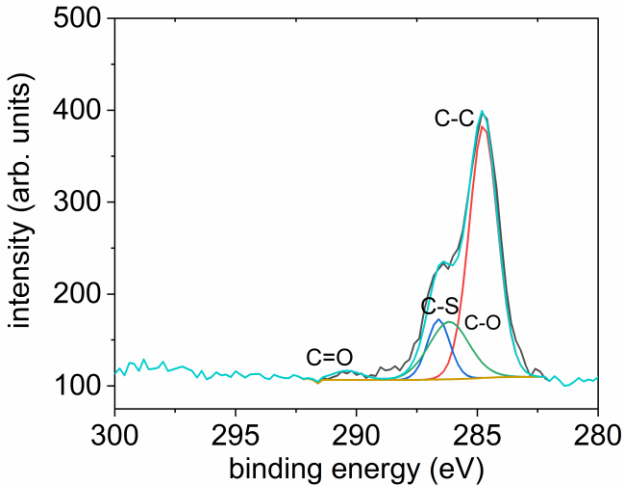

Figure 4.5 **Representative HR-XPS analysis of 50 SH/ 50 COOH (mole ratio) functionalized silica-coated Fe_3O_4 NPs. This functionalization was prepared by the microwave-assisted silanol-alcohol condensation reaction.**

The formation of Au NP assemblies on the core-shell structures was also used for visualizing the surface functionalization of the samples prepared by the microwave-assisted processes. A uniform distribution of Au NPs was observed over all of the surfaces of these magnetic NPs, similar to the results from an oil-bath heated sample (Fig. 4.6). The average number of Au NPs per assembly was determined by assessing the TEM data from 5 different core-shell particles. These assemblies contained 168 ± 35 Au NPs per magnetic core. The amount of Au NPs attached to the surfaces of the sample treated by the microwave-assisted reaction was lower than on the magnetic NPs functionalized with thiols using an oil-bath assisted reaction. This result was expected as the surface coverage of thiols for the microwave-assisted reactions at a reaction time of 2 h were slightly lower than the oil-bath heated sample reacted for 24 h.

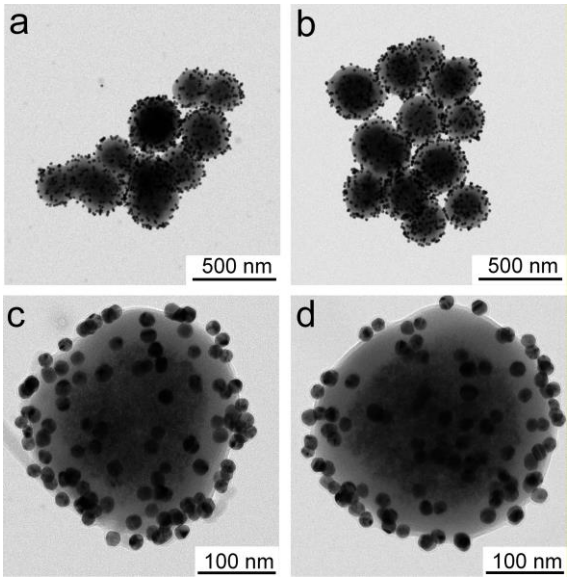

Figure 4.6 Representative TEM images of Au NPs assembled onto the thiol-functionalized core-shell particles. These thiol functionalized particles were prepared by a microwave-assisted silanol-alcohol condensation reaction.

The surface coverage of covalently linked species resulting from a microwave-assisted silanol-alcohol condensation reaction was not previously compared in a quantitative manner with the results of the same function achieved using a convective heating method. The functionalities prepared by either technique on silica substrates were previously compared by qualitative techniques, such as water contact angle measurements.[96] For the study outlined herein, a quantitative assessment was performed using silica-coated Fe_3O_4 NPs that were functionalized with a thiol containing alcohol reagent. These thiol functionalized NPs were prepared using three different conditions for the silanol-alcohol condensation reaction conditions: (i) convective heating at 80 ºC for 24 h; (ii) microwave-assisted heating at 80 ºC for 2 h; and (iii) room temperature for 24 h. The Ellman's Test was used to quantify and compare the surface coverage of thiols on the silica capped NPs as a result of each of these three thermal processes. Each of these conditions were performed in triplicate and the results compared to identify trends therein. Similar to Chapter 3, a calibration curve was prepared from a series of standard solutions containing 11-mercapto-1-undecanol at concentrations ranging from 0 to 0.50 mM.

The samples heated in an oil-bath at 80 °C for 24 h had the highest thiol coverage in comparison to the other conditions used to initiate the silanol-alcohol

reactions (Fig. 4.8). It was estimated that each thiol group occupies a surface area of 1.9 ± 0.1 nm^2, or 0.53 thiols nm^{-2} on these magnetic NPs. The sample prepared by microwave-assisted heating had the second highest thiol surface coverage with a thiol surface area of 2.4 ± 0.1 nm^2, or 0.42 thiols nm^{-2} on these magnetic NPs (Fig. 4.8). A statistical analysis of the results with the error assessed as three times the standard deviation from the calculated mean values suggests a significant overlap between these results. Although these results suggest a comparable surface coverage for these two methods, a larger sample size would be needed to determine an absolute quantification of thiols present on the surfaces of the NPs due to either set of process conditions. Even though the thiol surface coverage maybe lower for the microwave-assisted reaction than for the oil-bath heated samples, it only took 10% of the reaction time by microwave-assisted heating to achieve 78% of the surface coverage achieved from the oil-bath heating. The room temperature incubated sample had the lowest surface coverage of thiols. This condition had only a quarter of the surface coverage of the other two reaction conditions. As explained in Chapter 3, the coverage resulting from a room temperature reaction is likely due to the non-specific adsorption of 11-mercapto-1-undecanol onto the silica surfaces. A reaction time longer than 2 h using the microwave-assisted heating might be able to achieve a higher surface coverage of thiols in a fraction of the time required for the oil-bath heated reaction.

Nanoparticles coated with (3-mercaptopropyl)trimethyoxysilane (MPTMS) silane reagent were compared with the NPs prepared with a thiol functionalization through the silanol-alcohol condensation reaction. The MPTMS functionalized NPs had 10 times more thiol on their surfaces than the NPs functionalized via the silanol-alcohol condensation reaction. It was estimated that each thiol occupied an average surface area of 0.16 ± 0.02 nm^2, or there were 6.2 thiols nm^{-2} on the surfaces of the magnetic NPs. This coverage is higher than the reported value for silanol groups present on the surfaces of silica (4.6 silanols nm^{-2}).[126] The difference in these values might be due to the uneven coating of MPTMS on the NPs. The formation of uneven and multilayered surface coverages have been known to be a challenge that can result from surface functionalization with silane reagents.[89,91]

Energy dispersive X-ray spectroscopy (EDS) analyses were used to further analyze the elemental composition of thiol functionalized NPs. A comparison was made between the results achieved by the microwave-assisted silanol-alcohol condensation

reaction and the MPTMS coated silica-coated Fe_3O_4 NPs. For the sample prepared by the microwave-assisted reaction, the sulfur signal observed by EDS is relatively low (Fig. 4.9). The MPTMS coated Fe_3O_4 NPs had a higher sulfur signal in comparison. Similar results were seen in the Ellman's Test when comparing these same samples (Fig. 4.8). The thiol coverage as a result of the MPTMS species created islands on the surfaces of the NPs (Fig. 4.10). These results suggest the formation of a multilayer, prepared as a non-uniform coating of thiol species from the MPTMS reagent. In contrast, a lower surface coverage, but a more uniform coverage was achieved using the silanol-alcohol condensation reaction.

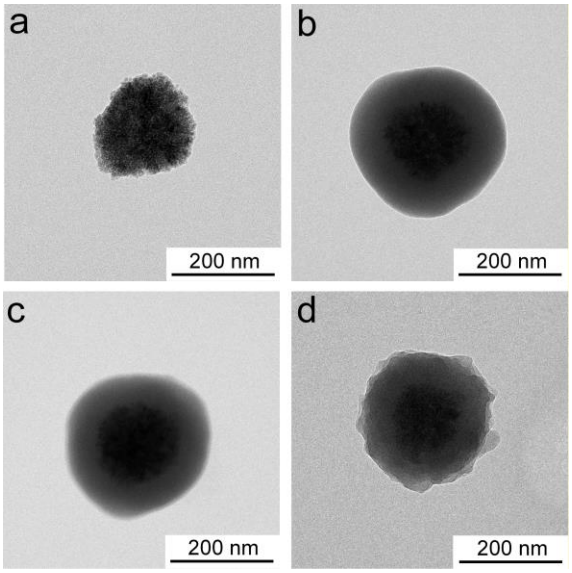

Figure 4.7 Representative TEM analyses of (a) the iron oxide nanoparticles, (b) the silica-coated Fe_3O_4 NPs, (c) the 11-mercapto-1-undecanol functionalized silica-coated Fe_3O_4 NPs, and (d) (3-mercaptopropyl)trimethoxysilane (MPTMS) functionalized silica-coated Fe_3O_4 NPs.

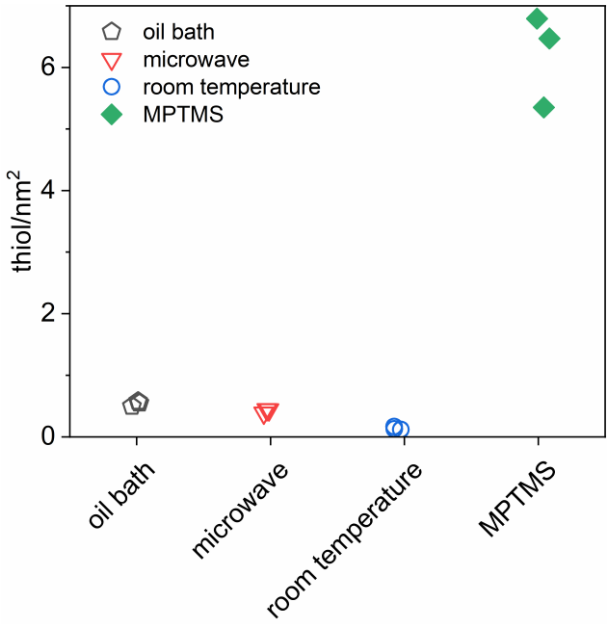

Figure 4.8 **Scatter plot of thiol coverage on the surfaces of the silica-coated Fe_3O_4 NPs. The oil bath-assisted, microwave-assisted, and room temperature reaction conditions were performed to assess their ability to induce a silanol-alcohol condensation reaction. The MPTMS functionalization was achieved using a silane reagent. These data were compiled from the results of the Ellman's Test performed on three replicate samples.**

Table 4.1 **Quantification of thiol coverage on the surfaces of the functionalized silica-coated Fe_3O_4 NPs correlated with reaction conditions.**

reaction condition	thiol coverage (thiols per nm^{-2})
silanol-alcohol condensation: oil bath assisted heating – 24 h @ 80 °C	0.53 ± 0.04
silanol-alcohol condensation: microwave-assisted heating – 2 h @ 80 °C	0.43 ± 0.03
silanol-alcohol condensation: no heating – 24 h @ RT	0.14 ± 0.03
silane reagent functionalization: (3-mercaptopropyl)trimethoxysilane (MPTMS) – 2 h @ 70 °C+ 24 h @ RT	6.1 ± 0.8

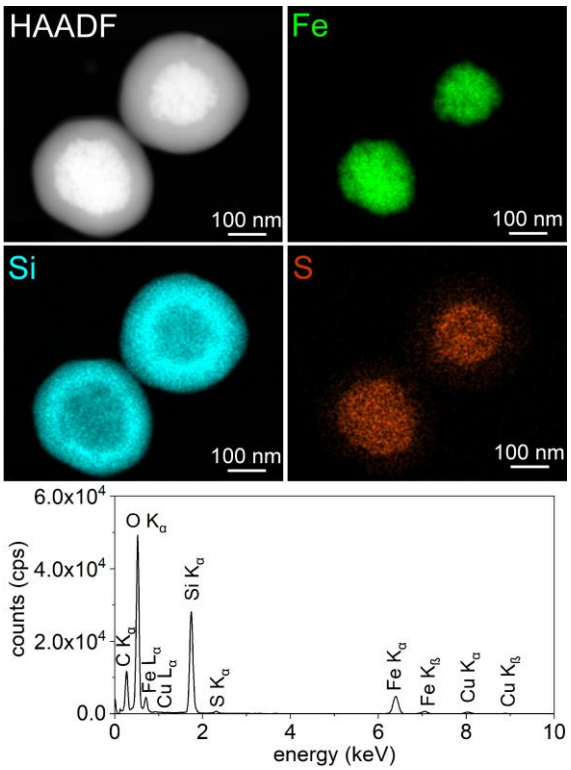

Figure 4.9 **Energy dispersive X-ray spectroscopy (EDS) analyses of the microwave radiation assisted thiol functionalization of silica-coated Fe_3O_4 NPs achieved by an silanol-alcohol condensation reaction. These images show a high-angle annular dark field (HAADF) image obtained by scanning TEM techniques, and EDS maps of Fe, Si, and S within this particle. A representative EDS spectrum is also included, depicting the composition of the particle along with contributions from the copper TEM grid.**

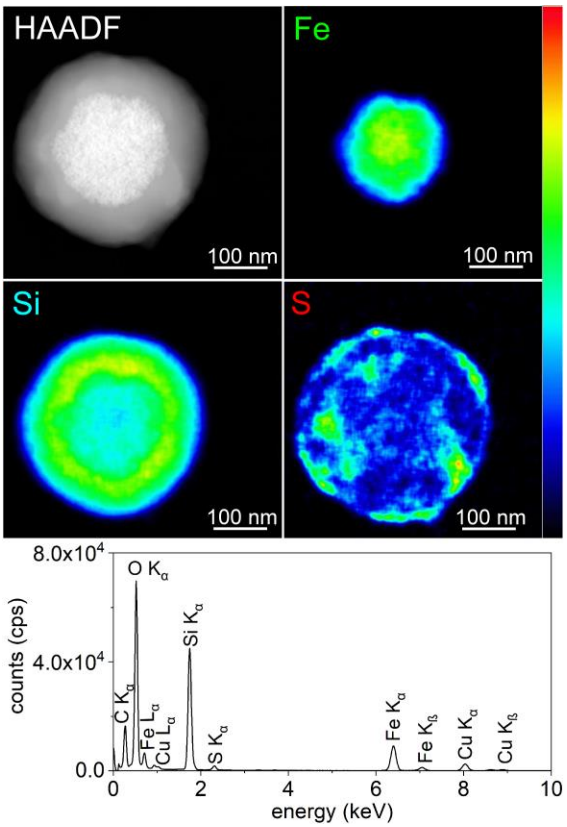

Figure 4.10 **The EDS analyses of the MPTMS functionalized Fe_3O_4 NPs. These images show the HAADF image obtained by scanning TEM techniques, and EDS maps of Fe, Si, and S within this particle. A representative EDS spectrum is also included, depicting the composition of the particle along with contributions from the copper TEM grid. The intensity scale for the EDS heat maps is provided on the right-hand side.**

4.5. Conclusion

We further demonstrated the ability to functionalize the surfaces of silica-coated Fe_3O_4 NPs through the silanol-alcohol condensation reaction. This reaction was tuned through adjusting the reaction conditions, as well as the alcohol reagents. The silanol-alcohol condensation reaction achieved by microwave-assisted heating was used to covalently link carboxylic acid and thiol terminated species to these NPs. An XPS analysis verified the presence of the carboxylic acids and thiols on the surfaces of the functionalized NPs. A mixed functionalization of the NPs with both carboxylic acid and thiol groups on their surfaces were also formed through the microwave-assisted silanol-alcohol condensation reaction. Composition of these surface coatings were confirmed through XPS measurement and the Ellman's Test. As a demonstration of the surface functionalization achieved using the microwave-assisted process, the assemblies with Au NPs were formed on the thiol functionalized silica-coated Fe_3O_4 NPs. These assemblies contained 168 ± 35 Au NPs per magnetic core. The silanol-alcohol condensation was further evaluated by assessing three different methods for initiating this reaction: (1) microwave-assisted heating; (2) oil-bath assisted heating; and (3) a room temperature reaction. These three conditions were compared for the thiol content on the surfaces of the resulting NPs. The Ellman's Test was used to quantify the thiol content on their surfaces. The oil-bath heating resulted in the highest thiol content on the surfaces of the NPs with 0.53 thiols per nm^2. The microwave-assisted heating resulted in the second highest thiol content with 0.42 thiols per nm^2. The microwave-assisted heating did, however, achieve 80% of the maximum loading achieved using the oil-bath assisted heating within one-tenth of the reaction time. Longer reaction times with the microwave-assisted process may achieve a higher thiol surface coverage, potentially surpassing that of the oil-bath assisted heating. With the possibility of attaching different functionalities to the surfaces of the NPs using a one-pot reaction, this process could be utilized for a range of different applications in future studies.

Chapter 5. Summary and Outlook

The research outlined in this thesis sought to modify the surfaces of silica-coated iron oxide nanoparticles (Fe_3O_4 NPs) through the silanol-alcohol condensation reaction. This method of covalently attaching alcohol reagents to the surfaces of silica has not been pursued before for silica-coated Fe_3O_4 NPs. Surface modifications of silica-coated Fe_3O_4 NPs have been achieved previously via the use of silane-based reagents or polymers. Challenges associated with these prior methods include a lack of covalent interactions with the polymers or instability of the silane-based reagents. There are several advantages of using alcohol-based reagents over these methods. Alcohol-based reagents have a relatively low toxicity and are mostly stable to moisture. The large diversity of functional groups available as alcohol reagents is one of the advantages. The silanol-alcohol condensation reaction is an alternative method for the functionalization of silica-coated Fe_3O_4 NPs.

Chapter 1 reviewed the methods to synthesize and modify the surfaces of Fe_3O_4 NPs with a focus on preparing and modifying silica coatings. The advantages and disadvantages, as well as the mechanisms involved in these processes, are discussed therein. Chapter 2 introduced the characterization tools and techniques used in the studies outlined in this thesis. These techniques include transmission electron microscopy, energy dispersive X-ray spectroscopy, X-ray photoelectron spectroscopy, and the Ellman's Test. The mechanism of each technique was discussed therein.

In Chapter 3, the silica-coated Fe_3O_4 NPs were functionalized with a thiol-terminated linear alcohol reagent, 11-mercapto-1-undecanol, using a convective assisted initiation of the condensation reaction. The thiol surface coverage was quantitatively analyzed via the Ellman's Test. It was estimated that each thiol group occupies a surface area of 1.9 ± 0.1 nm^2, or 0.53 thiols nm^{-2} on the magnetic NP. As a visualization of the successful surface modification, gold nanoparticles were attached to the thiol functionalized silica-coated Fe_3O_4 NPs. There were 320 ± 90 Au NPs per Fe_3O_4 core. In contrast, the native silica-coated iron oxide nanoparticles only had 6 ± 3 Au NPs per Fe_3O_4 core. This difference signifies that the thiol groups were indeed present on the surfaces of the NPs. This surface modification technique was extended to two different alcohol-based reagents, 12-hydroxy-1-dodecanoic acid, and 1,10-decanediol. Both of

these conditions had lower than 50 Au NPs per Fe_3O_4 NPs. The relative change in the number of gold nanoparticles assembled onto these functionalized nanoparticles suggested that these two alcohol reagents were present on the surfaces of these NPs.

In Chapter 4, a microwave-assisted silanol-alcohol condensation reaction was pursued in an attempt to further extend the methods used to prepare these functional coatings. Similar to Chapter 3, a thiol-terminated alcohol reagent was used as a standard for comparison of different methods for initiating the condensation reactions. The microwave-assisted heating was compared with the results achieved by convective heating using an oil-bath. The microwave-assisted sample had the 2.4 ± 0.1 nm^2, or 0.42 thiols nm^{-2} on these magnetic NPs, which was lower than the sample prepared using oil bath assisted heating. The carboxylic acid terminated surfaces were also prepared through a microwave-assisted silanol-alcohol condensation reaction. The surface functionalization was confirmed by X-ray photoelectron spectroscopy (XPS). The silanol-alcohol condensation reaction was also extended in Chapter 4 to preparing silica surfaces simultaneously functionalized with two different alcohol reagents. X-ray photoelectron spectroscopy and the Ellman's Test were used to verify the composition of these mixed surface modifications. The increase in thiol content was correlated to the increase of thiol alcohol reagents in the reaction mixture.

There were some additional challenges that still need to be overcome in the silanol-alcohol condensation reaction for the functionalization of Fe_3O_4 NPs:

1. Optimization of the assembly of Au NPs onto the core-shell structures: (i) optimization of the molecular weight of the PEG species could improve the achieve results; and (ii) the ratio of the PEG species to the Au NPs to the Fe_3O_4 NPs could also require further optimization.

2. Increasing the efficiency of silanol-alcohol condensation reaction: the Ellman's Test indicates that the silanol-alcohol condensation reaction reached approximately 10% of thiol surface coverage, which was lower than that achieved using the silane reagent (i.e., MPTMS).

3. Optimization of the synthesis and silica-coating of smaller Fe_3O_4 NPs: the size of the Fe_3O_4 NPs is sought to be around 15 nm for use in biomedical applications. Due to their high surface area to volume ratio these small nanoparticles tend to agglomerate

and form large clusters. When these large clusters are treated by the silica coating processes multiple nanoparticles would be coated within a single layer of silica. Further work is necessary to optimize this process.

4. Further verification of the surface functional groups should also be pursued: Different types of analytical methods should be pursued to verify the surface bound functional groups on the NPs. The results of techniques pursued in this study included: Fourier transform infrared spectroscopy (FT-IR, Appendix C), Raman spectroscopy (Appendix D), Ellman's Test (Chapters 3 and 4), thermogravimetric analysis (TGA, Appendix E), and X-ray photoelectron spectroscopy (Chapter 4). Some of these analyses were suitable, but some of them could not provide sufficient information regarding the surface functional groups. Different methods could be pursued in the future to study the surface modification in further detail.[91]

The silanol-alcohol condensation process, however, could be further optimized to increase the loading of the alcohol reagents covalently attached to the surfaces of the NPs. Since only 13% of silanol groups are functionalized with alcohol reagents, there is a lot of room for improvement. Reaction conditions could be optimized to increase the efficiency of the condensation reaction. There has been previous literature that suggests the silanol-alcohol condensation reaction performed under basic conditions could improve the efficiency of the reaction.[98] Solvents also have an effect on the efficiency of the condensation reaction. Three different polar aprotic solvents were tested previously. Propylene carbonate seemed to have the highest efficiency out of these solvents.[94] There might be a better solvent than propylene carbonate that could be used for the condensation reaction. Increasing the reaction temperature could also improve the condensation reaction. The water contact angle of silica substrates this functionalized by this method increased with increasing reaction temperature.[94] As shown previously, different reaction conditions such as the introduction of a base or further optimization of the reaction temperature could increase the loading of alcohol reagents on the surfaces. Further studies on optimizing the use of microwave radiation could also enable the condensation reaction to be completed possibly within a few hours. Longer reaction times could lead to an increase in alcohol reagents attached to the surfaces of the NPs. Previous work from our group shows that longer microwave reactions leads an increase in the amount of carboxylic acid groups on the silica-coated Au NPs.[152]

In this thesis, the assembly of Au NPs onto the functionalized silica-coated Fe_3O_4 NPs was performed to further verify the covalent attachment of the thiol species to the surfaces of silica-coated Fe_3O_4 NPs and the reactivity of the thiol through the ability to bind to the Au NPs. If the assembly steps are studied in further detail, the assembly of Au NPs of different sizes could be pursued to analyze the relationship between the number of Au NPs attached to the silica-coated Fe_3O_4 NPs and the size of the Au NPs.

The covalent attachment of alcohol reagents to silica surfaces can be applied to different applications by further tuning of the surface chemistry through the selection of additional reagents. Another aspect of future studies can be the pursuit of applications with the silica-coated Fe_3O_4 NPs, which could be enabled using the silanol-alcohol reagents. This thesis focused on the development of the silanol-alcohol condensation reaction to silica-coated Fe_3O_4 NPs, but the applications of these functionalized NPs were not pursued. The functionalized NPs can be applied to different fields by attaching other molecules to their surfaces, such as fluorescent tags for tracking the NPs or linkers to biomolecules for use in therapeutic purposes.

References

(1) Lakshmanan, R.; Gunaratna, R. Effective Water Content Reduction in Sewage Wastewater Sludge Using Magnetic Nanoparticles. *Bioresour. Technol.* **2014**, *153*, 333–339. https://doi.org/10.1016/j.biortech.2012.12.138.

(2) Aslani, F.; Bagheri, S.; Muhd Julkapli, N.; Juraimi, A. S.; Hashemi, F. S. G.; Baghdadi, A. Effects of Engineered Nanomaterials on Plants Growth: An Overview. *Sci. World J.* **2014**, *2014*. https://doi.org/10.1155/2014/641759.

(3) Dave, P. N.; Chopda, L. V. Application of Iron Oxide Nanomaterials for the Removal of Heavy Metals. *J. Nanotech.* 2014, pp 1–14. https://doi.org/10.1155/2014/398569.

(4) dos Santos Coelho, F.; Ardisson, J. D.; Moura, F. C. C.; Lago, R. M.; Murad, E.; Fabris, J. D. Potential Application of Highly Reactive Fe(0)/Fe_3O_4 Composites for the Reduction of Cr(VI) Environmental Contaminants. *Chemosphere* **2008**, *71* (1), 90–96. https://doi.org/https://doi.org/10.1016/j.chemosphere.2007.10.016.

(5) Azhar Uddin, M.; Tsuda, H.; Wu, S.; Sasaoka, E. Catalytic Decomposition of Biomass Tars with Iron Oxide Catalysts. *Fuel* **2008**, *87* (4), 451–459. https://doi.org/https://doi.org/10.1016/j.fuel.2007.06.021.

(6) Zhao, Z.; Zhou, Z.; Bao, J.; Wang, Z.; Hu, J.; Chi, X.; Ni, K.; Wang, R.; Chen, X.; Chen, Z.; et al. Octapod Iron Oxide Nanoparticles as High-Performance T2 Contrast Agents for Magnetic Resonance Imaging. *Nat. Commun.* **2013**, *4*, 2266.

(7) Shen, J.; Kim, H. C.; Su, H.; Wang, F.; Wolfram, J.; Kirui, D.; Mai, J.; Mu, C.; Ji, L. N.; Mao, Z. W.; et al. Cyclodextrin and Polyethylenimine Functionalized Mesoporous Silica Nanoparticles for Delivery of siRNA Cancer Therapeutics. *Theranostics* **2014**, *4* (5), 487–497. https://doi.org/10.7150/thno.8263.

(8) Espinosa, A.; Di Corato, R.; Kolosnjaj-Tabi, J.; Flaud, P.; Pellegrino, T.; Wilhelm, C. Duality of Iron Oxide Nanoparticles in Cancer Therapy: Amplification of Heating Efficiency by Magnetic Hyperthermia and Photothermal Bimodal Treatment. *ACS Nano* **2016**, *10* (2), 2436–2446. https://doi.org/10.1021/acsnano.5b07249.

(9) Huang, J.; Wang, L.; Lin, R.; Wang, A. Y.; Yang, L.; Kuang, M.; Qian, W.; Mao, H. Casein-Coated Iron Oxide Nanoparticles for High MRI Contrast Enhancement and Efficient Cell Targeting. *ACS Appl. Mater. Interfaces* **2013**, *5* (11), 4632–4639. https://doi.org/10.1021/am400713j.

(10) Ali, A. A. A.; Hsu, F. T.; Hsieh, C. L.; Shiau, C. Y.; Chiang, C. H.; Wei, Z. H.; Chen, C. Y.; Huang, H. S. Erlotinib-Conjugated Iron Oxide Nanoparticles as a Smart Cancer-Targeted Theranostic Probe for MRI. *Sci. Rep.* **2016**, *6* (April), 1–16. https://doi.org/10.1038/srep36650.

(11) Pavía-Sanders, A.; Zhang, S.; Flores, J. A.; Sanders, J. E.; Raymond, J. E.; Wooley, K. L. Robust Magnetic/polymer Hybrid Nanoparticles Designed for Crude Oil Entrapment and Recovery in Aqueous Environments. *ACS Nano* **2013**, *7* (9), 7552–7561. https://doi.org/10.1021/nn401541e.

(12) Deatsch, A. E.; Evans, B. A. Heating Efficiency in Magnetic Nanoparticle Hyperthermia. *J. Magn. Magn. Mater.* **2014**, *354*, 163–172. https://doi.org/https://doi.org/10.1016/j.jmmm.2013.11.006.

(13) de Montferrand, C.; Hu, L.; Milosevic, I.; Russier, V.; Bonnin, D.; Motte, L.; Brioude, A.; Lalatonne, Y. Iron Oxide Nanoparticles with Sizes, Shapes and Compositions Resulting in Different Magnetization Signatures as Potential Labels for Multiparametric Detection. *Acta Biomater.* **2013**, *9* (4), 6150–6157. https://doi.org/https://doi.org/10.1016/j.actbio.2012.11.025.

(14) Cornell, R. M.; Schwertmann, U. *The Iron Oxides : Structure, Properties, Reactions, Occurrences and Uses*, 2nd ed.; Wiley-VCH Verlag GmbH & Co. KGaA, 2003.

(15) Teja, A. S.; Koh, P. Y. Synthesis, Properties, and Applications of Magnetic Iron Oxide Nanoparticles. *Prog. Cryst. Growth Charact. Mater.* **2009**, *55* (1–2), 22–45. https://doi.org/10.1016/j.pcrysgrow.2008.08.003.

(16) Häfeli, U. O.; Pauer, G. J. In Vitro and in Vivo Toxicity of Magnetic Microspheres. *J. Magn. Magn. Mater.* **1999**, *194* (1), 76–82. https://doi.org/10.1016/S0304-8853(98)00560-5.

(17) Wu, W.; Wu, Z.; Yu, T.; Jiang, C.; Kim, W.-S. Recent Progress on Magnetic Iron Oxide Nanoparticles: Synthesis, Surface Functional Strategies and Biomedical Applications. *Sci. Technol. Adv. Mater.* **2015**, *16* (2), 23501. https://doi.org/10.1088/1468-6996/16/2/023501.

(18) Levy, D.; Giustetto, R.; Hoser, A. Structure of Magnetite (Fe_3O_4) above the Curie Temperature: A Cation Ordering Study. *Phys. Chem. Miner.* **2012**, *39* (2), 169–176. https://doi.org/10.1007/s00269-011-0472-x.

(19) Bengtson, A.; Morgan, D.; Becker, U. Spin State of Iron in Fe_3O_4 Magnetite and H-Fe_3O_4. *Phys. Rev. B - Condens. Matter Mater. Phys.* **2013**, *87* (15), 1–13. https://doi.org/10.1103/PhysRevB.87.155141.

(20) Li, Q.; Kartikowati, C. W.; Horie, S.; Ogi, T.; Iwaki, T.; Okuyama, K. Correlation between Particle Size/domain Structure and Magnetic Properties of Highly Crystalline Fe_3O_4 nanoparticles. *Sci. Rep.* **2017**, *7* (1), 1–4. https://doi.org/10.1038/s41598-017-09897-5.

(21) Gonzales-Weimuller, M.; Zeisberger, M.; Krishnan, K. M. Size-Dependant Heating Rates of Iron Oxide Nanoparticles for Magnetic Fluid Hyperthermia. *J. Magn. Magn. Mater.* **2009**, *321* (13), 1947–1950. https://doi.org/10.1016/j.jmmm.2008.12.017.

(22) Iida, H.; Takayanagi, K.; Nakanishi, T.; Osaka, T. Synthesis of Fe_3O_4 Nanoparticles with Various Sizes and Magnetic Properties by Controlled Hydrolysis. *J. Colloid Interface Sci.* **2007**, *314* (1), 274–280. https://doi.org/https://doi.org/10.1016/j.jcis.2007.05.047.

(23) Gilchrist, R. K.; Medal, R.; Shorey, W. D.; Hanselman, R. C.; Parrott, J. C.; Taylor, C. B. Selective Inductive Heating of Lymph Nodes. *Ann. Surg.* **1957**, *146* (4), 596–606. https://doi.org/10.1097/00000658-195710000-00007.

(24) Kumar, C. S. S. R.; Mohammad, F. Magnetic Nanomaterials for Hyperthermia-Based Therapy and Controlled Drug Delivery. *Adv. Drug Deliv. Rev.* **2011**, *63* (9), 789–808. https://doi.org/10.1016/J.ADDR.2011.03.008.

(25) Derfus, A. M.; Von Maltzahn, G.; Harris, T. J.; Duza, T.; Vecchio, K. S.; Ruoslahti, E.; Bhatia, S. N. Remotely Triggered Release from Magnetic Nanoparticles. *Adv. Mater.* **2007**, *19* (22), 3932–3936. https://doi.org/10.1002/adma.200700091.

(26) Brazel, C. S. Magnetothermally-Responsive Nanomaterials: Combining Magnetic Nanostructures and Thermally-Sensitive Polymers for Triggered Drug Release. *Pharm. Res.* **2009**, *26* (3), 644–656. https://doi.org/10.1007/s11095-008-9773-2.

(27) Alexiou, C.; Jurgons, R.; Schmid, R.; Hilpert, A.; Bergemann, C.; Parak, F.; Iro, H. In Vitro and in Vivo Investigations of Targeted Chemotherapy with Magnetic Nanoparticles. *J. Magn. Magn. Mater.* **2005**, *293* (1), 389–393. https://doi.org/10.1016/J.JMMM.2005.02.036.

(28) Fischer, B.; Huke, B.; Lücke, M.; Hempelmann, R. Brownian Relaxation of Magnetic Colloids. *J. Magn. Magn. Mater.* **2005**, *289*, 74–77. https://doi.org/https://doi.org/10.1016/j.jmmm.2004.11.021.

(29) Brown, W. F. Thermal Fluctuations of a Single-Domain Particle. *Phys. Rev.* **1963**, *130* (5), 1677–1686. https://doi.org/10.1103/PhysRev.130.1677.

(30) Shah, R. R.; Davis, T. P.; Glover, A. L.; Nikles, D. E.; Brazel, C. S. Impact of Magnetic Field Parameters and Iron Oxide Nanoparticle Properties on Heat Generation for Use in Magnetic Hyperthermia. *J. Magn. Magn. Mater.* **2015**, *387*, 96–106. https://doi.org/10.1016/J.JMMM.2015.03.085.

(31) Deatsch, A. E.; Evans, B. A. Heating Efficiency in Magnetic Nanoparticle Hyperthermia. *J. Magn. Magn. Mater.* **2014**, *354*, 163–172. https://doi.org/10.1016/J.JMMM.2013.11.006.

(32) Massart, R. Preparation of Aqueous Magnetic Liquids in Alkaline and Acidic Media. *IEEE Trans. Magn.* **1981**, *17* (2), 1247–1248. https://doi.org/10.1109/TMAG.1981.1061188.

(33) Sun, S.; Zeng, H.; Robinson, D. B.; Raoux, S.; Rice, P. M.; Wang, S. X.; Li, G. Monodisperse MFe_2O_4 (M = Fe, Co, Mn) Nanoparticles. *J. Am. Chem. Soc.* **2004**, *126* (1), 273–279. https://doi.org/10.1021/ja0380852.

(34) Ge, J.; Hu, Y.; Biasini, M.; Beyermann, W. P.; Yin, Y. Superparamagnetic Magnetite Colloidal Nanocrystal Clusters. *Angew. Chemie - Int. Ed.* **2007**, *46* (23), 4342–4345. https://doi.org/10.1002/anie.200700197.

(35) Sugimoto, T.; Matijević, E. Formation of Uniform Spherical Magnetite Particles by Crystallization from Ferrous Hydroxide Gels. *J. Colloid Interface Sci.* **1980**, *74* (1), 227–243. https://doi.org/10.1016/0021-9797(80)90187-3.

(36) *CRC Handbook of Chemistry and Physics.*; Cleveland, Ohio : CRC Press: Boca Raton, FL, 2019; Vol. 99th.

(37) Sugimoto, T. Formation of Monodispersed Nano- and Micro-Particles Controlled in Size, Shape, and Internal Structure. *Chem. Eng. Technol.* **2003**, *26* (3), 313–321. https://doi.org/10.1002/ceat.200390048.

(38) Blanco-Andujar, C.; Ortega, D.; Pankhurst, Q. A.; Thanh, N. T. K. Elucidating the Morphological and Structural Evolution of Iron Oxide Nanoparticles Formed by Sodium Carbonate in Aqueous Medium. *J. Mater. Chem.* **2012**, *22* (25), 12498–12506. https://doi.org/10.1039/c2jm31295f.

(39) Chastellain, M.; Petri, A.; Hofmann, H. Particle Size Investigations of a Multistep Synthesis of PVA Coated Superparamagnetic Nanoparticles. *J. Colloid Interface Sci.* **2004**, *278* (2), 353–360. https://doi.org/10.1016/j.jcis.2004.06.025.

(40) Pereira, C.; Pereira, A. M.; Fernandes, C.; Rocha, M.; Mendes, R.; Fernández-García, M. P.; Guedes, A.; Tavares, P. B.; Grenèche, J.-M.; Araújo, J. P.; et al. Superparamagnetic MFe_2O_4 (M = Fe, Co, Mn) Nanoparticles: Tuning the Particle Size and Magnetic Properties through a Novel One-Step Coprecipitation Route. *Chem. Mater.* **2012**, *24* (8), 1496–1504. https://doi.org/10.1021/cm300301c.

(41) Kim, D. K.; Zhang, Y.; Voit, W.; Rao, K. V.; Muhammed, M. Synthesis and Characterization of Surfactant-Coated Superparamagnetic Monodispersed Iron Oxide Nanoparticles. *J. Magn. Magn. Mater.* **2001**, *225* (1–2), 30–36. https://doi.org/10.1016/S0304-8853(00)01224-5.

(42) Kallumadil, M.; Tada, M.; Nakagawa, T.; Abe, M.; Southern, P.; Pankhurst, Q. A. Suitability of Commercial Colloids for Magnetic Hyperthermia. *J. Magn. Magn. Mater.* **2009**, *321* (10), 1509–1513. https://doi.org/10.1016/j.jmmm.2009.02.075.

(43) Laurent, S.; Forge, D.; Port, M.; Roch, A.; Robic, C.; Vander Elst, L.; Muller, R. N. Magnetic Iron Oxide Nanoparticles: Synthesis, Stabilization, Vectorization, Physicochemical Characterizations, and Biological Applications. *Chem. Rev.* **2008**, *108* (6), 2064–2110. https://doi.org/10.1021/cr068445e.

(44) Salavati-Niasari, M.; Mahmoudi, T.; Amiri, O. Easy Synthesis of Magnetite Nanocrystals via Coprecipitation Method. *J. Clust. Sci.* **2012**, *23* (2), 597–602. https://doi.org/10.1007/s10876-012-0451-5.

(45) Kim, S. B.; Cai, C.; Kim, J.; Sun, S.; Sweigart, D. A. Surface Modification of Fe_3O_4 and FePt Magnetic Nanoparticles with Organometallic Complexes. *Organometallics* **2009**, *28* (10), 5341–5348. https://doi.org/10.1021/om900375x.

(46) Hyeon, T.; Lee, S. S.; Park, J.; Chung, Y.; Na, H. Synthesis of Highly Crystalline and Monodisperse Maghemite Nanocrystallites without a Size-Selection Process. *J. Am. Chem. Soc.* **2001**, *123* (51), 12798–12801. https://doi.org/10.1021/ja016812s.

(47) Rockenberger, J.; Scher, E. C.; Alivisatos, A. P. A New Nonhydrolytic Single-Precursor Approach to Surfactant-Capped Nanocrystals of Transition Metal Oxides [15]. *J. Am. Chem. Soc.* **1999**, *121* (49), 11595–11596. https://doi.org/10.1021/ja993280v.

(48) Wu, W.; Xiao, X.; Zhang, S.; Zhou, J.; Fan, L.; Ren, F.; Jiang, C. Large-Scale and Controlled Synthesis of Iron Oxide Magnetic Short Nanotubes: Shape Evolution, Growth Mechanism, and Magnetic Properties. *J. Phys. Chem. C* **2010**, *114* (39), 16092–16103. https://doi.org/10.1021/jp1010154.

(49) Pinna, N.; Grancharov, S.; Beato, P.; Bonville, P.; Antonietti, M.; Niederberger, M. Magnetite Nanocrystals: Nonaqueous Synthesis, Characterization, and Solubility. *Chem. Mater.* **2005**, *17* (15), 3044–3049.

(50) Woo, K.; Hong, J.; Ahn, J. P. Synthesis and Surface Modification of Hydrophobic Magnetite to Processible Magnetite@silica-Propylamine. *J. Magn. Magn. Mater.* **2005**, *293* (1), 177–181. https://doi.org/10.1016/j.jmmm.2005.01.058.

(51) Li, S.; Zhang, T.; Tang, R.; Qiu, H.; Wang, C.; Zhou, Z. Solvothermal Synthesis and Characterization of Monodisperse Superparamagnetic Iron Oxide Nanoparticles. *J. Magn. Magn. Mater.* **2015**, *379*, 226–231. https://doi.org/10.1016/j.jmmm.2014.12.054.

(52) Wang, W.; Tang, B.; Ju, B.; Zhang, S. Size-Controlled Synthesis of Water-Dispersible Superparamagnetic Fe_3O_4 Nanoclusters and Their Magnetic Responsiveness. *RSC Adv.* **2015**, *5* (92), 75292–75299. https://doi.org/10.1039/c5ra14354c.

(53) Kozakova, Z.; Kuritka, I.; Kazantseva, N. E.; Babayan, V.; Pastorek, M.; Machovsky, M.; Bazant, P.; Saha, P. The Formation Mechanism of Iron Oxide Nanoparticles within the Microwave-Assisted Solvothermal Synthesis and Its Correlation with the Structural and Magnetic Properties. *Dalt. Trans.* **2015**, *44* (48), 21099–21108. https://doi.org/10.1039/c5dt03518j.

(54) Cheng, C.; Wen, Y.; Xu, X.; Gu, H. Tunable Synthesis of Carboxyl-Functionalized Magnetite Nanocrystal Clusters with Uniform Size. *J. Mater. Chem.* **2009**, *19* (46), 8782. https://doi.org/10.1039/b910832g.

(55) Smolensky, E. D.; Park, H. Y. E.; Berquó, T. S.; Pierre, V. C. Surface Functionalization of Magnetic Iron Oxide Nanoparticles for MRI Applications - Effect of Anchoring Group and Ligand Exchange Protocol. *Contrast Media Mol. Imaging* **2011**, *6* (4), 189–199. https://doi.org/10.1002/cmmi.417.

(56) Liang, S. Y.; Zhou, Q.; Wang, M.; Zhu, Y. H.; Wu, Q. Z.; Yang, X. L. Water-Soluble L-Cysteine-Coated FePt Nanoparticles as Dual MRI/CT Imaging Contrast Agent for Glioma. *Int. J. Nanomedicine* **2015**, *10*, 2325–2333. https://doi.org/10.2147/IJN.S75174.

(57) Aires, A.; Ocampo, S. M.; Simões, B. M.; Josefa Rodríguez, M.; Cadenas, J. F.; Couleaud, P.; Spence, K.; Latorre, A.; Miranda, R.; Somoza, Á.; et al. Multifunctionalized Iron Oxide Nanoparticles for Selective Drug Delivery to CD44-Positive Cancer Cells. *Nanotechnology* **2016**, *27* (6), 65103. https://doi.org/10.1088/0957-4484/27/6/065103.

(58) Laurent, S.; Dutz, S.; Häfeli, U. O.; Mahmoudi, M. Magnetic Fluid Hyperthermia : Focus on Superparamagnetic Iron Oxide Nanoparticles. *Adv. Colloid Interface Sci.* **2011**, *166* (1–2), 8–23. https://doi.org/10.1016/j.cis.2011.04.003.

(59) Suto, M.; Hirota, Y.; Mamiya, H.; Fujita, A.; Kasuya, R.; Tohji, K.; Jeyadevan, B. Heat Dissipation Mechanism of Magnetite Nanoparticles in Magnetic Fluid Hyperthermia. *J. Magn. Magn. Mater.* **2009**, *321* (10), 1493–1496. https://doi.org/10.1016/J.JMMM.2009.02.070.

(60) Revia, R. A.; Zhang, M. Magnetite Nanoparticles for Cancer Diagnosis, Treatment, and Treatment Monitoring: Recent Advances. *Mater. Today* **2016**, *19* (3), 157–168. https://doi.org/10.1016/j.mattod.2015.08.022.

(61) Hanessian, S.; Grzyb, J. A.; Cengelli, F.; Juillerat-Jeanneret, L. Synthesis of Chemically Functionalized Superparamagnetic Nanoparticles as Delivery Vectors for Chemotherapeutic Drugs. *Bioorganic Med. Chem.* **2008**, *16* (6), 2921–2931. https://doi.org/10.1016/j.bmc.2007.12.051.

(62) Wang, D.; Kou, R.; Choi, D.; Yang, Z.; Nie, Z.; Li, J.; Saraf, L. V; Hu, D.; Zhang, J.; Graff, G. L.; et al. Ternary Self-Assembly of Ordered Metal Oxide−Graphene Nanocomposites for Electrochemical Energy Storage. *ACS Nano* **2010**, *4* (3), 1587–1595. https://doi.org/10.1021/nn901819n.

(63) Mazloum, M.; Mehdi, A.; Alireza, M. High - Performance Electrochemical Sensor Based on Electrodeposited Iron Oxide Nanoparticle : Catecholamine as Analytical Probe. *J. Iran. Chem. Soc.* **2017**, *14* (8), 1659–1664. https://doi.org/10.1007/s13738-017-1106-0.

(64) Jun, Y. W.; Huh, Y. M.; Choi, J. S.; Lee, J. H.; Song, H. T.; Kim, S.; Yoon, S.; Kim, K. S.; Shin, J. S.; Suh, J. S.; et al. Nanoscale Size Effect of Magnetic Nanocrystals and Their Utilization for Cancer Diagnosis via Magnetic Resonance Imaging. *J. Am. Chem. Soc.* **2005**, *127* (16), 5732–5733. https://doi.org/10.1021/ja0422155.

(65) Guo, J.; Filpponen, I.; Johansson, L.-S.; Mohammadi, P.; Latikka, M.; Linder, M. B.; Ras, R. H. A.; Rojas, O. J. Complexes of Magnetic Nanoparticles with Cellulose Nanocrystals as Regenerable, Highly Efficient, and Selective Platform for Protein Separation. *Biomacromolecules* **2017**, *18* (3), 898–905. https://doi.org/10.1021/acs.biomac.6b01778.

(66) Lee, Y. T.; Woo, K. Preparation of Water-Dispersible and Biocompatible Iron Oxide Nanoparticles for MRI Agent. In *2006 IEEE Nanotechnology Materials and Devices Conference*; 2006; Vol. 1, pp 454–455. https://doi.org/10.1109/NMDC.2006.4388813.

(67) Illés, E.; Tombácz, E. The Effect of Humic Acid Adsorption on pH-Dependent Surface Charging and Aggregation of Magnetite Nanoparticles. *J. Colloid Interface Sci.* **2006**, *295* (1), 115–123. https://doi.org/10.1016/j.jcis.2005.08.003.

(68) Lalatonne, Y.; Richardi, J.; Pileni, M. P. Van Der Waals versus Dipolar Forces Controlling Mesoscopic Organizations of Magnetic Nanocrystals. *Nat. Mater.* **2004**, *3* (2), 121–125. https://doi.org/10.1038/nmat1054.

(69) Korpany, K. V; Majewski, D. D.; Chiu, C. T.; Cross, S. N.; Blum, A. S. Iron Oxide Surface Chemistry: Effect of Chemical Structure on Binding in Benzoic Acid and Catechol Derivatives. *Langmuir* **2017**, *33* (12), 3000–3013. https://doi.org/10.1021/acs.langmuir.6b03491.

(70) Bautista, M. C.; Bomati-Miguel, O.; Zhao, X.; Morales, M. P.; González-Carreño, T.; Alejo, R. P. de; Ruiz-Cabello, J.; Veintemillas-Verdaguer, S. Comparative Study of Ferrofluids Based on Dextran-Coated Iron Oxide and Metal Nanoparticles for Contrast Agents in Magnetic Resonance Imaging. *Nanotechnology* **2004**, *15* (4), S154–S159. https://doi.org/10.1088/0957-4484/15/4/008.

(71) Wahajuddin; Arora, S. Superparamagnetic Iron Oxide Nanoparticles: Magnetic Nanoplatforms as Drug Carriers. *Int. J. Nanomedicine* **2012**, *7*, 3445–3471. https://doi.org/10.2147/IJN.S30320.

(72) Zhou, Y. T.; Branford-White, C.; Nie, H. L.; Zhu, L. M. Adsorption Mechanism of Cu2+ from Aqueous Solution by Chitosan-Coated Magnetic Nanoparticles Modified with ??-Ketoglutaric Acid. *Colloids Surfaces B Biointerfaces* **2009**, *74* (1), 244–252. https://doi.org/10.1016/j.colsurfb.2009.07.026.

(73) Qiao, T.; Wu, Y.; Jin, J.; Gao, W.; Xie, Q.; Wang, S.; Zhang, Y.; Deng, H. Conjugation of Catecholamines on Magnetic Nanoparticles Coated with Sulfonated Chitosan. *Colloids Surfaces A Physicochem. Eng. Asp.* **2011**, *380* (1–3), 169–174. https://doi.org/10.1016/j.colsurfa.2011.02.038.

(74) McCarthy, J. R.; Weissleder, R. Multifunctional Magnetic Nanoparticles for Targeted Imaging and Therapy. *Adv. Drug Deliv. Rev.* **2008**, *60* (11), 1241–1251. https://doi.org/10.1016/j.addr.2008.03.014.

(75) Sodipo, B. K.; Aziz, A. A. Recent Advances in Synthesis and Surface Modification of Superparamagnetic Iron Oxide Nanoparticles with Silica. *J. Magn. Magn. Mater.* **2016**, *416*, 275–291. https://doi.org/10.1016/j.jmmm.2016.05.019.

(76) Wong, Y. J.; Zhu, L.; Teo, W. S.; Tan, Y. W.; Yang, Y.; Wang, C.; Chen, H. Revisiting the Stober Method: Inhomogeneity in Silica Shells. *J. Am. Chem. Soc.* **2011**, *133* (30), 11422–11425. https://doi.org/10.1021/ja203316q.

(77) Stöber, W.; Fink, A.; Bohn, E. Controlled Growth of Monodisperse Silica Spheres in the Micron Size Range. *J. Colloid Interface Sci.* **1968**, *26* (1), 62–69. https://doi.org/10.1016/0021-9797(68)90272-5.

(78) van Blaaderen, A.; Vrij, A. Synthesis and Characterization of Monodisperse Colloidal Organo-Silica Spheres. *J. Colloid Interface Sci.* **1993**, *156* (1), 1–18. https://doi.org/https://doi.org/10.1006/jcis.1993.1073.

(79) Buckley, A. M.; Greenblatt, M. The Sol-Gel Preparation of Silica Gels. *J. Chem. Educ.* **1994**, *71* (7), 599. https://doi.org/10.1021/ed071p599.

(80) Zhang, S.; Zhang, Y.; Liu, J.; Xu, Q.; Xiao, H.; Wang, X.; Xu, H.; Zhou, J. Thiol Modified Fe_3O_4@SiO_2 as a Robust, High Effective, and Recycling Magnetic Sorbent for Mercury Removal. *Chem. Eng. J.* **2013**, *226*, 30–38. https://doi.org/https://doi.org/10.1016/j.cej.2013.04.060.

(81) Ghasemzadeh, M. A.; Abdollahi-basir, M. H. Green Chemistry Letters and Reviews Fe_3O_4 @ SiO_2 – NH_2 Core-Shell Nanocomposite as an Efficient and Green Catalyst for the Multi- Component Synthesis of Highly Substituted Chromeno [2,3-B] Pyridines in Aqueous Ethanol Media. *Green Chem. Lett. Rev.* **2015**, *8* (3–4), 40–49.

(82) He, Y. P.; Wang, S. Q.; Li, C. R.; Miao, Y. M.; Wu, Z. Y.; Zou, B. S. Synthesis and Characterization of Functionalized Silica-Coated Fe_3O_4 Superparamagnetic Nanocrystals for Biological Applications. *J. Phys. D. Appl. Phys.* **2005**, *38* (9), 1342–1350. https://doi.org/10.1088/0022-3727/38/9/003.

(83) Liu, Y.; Li, Y.; Li, X. M.; He, T. Kinetics of (3-Aminopropyl)triethoxylsilane (Aptes) Silanization of Superparamagnetic Iron Oxide Nanoparticles. *Langmuir* **2013**, *29* (49), 15275–15282. https://doi.org/10.1021/la403269u.

(84) Lei, L.; Liu, X.; Li, Y.; Cui, Y.; Yang, Y.; Qin, G. Study on Synthesis of poly(GMA)-Grafted Fe_3O_4/ SiOX Magnetic Nanoparticles Using Atom Transfer Radical Polymerization and Their Application for Lipase Immobilization. *Mater. Chem. Phys.* **2011**, *125* (3), 866–871. https://doi.org/10.1016/j.matchemphys.2010.09.031.

(85) Galli, M.; Guerrini, A.; Cauteruccio, S.; Thakare, P.; Dova, D.; Orsini, F.; Arosio, P.; Carrara, C.; Sangregorio, C.; Lascialfari, A.; et al. Superparamagnetic Iron Oxide Nanoparticles Functionalized by Peptide Nucleic Acids. *RSC Adv.* **2017**, *7* (25), 15500–15512. https://doi.org/10.1039/c7ra00519a.

(86) Ratner, B. D.; Hoffman, A. S. Physicochemical Surface Modification of Materials Used in Medicine. In *Biomaterials Science: An Introduction to Materials in Medicine*; Ratner, B. D., Hoffman, A. S., Schoen, F. J., Lemons, J. E. B. T.-B. S. (Third E., Eds.; Academic Press, 2013; pp 259–276. https://doi.org/https://doi.org/10.1016/B978-0-08-087780-8.00027-9.

(87) McGovern, M. E.; Kallury, K. M. R.; Thompson, M. Role of Solvent on the Silanization of Glass with Octadecyltrichlorosilane. *Langmuir* **1994**, *10* (10), 3607–3614. https://doi.org/10.1021/la00022a038.

(88) Nie, H. Y.; Walzak, M. J.; McIntyre, N. S. Bilayer and Odd-Numbered Multilayers of Octadecylphosphonic Acid Formed on a Si Substrate Studied by Atomic Force Microscopy. *Langmuir* **2002**, *18* (7), 2955–2958. https://doi.org/10.1021/la0116847.

(89) Yoshida, W.; Castro, R. P.; Jou, J.-D.; Cohen, Y. Multilayer Alkoxysilane Silylation of Oxide Surfaces. *Langmuir* **2001**, *17* (19), 5882–5888. https://doi.org/10.1021/la001780s.

(90) Soto-Cantu, E.; Cueto, R.; Koch, J.; Russo, P. S. Synthesis and Rapid Characterization of Amine-Functionalized Silica. *Langmuir* **2012**, *28* (13), 5562–5569. https://doi.org/10.1021/la204981b.

(91) Kunc, F.; Balhara, V.; Brinkmann, A.; Sun, Y.; Leek, D. M.; Johnston, L. J. Quantification and Stability Determination of Surface Amine Groups on Silica Nanoparticles Using Solution NMR. *Anal. Chem.* **2018**, *90* (22), 13322–13330. https://doi.org/10.1021/acs.analchem.8b02803.

(92) Dion, M.; Rapp, M.; Rorrer, N.; Shin, D. H.; Martin, S. M.; Ducker, W. A. The Formation of Hydrophobic Films on Silica with Alcohols. *Colloids Surfaces A Physicochem. Eng. Asp.* **2010**, *362* (1–3), 65–70. https://doi.org/10.1016/j.colsurfa.2010.03.044.

(93) Sprung, M. M.; Guenther, F. O. The Reaction of Some Silanols and Siloxanes with N-Octyl Alcohol. *J. Org. Chem.* **1961**, *26* (2), 552–557. https://doi.org/10.1021/jo01061a064.

(94) Lee, A. W. H.; Gates, B. D. Covalent Surface Modification of Silicon Oxides with Alcohols in Polar Aprotic Solvents. *Langmuir* **2017**, *33* (35), 8707–8715. https://doi.org/10.1021/acs.langmuir.7b00820.

(95) Hacker, C. A.; Anderson, K. A.; Richter, L. J.; Richter, C. A. Comparison of Si−O−C Interfacial Bonding of Alcohols and Aldehydes on Si(111) Formed from Dilute Solution with Ultraviolet Irradiation. *Langmuir* **2005**, *21* (3), 882–889. https://doi.org/10.1021/la048841x.

(96) Lee, A. W. H.; Gates, B. D. Rapid Covalent Modification of Silicon Oxide Surfaces through Microwave-Assisted Reactions with Alcohols. *Langmuir* **2016**, *32* (29), 7284–7293. https://doi.org/10.1021/acs.langmuir.6b00662.

(97) Lee, A. W. H.; Gates, B. D. Tuning Oleophobicity of Silicon Oxide Surfaces with Mixed Monolayers of Aliphatic and Fluorinated Alcohols. *Langmuir* **2016**, *32* (49), 13030–13039. https://doi.org/10.1021/acs.langmuir.6b03415.

(98) Raymon, A.; Angell, C. L. Study of Alcohol-Silica Surface Reactions. *J. Phys. Chem.* **1973**, *77* (26), 3048–3052.

(99) Gude, V. G.; Patil, P.; Martinez-Guerra, E.; Deng, S.; Nirmalakhandan, N. Microwave Energy Potential for Biodiesel Production. *Sustain. Chem. Process.* **2013**, *1* (1), 5. https://doi.org/10.1186/2043-7129-1-5.

(100) Egerton, R. F. *Physical Principles of Electron Microscopy: An Introduction to TEM, SEM, and AEM*; Boston, MA: Springer US: Boston, MA, 2005. https://doi.org/10.1007/b136495.

(101) Williams, D. B.; Carter, C. B. *Transmission Electron Microscopy: A Textbook for Materials Science*, 2nd ed.; Boston, MA: Springer US: Boston, MA, 2009. https://doi.org/10.1007/978-0-387-76501-3.

(102) Thomas, J.; Gemming, T. *Analytical Transmission Electron Microscopy: An Introduction for Operators*; Dordrecht: Springer Netherlands: Dordrecht, 2014. https://doi.org/10.1007/978-94-017-8601-0.

(103) Steinhardt, R. G.; Serfass, E. J. X-Ray Photoelectron Spectrometer for Chemical Analysis. *Anal. Chem.* **1951**, *23* (11), 1585–1590. https://doi.org/10.1021/ac60059a019.

(104) Hofmann, S. *Auger- and X-Ray Photoelectron Spectroscopy in Materials Science: A User-Oriented Guide*; Springer Berlin Heidelberg, Berlin, Heidelberg: Berlin, Heidelberg, 2013. https://doi.org/10.1007/978-3-642-27381-0.

(105) Chakraborty, B. R.; Hofmann, S. Ion Bombardment Induced Silicide Formation during Sputter Depth Profiling of Ta/Si Multilayer Thin Film Structure as Studied by X-Ray Photoelectron Spectroscopy and Auger Electron Spectroscopy. *Thin Solid Films* **1991**, *204* (1), 163–174. https://doi.org/https://doi.org/10.1016/0040-6090(91)90502-O.

(106) Ellman, G. L. Tissue Sulfhydryl Groups. *Arch. Biochem. Biophys.* **1959**, *82* (1), 70–77. https://doi.org/10.1016/0003-9861(59)90090-6.

(107) Hinterwirth, H.; Kappel, S.; Waitz, T.; Prohaska, T.; Lindner, W.; Lämmerhofer, M. Quantifying Thiol Ligand Density of Self-Assembled Monolayers on Gold Nanoparticles by Inductively Coupled Plasma-Mass Spectrometry. *ACS Nano* **2013**, *7* (2), 1129–1136. https://doi.org/10.1021/nn306024a.

(108) Hostetler, M. J.; Wingate, J. E.; Zhong, C.-J.; Harris, J. E.; Vachet, R. W.; Clark, M. R.; Londono, J. D.; Green, S. J.; Stokes, J. J.; Wignall, G. D.; et al. Alkanethiolate Gold Cluster Molecules with Core Diameters from 1.5 to 5.2 Nm: Core and Monolayer Properties as a Function of Core Size. *Langmuir* **1998**, *14* (1), 17–30. https://doi.org/10.1021/la970588w.

(109) Matsuura, K.; Murai, K.; Fukano, Y.; Takashina, H. Simultaneous Determination of Tiopronin and Its Metabolites in Rat Blood by LC-ESI-MS-MS Using Methyl Acrylate for Stabilization of Thiol Group. *J. Pharm. Biomed. Anal.* **2000**, *22* (1), 101–109. https://doi.org/https://doi.org/10.1016/S0731-7085(99)00271-X.

(110) Winther, J. R.; Thorpe, C. Quantification of Thiols and Disulfides. *Biochim. Biophys. Acta - Gen. Subj.* **2014**, *1840* (2), 838–846. https://doi.org/10.1016/j.bbagen.2013.03.031.

(111) Moser, M.; Behnke, T.; Hamers-Allin, C.; Klein-Hartwig, K.; Falkenhagen, J.; Resch-Genger, U. Quantification of PEG-Maleimide Ligands and Coupling Efficiencies on Nanoparticles with Ellman's Reagent. *Anal. Chem.* **2015**, *87* (18), 9376–9383. https://doi.org/10.1021/acs.analchem.5b02173.

(112) Habeeb, A. F. S. A. [37] Reaction of Protein Sulfhydryl Groups with Ellman's Reagent. In *Enzyme Structure, Part B*; Methods in Enzymology; Academic Press, 1972; Vol. 25, pp 457–464. https://doi.org/https://doi.org/10.1016/S0076-6879(72)25041-8.

(113) Moser, M.; Schneider, R.; Behnke, T.; Schneider, T.; Falkenhagen, J.; Resch-Genger, U. Ellman's and Aldrithiol Assay as Versatile and Complementary Tools for the Quantification of Thiol Groups and Ligands on Nanomaterials. *Anal. Chem.* **2016**, *88* (17), 8624–8631. https://doi.org/10.1021/acs.analchem.6b01798.

(114) Kang, H. J. H.; Ali, R. F.; Paul, M. T. Y.; Radford, M. J.; Andreu, I.; Lee, A. W. H.; Gates, B. D. Tunable Functionalization of Silica Coated Iron Oxide Nanoparticles Achieved through a Silanol–alcohol Condensation Reaction. *Chem. Commun.* **2019**, *55* (70), 10452–10455. https://doi.org/10.1039/C9CC03969D.

(115) Peng, Y. K.; Lui, C. N. P.; Lin, T. H.; Chang, C.; Chou, P. T.; Yung, K. K. L.; Tsang, S. C. E. Multifunctional Silica-Coated Iron Oxide Nanoparticles: A Facile Four-in-One System for in Situ Study of Neural Stem Cell Harvesting. *Faraday Discuss.* **2014**, *175*, 13–26. https://doi.org/10.1039/c4fd00132j.

(116) Khandhar, A. P.; Keselman, P.; Kemp, S. J.; Ferguson, R. M.; Goodwill, P. W.; Conolly, S. M.; Krishnan, K. M. Evaluation of PEG-Coated Iron Oxide Nanoparticles as Blood Pool Tracers for Preclinical Magnetic Particle Imaging. *Nanoscale* **2017**, 1299–1306. https://doi.org/10.1039/C6NR08468K.

(117) Porter, C. J. H.; Moghimi, S. M.; Illum, L.; Davis, S. S. The Polyoxyethylene/polyoxypropylene Block Co-Polymer Poloxamer-407 Selectively Redirects Intravenously Injected Microspheres to Sinusoidal Endothelial Cells of Rabbit Bone Marrow. *FEBS Lett.* **1992**, *305* (1), 62–66. https://doi.org/10.1016/0014-5793(92)80655-Z.

(118) Suk, J.; Yeon, J.; Hui, S.; Yoon, I.; Jung, C.; Choo, J. Annals of Nuclear Energy Effect of Surface Modification of Silica Nanoparticles by Silane Coupling Agent on Decontamination Foam Stability. *Ann. Nucl. Energy* **2018**, *114*, 11–18. https://doi.org/10.1016/j.anucene.2017.12.007.

(119) Bracho, D.; Dougnac, V. N.; Palza, H. Functionalization of Silica Nanoparticles for Polypropylene Nanocomposite Applications. *J. Nanomater.* **2012**, *2012*, 1–8. https://doi.org/10.1155/2012/263915.

(120) Strong, L.; Whitesides, G. M. Structures of Self-Assembled Monolayer Films of Organosulfur Compounds Adsorbed on Gold Single Crystals: Electron Diffraction Studies. *Langmuir* **1988**, *4* (3), 546–558. https://doi.org/10.1021/la00081a009.

(121) Dubois, L. H.; Zegarski, B. R.; Nuzzo, R. G. Molecular Ordering of Organosulfur Compounds on Au(111) and Au(100): Adsorption from Solution and in Ultrahigh Vacuum. *J. Chem. Phys.* **1993**, *98* (1), 678–688. https://doi.org/10.1063/1.464613.

(122) Gardner, K. L.; Tait, J. G.; Merckx, T.; Qiu, W.; Paetzold, U. W.; Kootstra, L.; Jaysankar, M.; Gehlhaar, R.; Cheyns, D.; Heremans, P.; et al. Nonhazardous Solvent Systems for Processing Perovskite Photovoltaics. *Adv. Energy Mater.* **2016**, *6* (14), 1600386. https://doi.org/10.1002/aenm.201600386.

(123) Kimling, J.; Maier, M.; Okenve, B.; Kotaidis, V.; Ballot, H.; Plech, A. Turkevich Method for Gold Nanoparticle Synthesis Revisited. *J. Phys. Chem. B* **2006**, *110* (32), 15700–15707. https://doi.org/10.1021/jp061667w.

(124) Liu, X.; Atwater, M.; Wang, J.; Huo, Q. Extinction Coefficient of Gold Nanoparticles with Different Sizes and Different Capping Ligands. *Colloids Surfaces B Biointerfaces* **2007**, *58* (1), 3–7. https://doi.org/https://doi.org/10.1016/j.colsurfb.2006.08.005.

(125) Riddles, P. W.; Blakeley, R. L.; Zerner, B. [8] Reassessment of Ellman's Reagent. *Methods Enzymol.* **1983**, *91*, 49–60. https://doi.org/10.1016/S0076-6879(83)91010-8.

(126) Zhuravlev, L. T. The Surface Chemistry of Amorphous Silica. Zhuravlev Model. *Colloids Surfaces A Physicochem. Eng. Asp.* **2000**, *173* (1–3), 1–38. https://doi.org/10.1016/S0927-7757(00)00556-2.

(127) Aherne, D.; Rao, S. N.; Fitzmaurice, D. Programming a Gold Nanocrystal to Recognize and Selectively Bind a Molecular Substrate in Solution. *J. Phys. Chem. B* **1999**, *103* (11), 1821–1825. https://doi.org/10.1021/jp9832950.

(128) Kirihara, M.; Asai, Y.; Ogawa, S.; Noguchi, T.; Hatano, A.; Hirai, Y. A Mild and Environmentally Benign Oxidation of Thiols to Disulfides. *Synthesis (Stuttg).* **2007**, No. 21, 3286–3289. https://doi.org/10.1055/s-2007-990800.

(129) Wang, Y.; Chen, G.; Yang, M.; Silber, G.; Xing, S.; Tan, L. H.; Wang, F.; Feng, Y.; Liu, X.; Li, S.; et al. A Systems Approach towards the Stoichiometry-Controlled Hetero-Assembly of Nanoparticles. *Nat. Commun.* **2010**, *1*, 87.

(130) Chen, T.; Yang, M.; Wang, X.; Tan, L. H.; Chen, H. Controlled Assembly of Eccentrically Encapsulated Gold Nanoparticles. *J. Am. Chem. Soc.* **2008**, *130* (36), 11858–11859. https://doi.org/10.1021/ja8040288.

(131) Lei, L.; Liu, X.; Li, Y.; Cui, Y.; Yang, Y.; Qin, G. Study on Synthesis of poly(GMA)-Grafted Fe_3O_4/ SiOX Magnetic Nanoparticles Using Atom Transfer Radical Polymerization and Their Application for Lipase Immobilization. *Mater. Chem. Phys.* **2011**, *125* (3), 866–871. https://doi.org/10.1016/j.matchemphys.2010.09.031.

(132) Foglia, S.; Ledda, M.; Fioretti, D.; Iucci, G.; Papi, M.; Capellini, G.; Lolli, M. G.; Grimaldi, S.; Rinaldi, M.; Lisi, A. In Vitro Biocompatibility Study of Sub-5 Nm Silica-Coated Magnetic Iron Oxide Fluorescent Nanoparticles for Potential Biomedical Application. *Sci. Rep.* **2017**, *7*, 46513.

(133) Lee, C.; Kim, G. R.; Yoon, J.; Kim, S. E.; Yoo, J. S.; Piao, Y. In Vivo Delineation of Glioblastoma by Targeting Tumor-Associated Macrophages with near-Infrared Fluorescent Silica Coated Iron Oxide Nanoparticles in Orthotopic Xenografts for Surgical Guidance. *Sci. Rep.* **2018**, *8* (1), 11122. https://doi.org/10.1038/s41598-018-29424-4.

(134) Sun, P.; Zhang, H.; Liu, C.; Fang, J.; Wang, M.; Chen, J.; Zhang, J.; Mao, C.; Xu, S. Preparation and Characterization of Fe_3O_4/CdTe Magnetic/Fluorescent Nanocomposites and Their Applications in Immuno-Labeling and Fluorescent Imaging of Cancer Cells. *Langmuir* **2010**, *26* (2), 1278–1284. https://doi.org/10.1021/la9024553.

(135) Lee, I.; Wool, R. P. Controlling Amine Receptor Group Density on Aluminum Oxide Surfaces by Mixed Silane Self Assembly. *Thin Solid Films* **2000**, *379* (1), 94–100. https://doi.org/https://doi.org/10.1016/S0040-6090(00)01557-1.

(136) Maidenberg, Y.; Zhang, S.; Luo, K.; Akhavein, N.; Koberstein, J. T. Mixed Silane Monolayers for Controlling the Surface Areal Density of Click-Reactive Alkyne Groups: A Method to Assess Preferential Surface Adsorption on Flat Substrates and a Method to Verify Compositional Homogeneity on Nanoparticles. *Langmuir* **2013**, *29* (38), 11959–11965. https://doi.org/10.1021/la402517m.

(137) Fischer, T.; Dietrich, P. M.; Streeck, C.; Ray, S.; Nutsch, A.; Shard, A.; Beckhoff, B.; Unger, W. E. S.; Rurack, K. Quantification of Variable Functional-Group Densities of Mixed-Silane Monolayers on Surfaces via a Dual-Mode Fluorescence and XPS Label. *Anal. Chem.* **2015**, *87* (5), 2685–2692. https://doi.org/10.1021/ac503850f.

(138) Horikoshi, S.; Watanabe, T.; Narita, A.; Suzuki, Y.; Serpone, N. The Electromagnetic Wave Energy Effect(s) in Microwave–assisted Organic Syntheses (MAOS). *Sci. Rep.* **2018**, *8* (1), 5151. https://doi.org/10.1038/s41598-018-23465-5.

(139) Lamkhao, S.; Phaya, M.; Jansakun, C.; Chandet, N.; Thongkorn, K.; Rujijanagul, G.; Bangrak, P.; Randorn, C. Synthesis of Hydroxyapatite with Antibacterial Properties Using a Microwave-Assisted Combustion Method. *Sci. Rep.* **2019**, *9* (1), 4015. https://doi.org/10.1038/s41598-019-40488-8.

(140) Zhou, J.; You, Z.; Xu, W.; Su, Z.; Qiu, Y.; Gao, L.; Yin, C.; Lan, L. Microwave Irradiation Directly Excites Semiconductor Catalyst to Produce Electric Current or Electron-Holes Pairs. *Sci. Rep.* **2019**, *9* (1), 5470. https://doi.org/10.1038/s41598-019-41002-w.

(141) Galal, A.; Hassan, H. K.; Atta, N. F.; Abdel-Mageed, A. M.; Jacob, T. Synthesis, Structural and Morphological Characterizations of Nano-Ru-Based perovskites/RGO Composites. *Sci. Rep.* **2019**, *9* (1), 7948. https://doi.org/10.1038/s41598-019-43726-1.

(142) Roto, R.; Yusran, Y.; Kuncaka, A. Magnetic Adsorbent of Fe_3O_4@SiO_2 Core-Shell Nanoparticles Modified with Thiol Group for Chloroauric Ion Adsorption. *Appl. Surf. Sci.* **2016**, *377*, 30–36. https://doi.org/10.1016/j.apsusc.2016.03.099.

(143) Robinson, I.; Tung, L. D.; Maenosono, S.; Wälti, C.; Thanh, N. T. K. Synthesis of Core-Shell Gold Coated Magnetic Nanoparticles and Their Interaction with Thiolated DNA. *Nanoscale* **2010**, *2*, 2624–2630. https://doi.org/10.1039/c0nr00621a.

(144) Wang, F.; Li, Y.; Wang, Y.; Cao, Z. Self-Assembled Monolayer of Designed and Synthesized Triazinedithiolsilane Molecule as Interfacial Adhesion Enhancer for Integrated Circuit. *Nanoscale Res. Lett.* **2011**, *6* (1), 483. https://doi.org/10.1186/1556-276X-6-483.

(145) Wang, J.; Yang, H.; Guan, C.; Liu, J.; Chen, Z.; Liang, P.; Shen, Z. Space-Confinement and Chemisorption Co-Involved in Encapsulation of Sulfur for Lithium-Sulfur Batteries with Exceptional Cycling Stability. *J. Mater. Chem. A* **2017**, *5* (47), 24602–24611. https://doi.org/10.1039/c7ta08620b.

(146) He, Y.; Shan, Z.; Tan, T.; Chen, Z.; Zhang, Y. Ternary Sulfur/Polyacrylonitrile/SiO_2 Composite Cathodes for High-Performance Sulfur/Lithium Ion Full Batteries. *Polymers (Basel).* **2018**, *10* (8), 930. https://doi.org/10.3390/polym10080930.

(147) Ye, J.; He, F.; Nie, J.; Cao, Y.; Yang, H.; Ai, X. Sulfur/carbon Nanocomposite-Filled Polyacrylonitrile Nanofibers as a Long Life and High Capacity Cathode for Lithium–sulfur Batteries. *J. Mater. Chem. A* **2015**, *3* (14), 7406–7412. https://doi.org/10.1039/C4TA06976E.

(148) Abdul Razzaq, A.; Yao, Y.; Shah, R.; Qi, P.; Miao, L.; Chen, M.; Zhao, X.; Peng, Y.; Deng, Z. High-Performance Lithium Sulfur Batteries Enabled by a Synergy between Sulfur and Carbon Nanotubes. *Energy Storage Mater.* **2019**, *16*, 194–202. https://doi.org/https://doi.org/10.1016/j.ensm.2018.05.006.

(149) Ju, J.; Zhang, R.; He, S.; Chen, W. Nitrogen-Doped Graphene Quantum Dots-Based Fluorescent Probe for the Sensitive Turn-on Detection of Glutathione and Its Cellular Imaging. *RSC Adv.* **2014**, *4* (94), 52583–52589. https://doi.org/10.1039/C4RA10601F.

(150) Thomas, G.; Demoisson, F.; Boudon, J.; Millot, N. Efficient Functionalization of Magnetite Nanoparticles with Phosphonate Using a One-Step Continuous Hydrothermal Process. *Dalt. Trans.* **2016**, *45* (26), 10821–10829. https://doi.org/10.1039/C6DT01050D.

(151) Iranpoor, N.; Firouzabadi, H.; Khalili, D.; Motevalli, S. Easily Prepared Azopyridines As Potent and Recyclable Reagents for Facile Esterification Reactions. An Efficient Modified Mitsunobu Reaction. *J. Org. Chem.* **2008**, *73* (13), 4882–4887. https://doi.org/10.1021/jo8000782.

(152) Guo, I. Preparation and Covalent Surface Modifications of Silica Coated Spherical and Rod-Shaped Gold Nanoparticles, Simon Fraser University, 2018.

Appendix A.

Tests to select the best solvent for use as the wash solution when functionalizing the silica-coated iron oxide nanoparticles and for the formation of core-shell structures

Table A1. A summary of and guide to solvents used in the tests in correlation to the results in Table A2.

solvent # (for Table A2)	solvent
1	methyl ethyl ketone
2	ethyl acetate
3	isopropanol
4	isopropanol + di(ethylene glycol)
5	ethanol
6	ethanol + di(ethylene glycol)
7	ethanol + heat (60 °C)
8	ethanol + di(ethylene glycol) + heat (60 °C)
9	toluene
10	toluene + di(ethylene glycol)

Table A2. **A summary of a selection of the solvents tested for washing the functionalized silica-coated iron oxide nanoparticles and for formation of core-shell structures.[a]**

#	wash #1 + Au NPs	wash #2 + Au NPs	wash #3 + Au NPs	solvent + Au NPs	solvent + Fe_3O_4 NPs
1	 X + not miscible	 X + not miscible	 X + not miscible	 X	 O
2	 X + not miscible	 X + not miscible	 X + not miscible	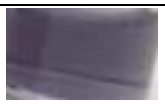 X	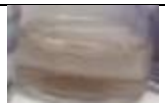 X
3	 X	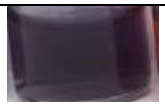 X	 O	 O	 O
4	 X	 X	 O	 O	 O
5	 X	 X	 X	 O	 O
6	 X	 X	 X	 O	 O
7	 X	 X	 X	 X	 O
8	 X	 X	 X	 X	 O
9	 O + not miscible	 X + not miscible	 O + not miscible	 O + not miscible	 X
10	 O + not miscible	 X + not miscible	 O + not miscible	 O + not miscible	 X

[a] O = no precipitation/color change observed; X = precipitation or aggregation/color change observed.

Appendix B.

Dynamic light scattering analysis of different types of nanoparticles

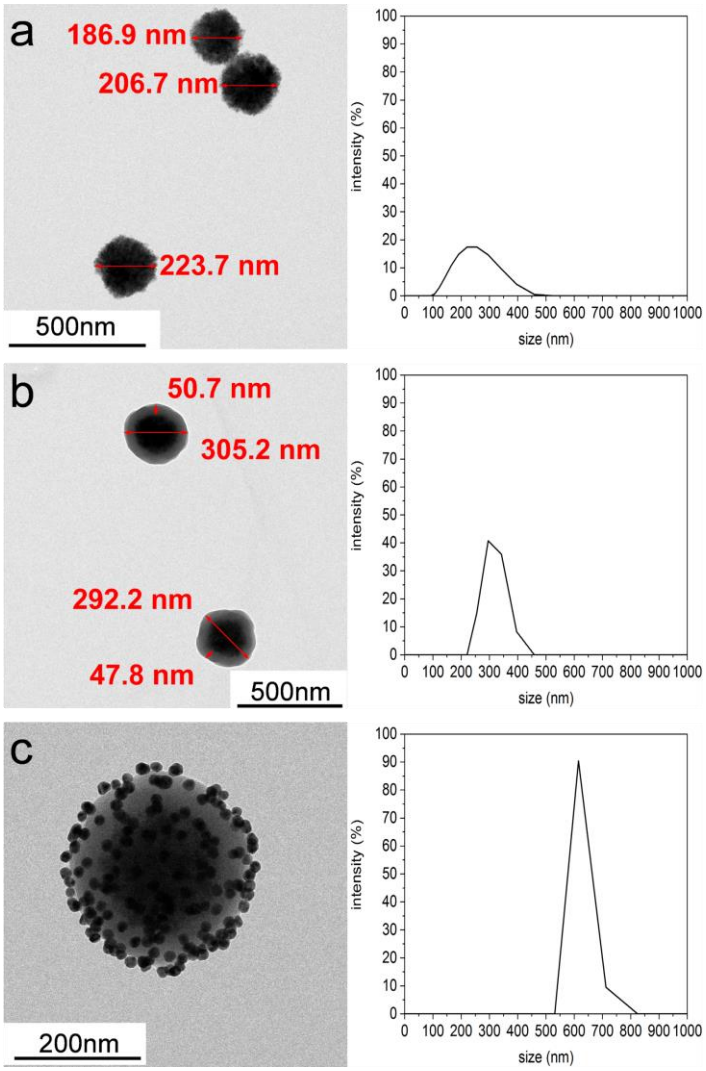

Figure A1. **Transmission electron microscopy and dynamic light scattering data for: a) bare iron oxide nanoparticles; b) silica-coated iron oxide nanoparticles; and c) gold attached to the thiol functionalized silica-coated iron oxide nanoparticles.**

Appendix C.

Fourier transform infrared spectroscopy (FT-IR) results for thiol functionalized silica-coated iron oxide nanoparticles

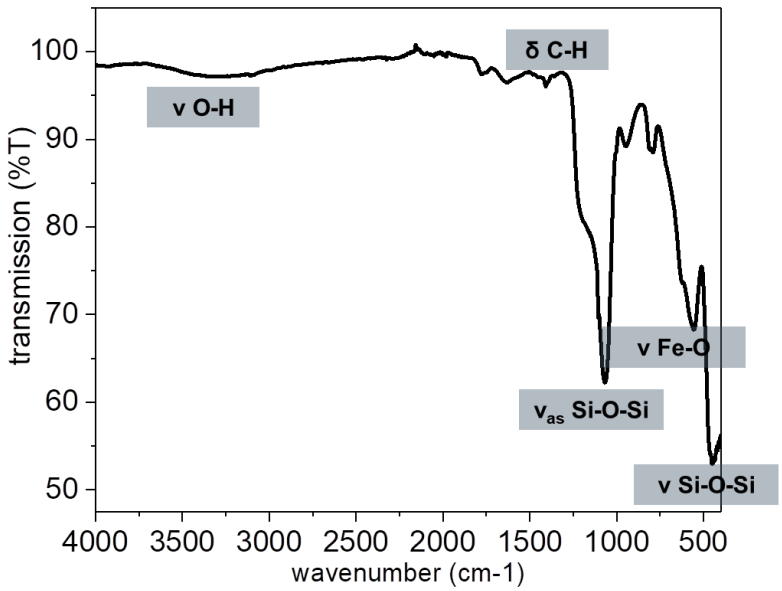

Figure C1. **Fourier transform infrared spectroscopy (FT-IR) results for thiol functionalized silica-coated iron oxide nanoparticles.**

Appendix D.

Raman spectroscopy results for thiol and carboxylic acid functionalized silica-coated iron oxide nanoparticles and bare silica-coated iron oxide nanoparticles

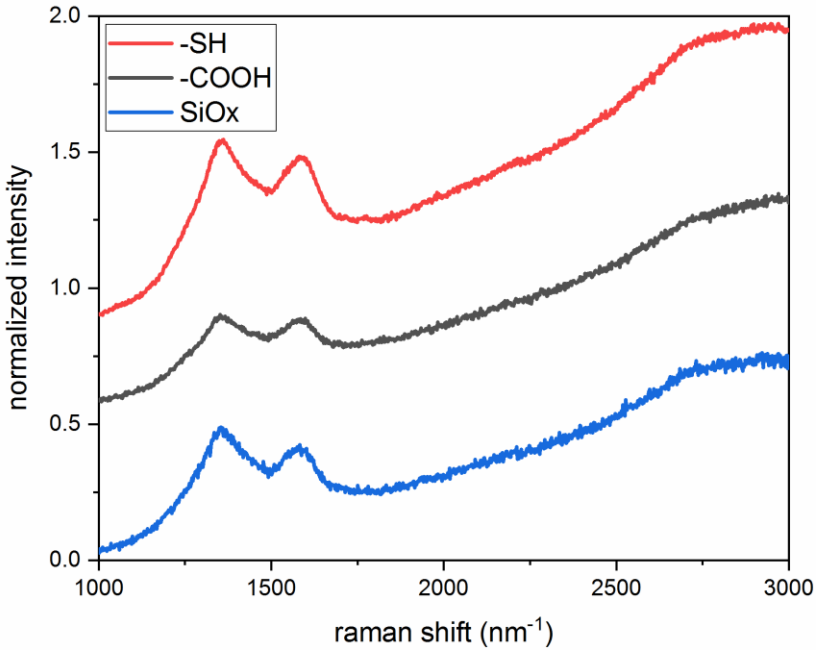

Figure D1. **Raman spectroscopy results for thiol (red) and carboxylic acid (black) functionalized silica-coated iron oxide nanoparticles and bare silica-coated iron oxide nanoparticles (blue).**

Appendix E.

Thermogravimetric analysis of thiol and carboxylic acid functionalized silica-coated iron oxide nanoparticles and bare silica-coated iron oxide nanoparticles

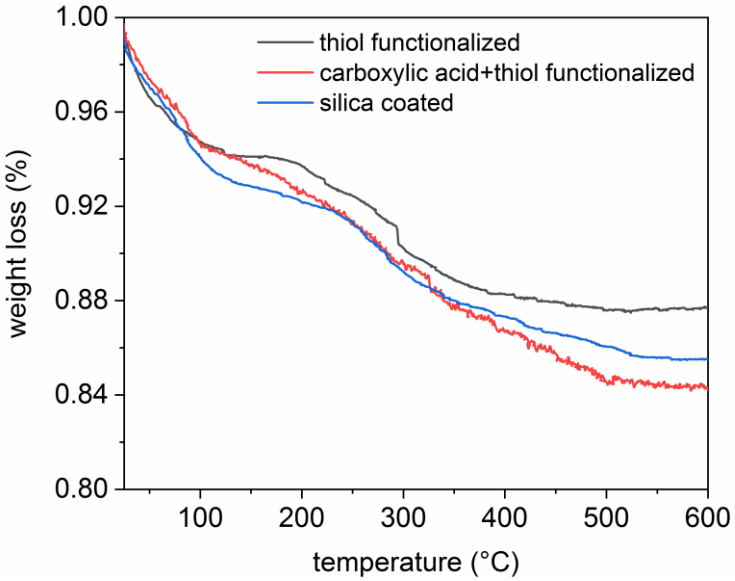

Figure E1. **Thermogravimetric analysis of functionalized silica-coated iron oxide nanoparticle: (black) the thiol functionalized NPs; (red) 50% thiol/ 50% carboxylic acid functionalized NPs; and (blue) bare silica-coated iron oxide NPs.**